LONDON'S GLOBAL UNIVERSITY

Multimodal Imaging for Characterisation and Testing of Composite Materials

Dana Shoukroun

Department of Medical Physics and Biomedical Engineering
University College London (UCL)

A thesis submitted for the degree of

Doctor of Philosophy

September 2021

I, Dana Shoukroun, confirm that the work presented in this thesis is my own. Where information has been derived from other sources, I confirm that this has been indicated in the thesis.

Signed:

D. Shoukroun

October, 2021

Abstract

Carbon fibre reinforced polymers (CFRP) are widely used across several industries, including aerospace, as they are lightweight and offer superior mechanical properties. Barely Visible Impact Damage (BVID), including cracks, delaminations, fibre debonding, as well as manufacturing defects such as porosity, are detrimental to CFRP structural integrity and detection of such faults is important. Different non-destructive evaluation (NDE) methods exist, including ultrasound, X-ray computed tomography (X-ray CT), infrared, and liquid penetrant testing. Edge Illumination X-ray Phase Contrast imaging (EI XPCi) was benchmarked as a viable NDE method for damage detection in CFRP, as it offers additional information through multimodal imaging. With the acquisition of at least three images, EI XPCi allows for the retrieval of the attenuation, differential phase, and dark field signals, using a pair of apertured masks. EI XPCi CT was compared with ultrasonic immersion C-scan imaging and high-resolution X-ray CT for the detection of severe impact damage in a composite plate (visible indent damage on surface of plate and protrusion on the back). The full extent and scale of the different defects were observed in the phase-based signals to a better standard than ultrasonic immersion imaging, with observations confirmed using high resolution X-ray CT. Planar EI XPCi was then compared to contrast agent X-ray imaging and ultrasonic immersion C-scan imaging on a different, less damaged specimen (only small crack visible on surface), showing that planar EI XPCi can detect a network of cracks across the specimen and overcame some of the limitations of contrast agent X-ray imaging. However, in the planar imaging, delamination damage was only detected by the ultrasonic measurement, showing the necessity of using both ultrasonic imaging and EI XPCi for a complete understanding of the damage in the plate. EI XPCi was used for the quantification of porosity for woven composite plates with varying porosity (0.7% to 10.7%), compared to ultrasonic through transmission imaging and destructive

matrix digestion. The introduction of the standard deviation of the differential phase (STDP) showed excellent correlation with the porosity calculated from matrix digestion. The STDP signal quantifies the variation of the distribution of inhomogeneities for features of a scale equal to or above the system resolution (in this case, 12μm along the direction of phase sensitivity), which was advantageous for the investigated set of specimens with larger porosity.

Impact Statement

The research conducted in this project benchmarked the use of the novel Edge Illumination X-ray Phase Contrast Imaging (EI XPCi) method as a viable non-destructive evaluation approach for impact damage and manufacturing defect detection in carbon fibre reinforced composite (CFRP) plates. This was achieved by comparing both planar and 3-dimensional computed tomography (CT) EI XPCi to ultrasonic imaging and conventional X-ray imaging, including with the use of contrast agents.

EI XPCi was compared with ultrasonic immersion C-scan imaging, conventional high-resolution X-ray CT and contrast agent X-ray imaging for damage detection in severely damaged carbon fibre reinforced composite plates (Chapters 4 and 5). This showed the complementarity offered by phase-based signals to the conventional attenuation signal, and the possibility of identifying defects based on the signal in which they manifest. It demonstrated the potential EI XPCi offers for the NDE of composites, allowing better detection and identification of damage. This project was conducted in collaboration with Nikon, where preliminary scans of damaged aeroplane CFRP parts were independently performed on a commercial prototype of the EI XPCi system using the results from this project. This demonstrates the advantage of planar EI XPCi over other XPCi methods, as scans of large specimens can be performed relatively quickly.

The post-processing image analysis techniques developed in this project (Chapter 3) allow for the removal of image artefacts from long acquisitions and the improvement of image quality post-acquisition, and can be applied to any EI XPCi acquisition without affecting the qualitative and quantitative quality of the retrieved images.

The new approach using the standard deviation of the differential phase signal (STDP), discussed in Chapter 6, allows for better

visualisation of the variation in the distribution of inhomogeneities of the samples, and thus for the quantification of porosity in composite plates. Employing only planar imaging, it allows for faster quantification compared to X-ray CT imaging, but compromises on the ability to locate the porosity through the thickness of the sample. Further evaluation of the approach should also be conducted to investigate its relation to porosity distribution and size. This new approach has great potential and, once characterised and quantified in relation to the dark field signal, can lead to a precise quantification of porosity in composite plates across pore size ranges. It can also enable the evaluation of the pore size distribution and of other manufacturing defects such as fibre misalignment, as well as the evaluation of fibre anisotropy. The use of the standard deviation of the differential phase offers a fast and accurate representation of porosity in composite plates using planar imaging, which is not achievable using other NDE techniques, and can be applied across many applications, not only in the physical sciences, but also in biomedical imaging.

The introduction and benchmarking of EI XPCi, along with the additional methodologies presented in this project, has great potential for the aerospace industry. Once adapted to and implemented in an industrial environment, it could allow for the testing of potentially damaged components, performing a detailed analysis on samples as they are developed, and providing feedback of the characterisation results to the material developers, ultimately leading to improved manufacture of composites.

List of Publications

Journal articles – First Author:

D. Shoukroun, L. Massimi, F. Iacoviello, M. Endrizzi, D. Bate, A. Olivo, P. Fromme, “Enhanced composite plate impact damage detection and characterisation using X-Ray refraction and scattering contrast combined with ultrasonic imaging”, Composites Part B: Engineering, Volume 181, 107579, 2020, https://doi.org/10.1016/j.compositesb.2019.107579

D. Shoukroun, L. Massimi, M. Endrizzi, D. Bate, A. Nesbitt, P. Fromme, A. Olivo, “Quantification of Porosity in Woven Fibre Reinforced Composite Plates using Edge Illumination X-ray Phase Contrast Imaging and Ultrasonic Attenuation”, (submitted)

D. Shoukroun, L. Massimi, M. Endrizzi, D. Bate, P. Fromme, A. Olivo, “A Comparison between Edge Illumination X-ray Phase Contrast Imaging, X-ray Contrast Agents and Ultrasonic Immersion C-scan Imaging for Impact Damage Detection in Composite Plates”, (under review).

Oral Presentations at Conferences – First Author:

D. Shoukroun, P. Fromme, A. Olivo, “Edge illumination X-ray phase contrast imaging for imaging defects in composite structures”, Review of Progress in Quantitative Nondestructive Evaluation (2019), Portland, Oregon (USA).

D. Shoukroun, P. Fromme, A. Olivo, “Comparison of NDE techniques for damage detection in fibre-reinforced composites”, Review of Progress in Quantitative Nondestructive Evaluation (2019), Portland, Oregon (USA).

D. Shoukroun, P. Fromme, A. Olivo, “The Use of Edge Illumination X-ray Phase Contrast Imaging and Ultrasonic Attenuation for Porosity Detection in Composite Structures”, Review of Progress in Quantitative Nondestructive Evaluation (2021), Online.

Conference Proceedings – First Author:

D. Shoukroun, L. Massimi, M. Endrizzi, D. Bate, A. Olivo, P. Fromme, “Composite Impact Damage Detection and Characterization using Ultrasound and X-ray NDE Techniques”, Proc. SPIE 11381, Health Monitoring of Structural and Biological Systems XIV, 113810B (2020), https://doi.org/10.1117/12.2549078

D. Shoukroun, L. Massimi, M. Endrizzi, D. Bate, P. Fromme, A. Olivo, “Composite Porosity Characterization using X-ray Edge Illumination Phase Contrast Imaging and Ultrasonic Techniques”, Proc. SPIE 11593, Health Monitoring of Structural and Biological Systems XV, 115932M (2021), https://doi.org/10.1117/12.2582561

D. Shoukroun, P. Fromme, A. Olivo, “Edge Illumination X-ray Phase Contrast Imaging and Ultrasonic Attenuation for Porosity Quantification in Composite Structures”, Proceedings of the ASME 2021, 48th Annual Review of Progress in Quantitative Nondestructive Evaluation (2021), (under review).

Other publications – Co-author:

A. Olivo, F.A. Vittoria, P. Modregger, G.K. Kallon, L. Massimi, J. Jiang, S. Savvidis, G. Havariyoun, C.J. Maughan Jones, I. Buchanan, D. Shoukroun, P.R.T. Munro, C.K. Hagen, M. Endrizzi, “Flexible Solutions for Lab-based Phase Contrast and Dark Field CT and micro-CT”, iCT 2019 Session: New Methods & Optimization (pp. 23652-1), NDT.net: Padova, Italy.

Acknowledgments

First, I would like to express my sincere gratitude to both of my supervisors, Prof. Sandro Olivo and Prof. Paul Fromme, for their invaluable supervision, support, and mentorship during this PhD. Their knowledge and experience encouraged me and gave me the enthusiasm needed to achieve this PhD and more. I would like to thank them both for their continuous support, both academic and personal, and their continuous advice, as each one of them was invaluable to this PhD in his own way.

I would also like to thank Dr. Lorenzo Massimi, who provided me with help and support since day one of this PhD, for the hours spent in the lab fighting both code and equipment, for his insights, suggestions, and most importantly his patience for my “one-more-question”.

I would like to say a special thanks to the AXIM group, for making me feel at home as soon as I joined. I would like to especially thank Dr. Gibril Kallon, Dr. Ian Buchanan, Dr. Savvas Savvidis and Dr. Peter Modregger, for the fantastic brainstorming sessions and discussions in the office that gave me the necessary external point of view to continue and improve my work.

I would like to thank my industrial supervisor, David Bate, for the support and advice he provided throughout this PhD. I would also like to thank Nikon, for co-funding this PhD and allowing me to use their facilities in Tring to expand my research and gain industrial experience.

I am forever grateful for my family’s support, to my mother, Ronit, who started this journey with me nine years ago and was always supportive, attentive, and listened to my “complaints”. I would like to thank my dad, Yossi, for his continuous advice and pride in what I do,

my sister, Amit for her unparallel love and support, and my partner, Dan, for his patience and constant attempt to understand what I am talking about. Lastly, I would like to dedicate this thesis to my uncle Shmuel, who always offered to help “if I get stuck” with my research, and always looked forward to the day he could call me Dr.

Table of Contents

List of Symbols

C	Attenuation contrast
I	Transmitted intensity
n	Refractive index
δ	Real part of refractive Index
β	Imaginary part of refractive index
λ	Wavelength
ϕ	Phase Shift
$\Delta\theta_R$	Refraction angle
v	Wave velocity
F_z	Focal length
t	Time
f	Frequency
D_f	Focussed beam diameter
D	Transducer diameter
Z	Acoustic impedance
R	Reflection factor
N	Near field
ΔI	Signal attenuation
V	Signal amplitude
M	Magnification
G	Geometric magnification between sample stage and sample mask position
$I_{N,M}$	Fitted Gaussian
$t_{N,M}$	Areas of measured curves
$\sigma^2{}_{N,M}$	Widths of measured curves
$\Delta x_{N,M}$	Centres of measured curves
Δx_R	Refraction Signal
$\sigma^2{}_0$	Scattering Signal
P(x,y)	Polynomial fitted for gradient correction
G(x)	Normalised Gaussian

List of Figures

1 Introduction

Fibre-reinforced composite materials are used across a wide range of industries, including aerospace and military, as their high strength and low weight offer an advantage over other materials. Defects in composite materials, such as matrix cracking, fibre breakage, debonding and delamination, are caused by stress, fatigue, or impact events. These defects affect the structural integrity of the composite components, potentially leading to complete failure. The detection and characterisation of such defects are thus of primary importance in predicting the composite's health and performance capabilities [1,2] Another class of defect that can occur in fibre-reinforced composite plates are manufacturing defects, such as discrete voids and porosity. High levels of porosity induced during manufacturing (in aerospace, equivalent to above 2% porosity), reduce the compressive and interlaminar shear strength of the plates [3].

Non-Destructive Evaluation (NDE) or Testing (NDT) aims at identifying and characterising damage in structures, both internally and externally, while conserving its structural integrity. Such evaluation is conducted using different imaging techniques, such as radiography, ultrasonic testing, eddy current testing, magnetic testing [4], penetrant testing, thermography, and infrared testing [1,5]. NDE has many applications, including manufacturing, military and defence, aerospace and nuclear industries, as well as for defect characterisation in materials and composites. Ultrasonic imaging and conventional radiography are commonly used for defect detection and evaluation in fibre-reinforced composite plates as they offer high resolution and are easy to set up [6]. However, ultrasonic imaging encounters difficulties in identifying multiple defects across the thickness of the sample, and requires compromises on resolution for the analysis of thicker plates [7]. Conventional radiography struggles with the detection of defects using 2D planar imaging. As a result, time-

consuming X-ray computed tomography (X-ray CT) scans need to be acquired for better visualisation of damage, which often imposes limits on the specimen size. Moreover, in carbon fibre-reinforced polymers (CFRP), contrast limitations are imposed due to similar attenuation coefficients, leading to more difficulties in resolving features [6].

In the past years, phase-enhanced X-ray imaging has been investigated for the NDE of materials, most noticeably composite materials, however mostly at synchrotron facilities [8]. Only a limited number of studies were done in a laboratory environment and were focused on anisotropy investigations [9]. The work in this thesis aims to benchmark Edge-Illumination Phase Contrast X-ray imaging (EI XPCi) as a viable NDE technique for damage detection and porosity evaluation in laminate composite plates. EI XPCi uses refraction effects induced in the X-ray beam passing through an object to create contrast, in addition to the dark field signal, which is due to ultra-small scattering caused by sub-pixel features [10,11]. This benchmarking was achieved by qualitatively and quantitatively comparing EI XPCi with established ultrasonic testing techniques, foremostly immersion C-scan ultrasonic imaging. By doing this, a better interpretation of the damage detected with ultrasonic C-scan imaging can be obtained, complemented by multimodal EI XPCi, as well as a better understanding of the limitations of each imaging technique.

In this thesis, an overview of carbon-based fibre-reinforced composite materials is presented in the literature review (chapter 2). Their usage in the aerospace industry is detailed, along with the typical defects occurring during manufacturing and in-service. A state-of-the-art summary of the current NDE techniques used for damage detection in fibre-reinforced composite plates is presented, focussing on the use of ultrasonic imaging and conventional and phase-enhanced radiography. The third chapter presents the different ultrasonic and radiographic experimental methods used for this research. The fourth chapter presents a preliminary qualitative comparison between both

planar and CT EI XPCi and ultrasonic immersion C-scan imaging for damage detection and identification in a carbon-based fibre-reinforced composite plate suffering from severe impact damage. This comparison evaluates the complementarity offered by the addition of the differential phase and dark field signal to the conventional attenuation signal, which results in a better identification of the damage incurred. This comparison is then further investigated in chapter five, where conclusions obtained from the multimodal planar phase contrast X-ray imaging of another sample suffering from impact damage are compared to images obtained using planar contrast agent X-ray imaging, which is another NDE technique often used for damage detection. Conventional radiography and ultrasonic C-scan imaging were also used for a thorough comparison of all imaging techniques. The sixth chapter provides a study investigating the use of planar EI XPCi for the quantitative evaluation of porosity in cross-ply woven pre-impregnated (pre-preg) composite plates. This investigation explores the use of planar images as opposed to the use of micro-CT; while offen the preferred method in industry, as mentioned micro-CT limits sample size and is time consuming. This study tracks the evaluation of the dark field signal as well as the standard deviation of the differential phase signal and correlates it to an ultrasonic signal attenuation and known porosity values calculated using the destructive matrix digestion provided by the manufacturer. An additional ultrasonic comparison was done, investigating the variation of signal attenuation with porosity for different frequencies.

2 Carbon Fibre-Reinforced Composites, NDE Techniques, and X-Ray Phase Contrast Imaging

2.1 Introduction

This chapter presents a literature review of the different areas relevant to this investigation. In the first part of this chapter, the components, manufacturing, and usage of composites is described. Then, the different types of defects found in composites are described, ranging from manufacturing to in-service defects. In the second part of this chapter, Non-destructive Evaluation (NDE) techniques are introduced, listing the different imaging techniques used for the detection of damage in composites. Ultrasonic imaging is then introduced, with an explanation of its basic principle and a state-of-the-art review of the use of ultrasonic imaging for damage detection in composites. The same was then done for conventional X-ray imaging, where both the working principle and its use in industry are described. In the last part of this chapter, X-ray phase contrast imaging (XPCi) is introduced, more specifically Edge Illumination (EI) XPCi. The working principles of XPCi and EI XPCi are described, along with the state-of-the-art review of the use of XPCi for damage detection in composites. Lastly, as this investigation aims at comparing EI XPCi with ultrasonic imaging and conventional X-ray imaging, a review of the research where XPCi is compared with the latter two techniques is laid out, setting out the base of this investigation.

2.2 Carbon Fibre-reinforced Composites

Fibre-reinforced composites, or laminates, are complex materials composed of layers, referred to as laminae or ply, of fibre materials which are embedded in a matrix, in a given orientation [1,2]. They are widely used in the aerospace, marine, and recreational industries as they present an advantage over other materials due to their high

strength, durability, toughness, and fatigue endurance. They are also highly resistive against temperature variations, corrosion, and chemical attacks. Composite materials are extremely lightweight, which presents an advantage for the aerospace industry where material weight is an important issue [12].

2.2.1 Composites Materials, Manufacturing, and Industrial Use

A composite can be defined as a material consisting of two or more distinct components [12]. These components usually are continuous fibres arranged in a specific orientation within a matrix. The aim of such arrangement is to take advantage of the mechanical properties of both materials and combine them. The aim of the fibres in composites is to carry loads, whereas the matrix evenly distributes the load between the different sheets (plies or laminae) of fibres with the same orientation [12]. The matrix and fibre materials chosen to make a composite play a very important role; the fibre properties control the impact resistance of the composite material, and thus the load bearing capacity, with the fibres' elastic energy storage capabilities of fundamental importance [13]. The matrix plays a protective role, and thus aims to stabilise the fibres by ensuring a homogeneous distribution of stress among them [12,13]. Popular examples of matrix materials include epoxy resin, preferred for its versatility, as it can be cross-linked with other materials, including polymers, amines, and acids. It is, however, known to be quite brittle [12,14,15]. Other matrix materials include unsaturated polyesters and vinyl esters [16].

Depending on the desired material characteristics, fibres can account for 30-70% of the composite volume [12,14]. The most common fibre material used in the aerospace industry is carbon, as it offers high tensile strength and thermal conductivity, low material density and stiffness [13]. Glass, aramid, ceramics, and metallic fibres are also used as fibre materials in composites [12,14,15,17]. Typically, the diameter of carbon fibres can vary between 7 and 15 μm [14,18]. The

fibres can be chopped or continuous, with the latter allowing for several types of orientations (e.g. unidirectional, woven, or braided) [14].

Lamina, or ply, thickness usually varies from 100 to 500μm [19]. The most common fibre orientation used within a single lamina is unidirectional, i.e., where the fibres are parallel. Other fibre orientations, such as woven or braided, can also be used [13]. The individual plies are then stacked together with a certain orientation to form a laminate, with the typical orientations being unidirectional, cross-ply (the fibres of each ply are perpendicular to the fibres in their neighbouring plies), and quasi-isotropic (e.g. plies stacked with 45 degrees difference). Fibre reinforced composite plates are anisotropic in nature, and continuous fibre plies are transversely anisotropic by default [12]. To make a composite plate isotropic, discontinuous fibres must be used in random orientations [14]. The number of plies, their specific orientation with respect to each other as well as their order play a role in the impact resistance and degree of anisotropy of the composite plate [20].

Unidirectional fibre reinforced composite plates are characterised by a high specific strength and stiffness along the fibre orientation, however they are highly susceptible to impact damage due to their heterogeneity [20,21]. Cross-ply composite plates were found to offer the best impact resistance and can absorb more energy than other ply orientations. The nature and severity of damage thus depends on the relative orientation of adjacent plies [12,13,17,22].

Different types of manufacturing processes for composite plates exist, depending on their composition and geometry [23]. They are divided into two main manufacturing methods for the aerospace industry: autoclave processes and out-of-autoclave processes [24]. The first refers to pre-impregnated (pre-pregs) which are fused together, and out-of-autoclave processes refers to the fibres first being laid in a mould, and the liquid resin being injected subsequently to saturate and

cover the fibres [25]. Pre-pregs composite plates are a type of laminate used in industry. They consist of thin plies, which are manufactured by laying the fibres onto the already present resin. The impregnated fibres are then pressed together between sheets to ensure the wetting of the fibres by the resin. This process is done to produce unidirectional and cross-ply composites as it results in good alignment of the fibres [26].

Composite materials are used across many industries, including aerospace, automotive, racing, sports, and leisure, with the greatest demand being the aerospace and automotive industries [27,28]. The use of composite materials has also increased in the infrastructure industry, mainly for pipe, tank, and plant engineering [29], and in the construction industry for reinforcements to concrete pillars and bridge decks [30,31]. Composite materials offer great advantages, not only due to their lightweight properties, but also thanks to their excellent corrosion resistance, and their high level of freedom of design, giving them great potential to replace established materials in many applications. In the aerospace industry, the global demand for composites is increasing as they allow to reduce aircraft weight, improve manufacturing times, and save costs [32,33]. Reducing the weight of an aircraft makes it more fuel efficient leading to a reduced carbon footprint. This demand leads to an increase in the number of large, geometrically complex, flight critical composite structures in the latest generation of commercial aircrafts and engines [34]. CFRP can be found in wing planks, sandwich panels, and fuselages of the airplane, and are used also to strengthen and repair existing structures [35]. They can also be found in helicopter rotor structures [36]. In the marine industry, composite materials were originally used for the construction of boats as early as post-World War II, replacing the use of timber which was easily degraded by seawater. Composite structures can now be found in submarines, and personal and commercial boats [37].

2.2.2 Defects in Composite plates

Composites cannot absorb energy through plastic deformation, and, as a result, when high external loads are applied on a composite, damage occurs [15,38]. Such loads can lead to fatigue or impact loads, and the formation and propagation of damage can be accelerated by structural discontinuities [22]. This leads to the structural integrity of the composite to be compromised [39]. Damage can be defined as a collection of irreversible changes made to the material due to different external factors, such as manufacture or impact damage. The severity of the induced damage relates to how the damage is formed, as well as its growth under external loads [22]. Relevant examples of damage in composite plates include cracks (intra- and interlaminar), fibre breakage, debonding and delaminations [13,39,40]. Recent studies showed that the probability for damage in composite plates increases with the complexity of the structure [41]. The American Society for Testing and Materials (ASTM) defines a flaw as “an imperfection that may be detected by NDE method and is not rejectable”, a defect as “one or more flaws who aggregate size, shape, orientation, location, or properties do not meet specified acceptance criteria and are therefore rejectable”, and damage as the “change to the material or geometric properties of a structural system that affects its performance” [42], however in literature the three tend to be used interchangeably.

2.2.3 Manufacturing Defects

Manufacturing defects are induced during the processing of composite plates, and are grouped into matrix defects (e.g. incomplete curing, voids), fibre defects (fibre misalignment, waviness, broken fibres) and interface defects (fibre debonding) [39]. The most common type of manufacturing defect is porosity, or voids, and is a known problem in the manufacturing process of CFRP. Porosity is defined as a significant number of micro-voids in the sub-millimetre scale that can have an overall effect on the mechanical properties of the

components, whereas voids are defined as of millimetre size and large enough to have an individual structural impact [43]. Voids vary in size, shape and location, arising from faults or improper parameter settings in the curing process [44]. Their formation can be controlled by varying the pressure, temperature, or the resin's viscosity; however, this results in an increase in manufacturing costs and time.

Large voids can be the result of an incorrect resin infusion process or heated gas without an exit from the central area of the composite. They can also be due to an uneven temperature profile, as an even temperature profile is very difficult to obtain [35,41]. High levels of porosity are a serious problem [45,46], and most techniques concentrate on the detection and quantification of porosities in the 1%-5% range, with porosity levels above 2% typically considered not acceptable by the aerospace industry [43,47]. Void formation is a complex subject that is widely investigated and is highly dependent on the manufacturing process used. In out-of-autoclave processes, voids are believe to originate from air entrapment during the resin injection, with the porosity size and location depending on the mould geometry and complexity, the resin properties, temperature, and pressure[48]. In autoclave cure processes, voids originate in resin-rich area during the formulation of the pre-preg materials, and potential tears in the vacuum bag during the cure cycle, with their size and distribution in the laminate depending on the temperature, pressure of the cure, the stacking sequence, and the moisture absorbed during storage [48].

Porosity in CFRP mainly affects the matrix dominated mechanical properties, such as compressive and flexural strengths and interlaminar shear strength. Understanding the effect of porosity on those properties is complex, as numerous variables play a role, including the void shape, size, and distribution, but also the mechanical properties of the fibres and matrix, and the applied loads [49,50]. Studies have investigated void formation, including shape, size, and location, depending on porosity content and distribution in

composite samples, for different layups, processing parameters and manufacturing techniques [51,52].

Fibre manufacturing defects such as waviness or fibre misalignment can lead to a decrease in the primary compression strength and stiffness of the composite plate. The occurrence of manufacturing defects largely depends on the conditions and the processes involved to manufacture the composites [39] .

2.2.4 In-Service Defects

CFRP are prone to Barely Visible Impact Damage (BVID), due to the brittle nature of the carbon fibres [53]. BVID is a type of damage that can be induced in a composite plate in-service, and can be defined in different ways; Scarponi et al. [54] define BVID as “damage induced by an impact which causes indentation of 0.3-0.4mm.”; others define it as a damage induced in a composite with no visual evidence of the impact event [55]. BVID is a result of low velocity impacts, which are defined as events where the damage is induced by a body whose velocity typically varies between 1 to 10 m/s, depending on the target and impactor properties. Low velocity impacts are characterised by the long contact duration between the target and the impactor, resulting in the entire structure responding to the impact [15]. BVID from low velocity impacts are predominantly intra-ply matrix cracks and delaminations [22].

Matrix cracks are induced by low velocity impacts, which can also manifest as debonding between matrix and fibres in a ply when the interface between the two is weak [15,22,39]. They are the initial type of BVID to occur, and are the most common type of damage caused by transverse impact, tensile, compressive and shear stresses which disperses across the impact area [55]. Intra-ply matrix cracks extend across the ply parallel to the fibres orientation [22]. The smaller matrix cracks, called micro-cracks (up to 50μm long), tend to appear as the

weight load on the material increases. Macro-cracks tend to be a few 100s of μm to a few mm long, and about 50-150μm wide. As the cracks grow, they eventually start to interact with each other. Secondary micro-cracks grow from the main matrix cracks, which can initiate delaminations [39]. Macro-cracks are always connected to a delamination, either directly or through secondary micro-cracks. Macro inter-ply cracks propagate at an angle, as seen in Fig. 2-1, and not perpendicular to the laminates, until they reach the adjacent plies interface, leading to the formation of a delamination at that interface [22,56].

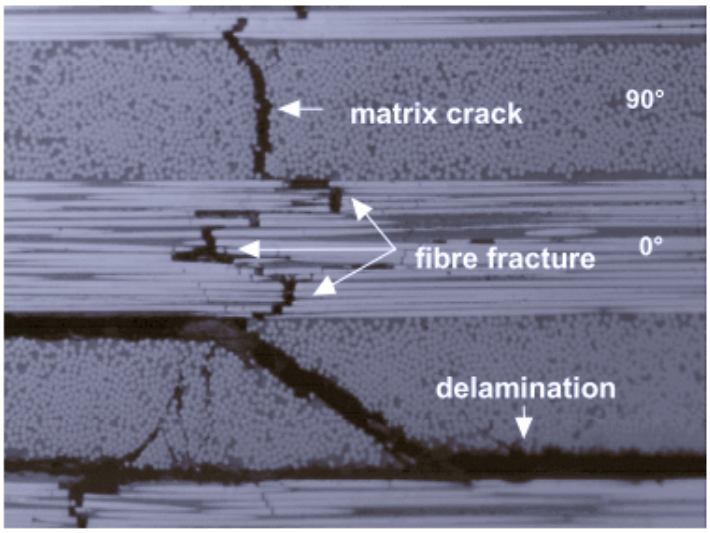

Figure 2-1 *Different types of impact induced damage in a [0°,90°] cross-ply composite*[40].

Delaminations, also referred to as interlaminar cracks, are a type of impact damage which results in the separation of two adjacent plies in a laminate, leaving a small pocket of air between the two plies. They are considered the most severe type of BVID as they significantly reduce the load carrying capacity of the structure [15]. Delaminations are caused by interlaminar stresses and usually have a surface area of about 100-1000 mm^2 depending on the applied load, and 20-50 μm thick, with morphologies of peanut or butterfly shapes. This type of damage is usually found in the resin rich area between adjacent plies, and is the most common type of in-service damage [12,15,22,39,55].

This type of defect can also be induced by intralaminar ply cracks at the edge of a given ply. Delaminations are usually initiated by matrix cracks, and occur after a certain energy threshold has been reached [15,22,55].

Fibre failure usually results in fibre breakage, and is due to local high stresses [15]. Fibre failure is usually observed closed to the impact point due to high compressive stresses, as well as in proximity to macro-cracks [55]. The different types of impact damages, as well as their locations within the structures, are characterised by their occurrence in composite materials with specific ply orientations, specific fibre/matrix ratios, as well as the mechanical properties of the constituents [12,14]. The dimensions of each type of damage, as well as their evolution, are characteristics which depend on the magnitude and location of the applied load, as well as the mechanisms involved in causing the damage [39]. Many studies try to model and thus predict the formation and propagation of damage formation in composite plates [20,57–59], however a general model is yet to be achieved.

The occurrence of all the defects mentioned above affects the structural integrity of the composite components and can potentially lead to their complete failure. As a result, the detection and identification of those defects are important for predicting the composite structure health and performance capabilities. In the aerospace industry, CFRP are limited to 0.4% compressive strain to failure, and as a result the cost of maintenance and inspection of the parts is high [60].

2.3 Destructive and Non-Destructive Evaluation

Non-Destructive Evaluation (NDE) or Testing (NDT) refers to the identification and characterisation of damage inside and on the surface of materials using non-destructive methods [61]. NDE techniques are used for damage evaluation in composite materials for many fields,

including manufacturing, aerospace, military and defence, and the nuclear industry [1,62], as stated above. Unlike metallic materials, composites are highly anisotropic, have high acoustic attenuation and poor electrical conductivity. Moreover, they are not exempt from unwanted manufacturing defects, nor do they have easily identifiable defects from in-service failures on their surfaces. As a result, the use of non-destructive evaluation techniques for the identifications of such defects is of great importance [7].

Many NDE techniques exist, categorised by contact and non-contact methods. Examples of contact methods include traditional ultrasonic testing [63], eddy current testing [64], magnetic testing [65,66] and liquid penetrant testing [67]. Non-contact methods include through transmission ultrasonic testing [54,68,69], radiography [70,71], infrared testing [5,72], holography [73] and shearography [74]. Composites vary in composition and structure, and based on the nature of the composite and its application, as well as the aim of the evaluation, certain NDE techniques are more advantageous than others [1,41,62,75]. For the aerospace industry, which is the main focus of this work, the main NDE techniques for aircraft composite structures are ultrasonic testing, X-Ray CT, thermographic testing [72,76], with ultrasonic testing being the most widely used technique for damage identification in aircraft composite components [1,7,77].

Destructive analysis is often used to accurately evaluate porosity in composite plates. The main technique is matrix digestion, measuring the mass of the specimen before and after the extraction of the resin through an acid, and relating these measurements to the known resin and fiber contents of the sample [78]. Other destructive techniques include micrograph image processing [79], density evaluation, and optical microscopy [80], which can be used to verify the accuracy of new non-destructive methods.

2.4 Ultrasonic Imaging

Ultrasonic testing enables the detection and localisation of defects, as well as their characterisation and measurement of their dimensions by analysing the information carried by the received signal. Ultrasonic testing presents several advantages, including scan speed, relatively high resolution, and the ability to detect internal defects and inhomogeneities in materials, as long as they are larger than half the used wavelength [6]. However, the achievement of high accuracy in immersion ultrasonic imaging requires laborious set ups and longer acquisition times [1,6]. Moreover, ultrasonic imaging is ideal for the detection of features that lie normal to the incident beam, such as delaminations, but is less sensitive for features such as matrix cracks and fibre fractures due to their narrow cross-section [38].

The quality of the ultrasonic testing depends both on its sensitivity (the ability to detect a feature) and its resolution (its ability to separate two distinct features that are close to each other). Both qualities increase with frequency, however, the higher the frequency, the higher the scattering of the signal in the material that leads to its attenuation, hence reducing the penetration power of the signal. As a result, a compromise must be found when choosing a frequency for the analysis of a composite based on its material structure and the size and type of defects involved [6].

2.4.1 Basic Principles

Ultrasonic imaging measures the reflection, transmission, or backscattering of an emitted ultrasound pulse depending on the configuration used, e.g. through transmission, pulse-echo testing, or resonance testing [35]. In this investigation, immersion through-transmission and pulse-echo testing were used and are explained in detail in Chapter 3.3.

There are two types of ultrasonic testing technique: the pulse-echo technique, where the transducer sends out a pulse and the same transducer receives the energy reflected at each interface, including cracks, delamination, and any imperfections within the sample [81], and through transmission techniques, where a transducer emits a signal which propagates through a sample, and a second transducer on the other side of the sample receives the transmitted signal [1,82]. The pulse-echo technique is more suitable for large defect detection and localisation; however, it has a limited detection capability for consecutive defects through the specimen depth. The through transmission technique, where the two probes are kept at a fixed distance from the object, is more suitable for irregular and thicker samples, as the transmitted signal is measured [83]. Both testing modes can be achieved through contact ultrasonic testing, or alternatively, through immersion ultrasonics [1,7]. Different scan modes (A-scan, B-scan, C-scan) were used in this investigation and are discussed in more depth in Chapter 3.

2.4.2 Ultrasonic NDT for Fibre Reinforced Composite Plates

Immersion C-scan ultrasonics are most often used to detect defects and delaminations in the plane normal to the emitted ultrasonic waves. Cracks oriented parallel to the emitted waves are unlikely to be observed [7], and the use of oblique incidence signal is needed. For low frequencies, ranging between 1 and 10 MHz, defects can be observed but only roughly located within the laminate. At higher frequencies, ranging up to 20 MHz, the wavelength becomes smaller than the average thickness of a single lamina (70-80 μm), thus individual lamina can be differentiated, and delaminations can be localised more precisely. Moreover, by increasing the frequency, the defect definition becomes higher, however the signal attenuation also increases [7].

In immersion C-scan ultrasound testing, damage is often assessed as a function of attenuation, as the pocket of air in a delamination results in strong reflection of the signal at the interface, which can also be used to locate the delamination through the thickness of the sample [84]; cracks lead to reflection and scattering of the incident wave [7]. Ultrasonic immersion C-scan imaging was used to find a relation between the degree of bending-fatigue damage and both ultrasonic attenuation coefficient and velocity in carbon epoxy pre-preg cross-ply composite plates [85]. A relation was found between the damage and ultrasonic properties, where the ultrasonic velocity was observed to be decreasing with increased damage, whereas the attenuation coefficient was observed to be increased. The porosity in different composite plates was detected though immersion double-through transmission, and the effect on the received signal was quantified by measuring variations in phase velocity and signal attenuation [50,68,86]. In [87–89], through-transmission ultrasonic signal attenuation was used for the quantification of porosity instead. In all cited studies, a correlation between ultrasonic attenuation and porosity was observed. In [86], this correlation was observed using the ultrasonic double-through transmission technique on both unidirectional and cross-ply composite plates. In [50], it was found that the attenuation as a function of the porosity was higher for unidirectional plates, as the porosity shape in those plates is flatter and longer than the spherical voids in plates with multidirectional fibre orientation, thus blocking the ultrasonic signal more efficiently.

C-scan ultrasonic imaging was used to develop an automated NDE system for the detection of manufacturing defects in composites [69]. The analysis allowed for the measurement of void volume fraction and fibre volume fraction, as well as the ply stacking sequence, fibre waviness and out-of-plane fibre wrinkling. Ultrasonic signal attenuation was used to define a maximum acceptable void content, as opposed to a maximum percentage of voids in the material, using different levels of voids and testing the cross-ply laminates under static and

fatigue load [52]. This tool can be used to predict the decrease in static strength and fatigue life due to the presence of voids. Immersion C-scan imaging was used for the detection of matrix damage in cross-ply composite plates, showing combined normal and oblique incidence scanning, as well as the presence and extent of both matrix cracks and delamination [38]. To address the ultrasonic limitation of detecting damage parallel to the incident beam, oblique incidence was used, allowing for a better detection and localisation of matrix cracks. In [68], the relation of wave velocity and attenuation versus frequency was investigated. It was found that the velocity dispersion increased as the frequency decreased. It was also found that the velocity decreases with increased void content. In [90], the relation between porosity content and amplitude using different types of transducers was investigated for unidirectional and quasi-isotropic curved-corner CFRP using the pulse-echo mode. It included non-focussed, point-focussed and line-focussed transducers. It was shown that focused transducers provide a clearer representation of both laminates, and that the influence from the porosity is visible in both focussed and unfocused transducers, although the porosity content can be better evaluated using the focussed transducers. In [54], through transmission ultrasonics was used to detect and localise damage in quasi-isotropic carbon epoxy pre-preg composite plates. The damage was detected using the variations in signal amplitude across the sample, as damage causes a reduction in signal amplitude. The localisation of the damage within the sample in terms of relative depth was achieved by measuring the ultrasonic echo delay. [91] characterised the reflections and fluctuations in the received signal obtained from different features in a composite laminate, such as the front and back surface, the inter-ply resin layers, delaminations and wrinkling, as functions of the amplitude, phase, and frequency of the signal. Delaminations manifest with a peak which is higher than the back surface signal, but with the same phase and frequency as the back surface.

Ultrasonic imaging is an established NDE technique that is often used for damage assessment in composite materials, including voids, irregular fibre volume fraction, ply stacking sequence, fibre waviness, and out-of-plane fibre wrinkling [69,91]. Thanks to its accuracy in the detection and localisation of defects and being the main NDE method in the aerospace industry, it was chosen as a reference for the new X-ray imaging technique. Ultrasonic imaging, however, does present a few disadvantages, the main one being its limited resolution. As mentioned, this is due to signal attenuation increasing with increasing frequency, which means a trade-off between resolution and inspection depth is often required. Small features such as micro-defects or individual fibres cannot be resolved in composite plates using ultrasonic imaging. Another disadvantage of ultrasonic C-scan imaging is its limitation for the detection of multiple defects across the thickness of the sample, as a large fraction of the signal reflects or scatters at the first defect [7].

2.5 Conventional X-Ray Imaging

Radiography was one of the earliest non-destructive evaluation techniques used in material science. It was first applied on metals and alloys to study their structural integrity and look for manufacturing defects, such as voids. Later on, this technique was expanded to the study of impact damage in composite materials [77].

2.5.1 Basic Principles

The physical principles used for contrast formation in conventional X-ray imaging has been the same since the discovery of X-rays by Rontgen in 1895, despite the considerable progress achieved in the technology since the first radiograph. This contrast mechanism relies on the difference in the attenuation coefficients of the different materials being imaged. The attenuation contrast C is defined as:

$$C = \frac{I_1 - I_2}{I_1} \tag{2-1}$$

Where I_2 is the intensity transmitted through a detail and I_1 is the intensity transmitted through the material surrounding that detail, as shown in Fig. 2-2.

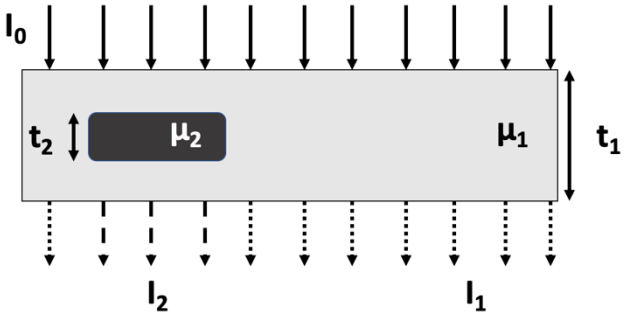

Figure 2-2 *Contrast mechanism in conventional X-ray imaging.*

The intensity transmitted through a material I_1 follows the Beer-Lambert's Law:

$$I_1 = I_0 e^{-\mu_1 * t_1} \tag{2-2}$$

Where I_0 is the incident X-ray intensity, t_1 is the thickness of the material through which the X-rays are propagating and μ_1 is the attenuation coefficient of that material [10,92]. This principle was used across many applications, including as an NDE technique for damage detection in composite plates, both with planar and 3D CT imaging. X-ray imaging, and in particular X-ray CT imaging, is one of the most widely used NDE techniques for damage detection in CFRP plates and is often used as a confirmation tool for other NDE techniques, as it offers high resolution, and allows to detect damage to a better extent than other NDE techniques.

2.5.2 X-ray Imaging for damage detection in fibre reinforced composite plates

Planar radiography is most useful for the detection of cracks and fibre failure if the resolution is high enough [1,6]. X-ray CT results in the production of a 3D cross-section image of the sample, which can detect defects such as delaminations, porosity, or cracks that are much harder to visualise in 2D images, and allows the visualisation of the whole structure. The extent of the detectable damage is limited by the resolution of the system. CT systems have some disadvantages, such as considerably long acquisition time and limitations in sample size [1,6].

For conventional radiography, X-ray CT is the most common imaging technique for composite damage characterisation [8,41,70]. Features detected using X-ray CT include inhomogeneities, cracks, and voids [8,93,94]. It is also widely used for porosity detection and quantification, as it offers the most precise visualisation of porosity distribution, morphology and size [95–97]. It provides more information than planar images and, if the resolution is sufficiently high, it allows the damage types to be determined, including e.g. delaminations which are not always visible in 2D X-ray images [1,6].

Another type of radiography used for damage detection in composite materials is penetrant enhanced radiography [98,99], which uses a liquid penetrant that is highly x-ray absorbing, and enhances the presence of micro cracks and fibre failures in the vicinity of the impact point of the composite [1]. Examples of X-ray opaque dye penetrant include zinc iodide (ZnI_2), which is used to enhance the contrast in the damaged areas of the sample [94]. The use of contrast agents for X-ray imaging was shown to enhance damage features, improving the detection of matrix cracks and delaminations [94,100–102]. The addition of contrast agents improved the detectability of small matrix cracks, as well as the characterisation of crack and microcracks networks within the sample [94,103]. However, the use of contrast

agents in X-ray imaging comes with a key disadvantage, which is the need for the dye to penetrate a defect to enable its detection, and the consequent impossibility to e.g. reach parts of the damage which are not directly connected to the main impact point.

There are many studies investigating different aspects of damage detection in composites using X-ray CT imaging, both manufacturing and in-service defects, and many new techniques and approaches are developed to improve the efficacy and capabilities of the imaging technique to allow for an even better understanding of the damage formation and propagation.

2.6 X-Ray Phase Contrast Imaging

For defects in composite materials too thin or too faint to cause sufficient variation in the detected intensity and invisible using conventional radiography, X-ray Phase Contrast imaging (XPCi) offers an advantageous alternative.

2.6.1 Basic Principles

Contrast creation in conventional X-ray imaging relies on the difference in the attenuation coefficients and the thicknesses of the different observable features. However, if the attenuation coefficients of two objects are very similar, or the thickness of a feature within an object is too thin to noticeably vary the transmitted intensity, then the contrast between these objects will become negligible [10].

X-ray phase contrast imaging (XPCi) is different from conventional X-ray imaging as its physical properties rely on the real part of the refractive index, *n*, as opposed to the imaginary part used by conventional X-rays:

$$n = 1 - \delta + i\beta \tag{2-3}$$

where β is responsible for the attenuation properties of a material, and δ is responsible for the phase shift, ϕ, the X-ray suffer when going through said material. δ is a function of the material's electron density, ρ_e, and depends on the X-ray wavelength, λ.

$$\delta = \frac{r_e \rho_e \lambda^2}{2\pi} \tag{2-4}$$

where r_e is the classical electron radius. For most materials and across most energies, δ is much larger than β, so its effect on the refractive index, n, dominates over β, and thus can lead to a greater contrast than attenuation-based imaging. Changes in phase have always been present in X-ray imaging but were not observed due to the inadequacy of the used experimental setups. New experimental setups were thus created to allow for changes in phase to be converted into changes in detected intensity, which is what detectors are sensitive to. These changes are measured either by detecting interference patterns, or, alternatively, by exploiting X-ray refraction [10].

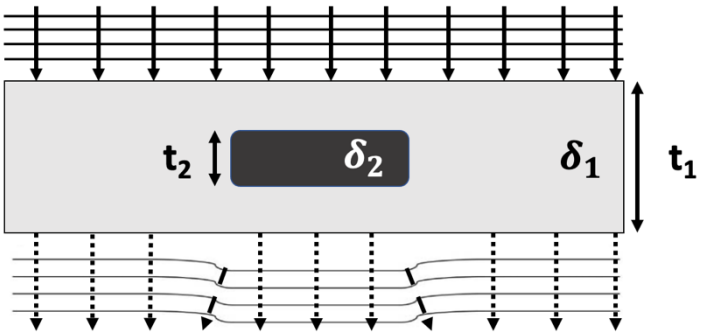

Figure 2-3 *X-ray interaction with a material, inducing a change in the wave front and a distortion which translates into a local change in the direction of propagation of the X-rays.*

When one considers an incident X-ray as a wave front, a detail in an object will cause a change in the wave front, resulting in either a locally advanced or delayed wave front (depending on the value of δ) with respect to its surroundings, as seen in Fig. 2-3. In order to detect the interference effects caused by this distortion, the wave is either

allowed to propagate through a large enough distance to allow for an interference pattern to form between the perturbed and unperturbed parts of the wave front, or the perturbed wave front is recombined with its unperturbed version in an interferometer [10].

Another way to detect phase changes is by looking for changes in the X-ray propagation direction, as a change in the wave front will cause a small local change in the X-ray propagation direction, due to the latter always being locally orthogonal to the wave front. This is X-ray refraction, which is dependent on the variation (namely on the first derivative) of the phase shift.

$$\phi(\mathrm{x},\mathrm{y}) = \frac{2\pi}{\lambda}\int_{object}\delta(x,y,z)dz \tag{2-5}$$

$$\Delta\theta_R \cong \frac{\lambda}{2\pi}\nabla_{x,y}\phi \tag{2-6}$$

where z is the direction of propagation of the X-rays, and $\Delta\theta_R$ is the refraction angle. Approaches exploiting refraction to detect phase effects are referred to as the differential phase methods. The detection of x-rays refracted in opposite directions at either side of an object typically leads to dark and bright fringes in the image [10]; their dependence of the first derivative of the phase change means their integration yields the phase shift [104].

2.6.2 Different XPCI Methods

Several methods were developed for XPCi, the first being the Bonse-Hart interferometer, which was originally presented in 1965 [10,105]. Other techniques include the analyser-based imaging technique [106], the free-space propagation technique [8,9], and the Talbot-Lau (or "grating") interferometry technique [107–109]. A detailed description of these techniques lies beyond the scope of this thesis work and can be found in [10,105]. These techniques impose several limitations, including high sensitivity to vibrations, long exposure times and thus

high dose delivery, and often limited fields of view. Some also impose the use of a monochromatic x-ray beam. Edge Illumination XPCi aims to solve most of these limitations [110].

2.6.3 Edge Illumination XPCI

Edge Illumination (EI) XPCi is a differential phase technique which relies on the X-ray beam only illuminating the edge of the pixel's active surface, in order to only partially detect the primary photons [110]. If one assumes a vertically thinned beam and a detector composed of a single row of pixels, with only a fraction of each pixel exposed to the incoming primary photons, images can be obtained by vertically scanning an object, as is shown in Figure 2-4.

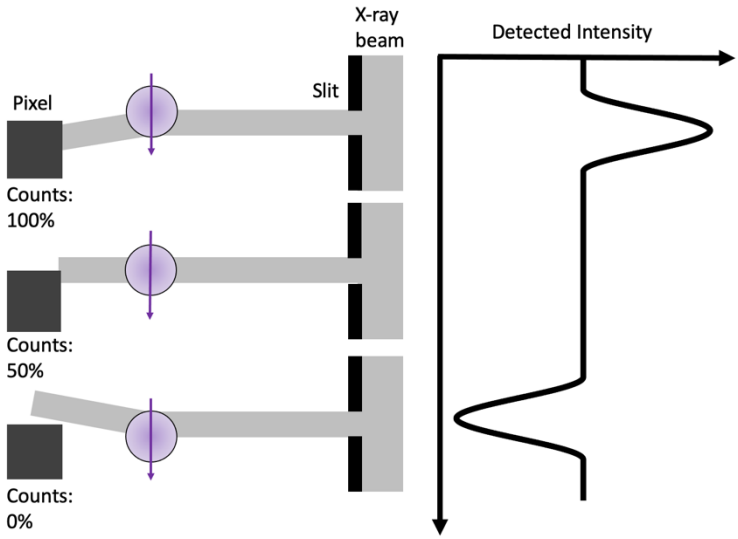

Figure 2-4 *Contrast mechanism in aperture-based phase contrast X-ray imaging.*

Any gradient in the refractive index, *n*, caused by the introduction of the sample in the beam will result in the deflection of the beam, and thus lead to a change in the detected intensity. If the beam is deflected upwards, a larger fraction of the beam will be deviated outside of the sensitive part of the detector, and thus the detected intensity will decrease, resulting in a negative (dark) fringe. Alternatively, if the beam is deflected downwards, the opposite effect will take place, and photons which do not normally hit the sensitive part of the pixel are

deviated inside, resulting in an increase of the detected intensity, i.e. a positive (bright) fringe [10,110].

In order to implement this technique in a laboratory and use a 2-dimensional detector instead of a single row of pixels combined with sample scanning, two apertured mask systems were introduced [110,111], as shown in Fig. 2-5. The detector mask is identical to the sample mask, apart from the scaling factor which accounts for beam divergence. A first mask, referred to as the sample mask, was placed upstream of the imaged sample, splitting the beam into an array of individual beamlets. The beamlets were kept separated by a distance of about half a pixel (usually a few tens of μm), to prevent them from overlapping at the detector which would reduce the detected refraction signal. The second mask, referred to as the detector mask, was placed in contact with the detector, thus making the regions separating adjacent pixels insensitive to incoming X-rays, and replicating the scenario above where only a fraction of each beamlet is detected by the pixel. The characteristics of the EI XPCi measurement (source, masks and detector) had been optimised before the start of the project as it's optimisation is a function of the system's characteristics as opposed to the sample used [112]. The system was only sensitive to the phase effects in one direction (i.e., upwards/downwards or left/right) [10,110].

Using the acquisition of at least three images with different sample mask positions relative to the detector mask, this method allows for the quantitative retrieval of attenuation, differential phase (refraction) and dark field (scattering) images [113,114], the latter being a representation of ultra-small angle scattering generated by sample features on the sub-pixel scale [11]. A full description of the phase retrieval process is provided in Chapter 3.4.2.

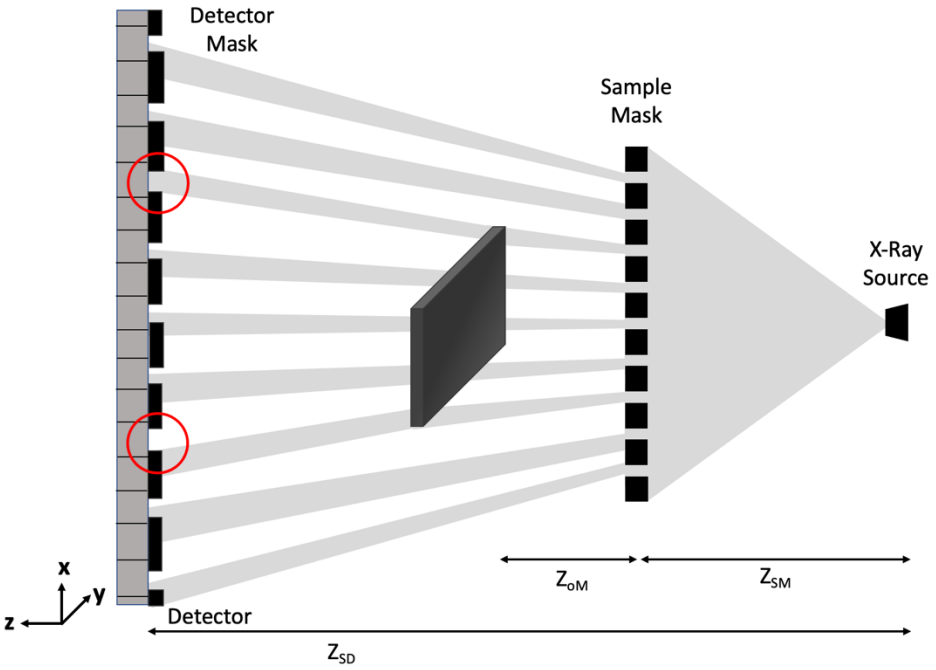

Figure 2-5 Schematic of the concept of EI XPCi implemented with a conventional X-ray source.

The EI method is robust against X-ray energy increase, and is able to achieve an angular resolution down to a few hundreds of nanoradians in standard laboratory environments [115,116]. In a synchrotron environment, a much higher angular resolution can be achieved, down to a few nanoradians, for both high and low energies [117]. It is also robust against environmental vibrations, thus allowing it to be used in a laboratory environment [10,11]. Other advantages of this method include the possibility of using divergent and polychromatic beams [118], as well as its relative insensitivity to increasing focal spot and pixel size, which is not the case with most other XPCi methods [119]. EI XPCi offers advantages for industrial applications, as it is easy to implement for large fields of view: a pre-commercial system with a field of view of 200*500 mm^2 has been developed and is used at the Nikon facilities in Tring [120].

2.6.4 XPCi for damage detection in CFRP

Most of the research that investigates composite materials using XPCi involves free space propagation or grating interferometry phase

contrast imaging techniques, performed using both synchrotron radiation and in a laboratory environment. Free space propagation involves placing the detector far from the sample in order to allow for an interference pattern to form between perturbed and unperturbed wave fronts when a sample is placed in the beam [10], and can be used to study composite materials and their defects. In [8], third generation synchrotron radiation was used to image cracked silicon carbide (SiC) macro-fibres in a composite plate. This was benchmarked against conventional X-ray imaging. It was shown that phase contrast imaging was more sensitive to the variations in inhomogeneity and detected voids in the composite plate much better than attenuation-based X-ray imaging. In [121], grating-based XPCi was used for the detection of delamination in an L-shaped CFRP using planar imaging, which were not necessarily detected using conventional X-ray CT.

XPCi is highly sensitive to porosity, boundaries between materials and defects in composite materials. XPCi is also more sensitive to low density materials in comparison with conventional X-rays. Phase enhanced X-rays were used to observe individual carbon fibres in a CFRP, as well as for the analysis of fibre orientation in glass fibre reinforced composite plates [122]. Free-space propagation XPCi was performed on short carbon fibre-reinforced polymeric composite materials, allowing for the reconstruction of the different parts of the composite and for a full anisotropy analysis of the short fibre orientations [9]. Due to the carbon-based nature of both the fibres and the polymer matrix, conventional X-rays resulted in low contrast which prevented the separation of fibres and defects from their surroundings. The same was done in [108] for woven CFRP using grating interferometry.

In [123], free space propagation XPCi was used to separate the different phases within a composite plate, i.e., the matrix and the carbon fibres from the porosity present in the sample, which was

unachievable with conventional X-ray imaging. XPCi was previously used for the detection of porosity in aluminium welds using dark field CT [107] based on Talbot-Lau interferometry. The latter technique was used to perform CT scans on carbon and glass fiber reinforced composite plates, investigating all three (attenuation, differential phase and dark-field) signals [124]. The differential phase signal showed an increased contrast between matrix regions with higher and lower porosity, helping to visualize the pores better, but not to quantify them. A similar investigation was conducted for the detection of porosity in concrete [125]. Overall, these studies show that the complementarity of the phase-based signals allows for a better detection of inhomogeneities such as pores than can be obtained with conventional radiography. However, the option to detect and quantify porosity with planar (2D) XPCi was never explored. This would have advantages as 2D imaging is much faster than CT, removes limitations on sample size [120], and is compatible with online inspection.

The need for improved scanning is of real importance, and the advancement of XPCi is allowing for the development of a compact scanner-type XPCi system, using Talbot-Lau interferometry, for examination of objects on conveyor systems [126]. The system was used for the examination of a CFRP specimen, which allowed to map the degree of anisotropy of the fibres in the plate by scanning it three times with different sample orientations. Grating interferometry X-ray CT was also used for the inspection of bonded repairs of CFRP in civil aircrafts, with the multimodal imaging allowing for the detection of the repair bond's constituents, as well as the fibre bundles alignments [127].

2.7 Comparison of NDE Techniques

Most of the comparisons between radiographic imaging and ultrasonic imaging techniques involved X-ray CT imaging and longitudinal C-scan ultrasonic imaging. Comparisons involving radiographic imaging

and ultrasonic imaging techniques were performed to study the evolution of damage (cracks, delaminations) in self-healing composites (composites containing a fraction of hollow micro-fibre, which results in the composite's capacity for self-healing)[71], for the detection of BVID in composites (e.g. matrix and fibre cracks, debonding and fibre pullout) [128], as well as the evaluation of porosity content in composites plates, which is more difficult to estimate using ultrasonic imaging alone [129]. Both imaging methods are capable of detecting damage in fibre-reinforced composite plates, with X-ray CT imaging offering higher resolutions and capable of detecting micro-damage and individual plies, up to the detection of individual fibres [71,128,130].

In [131], ply orientation and wrinkling was mapped and characterised in CFRP using ultrasonic imaging by presenting new segmentation methods, which was then confirmed using X-ray CT imaging. The same was done in [132] for matrix cracks, micro-buckling, fibre breakage and void volume quantification. In [18], ultrasonic signal attenuation was compared with X-ray CT imaging for the quantification of porosity in composite plates, showing a correlation between the two imaging methods and increasing porosity.

In [71], both ultrasonic C-scan imaging and X-ray micro-tomography were used to study the evolution of BVID for low velocity impacts on self-healing composite materials. Both the CT imaging and the C-scans showed a consistent increase in the damage shape with increasing impact energy. The C-scan proved to be of limited resolution, meaning some damage, such as micro-cracks, or even the distinction between the individual fibres, can go undetected. However, this method is still capable of showing the maximum extent of the damage in the plane of the specimen. The CT images could detect both delaminations and all cracks, as well as individual glass fibres, due to its higher resolution. The full extent of the damage within the

composite was extracted and allowed for an improved visualisation of the failure patterns.

Another comparison between conventional X-ray micro-CT and ultrasonic C-scans was investigated in [128], imaging both matrix and fibre defects in composite plates with different fibre orientations, including matrix and fibre cracking, matrix debonding and fibre pullout. The investigated composite plates were of silicon carbide fibre with silicon nitride matrix, including unidirectional plates with varying number of plies and a cross-ply plate. Immersion C-scan was used with transducers with frequencies ranging from 5 to 50 MHz. The aim was to differentiate the fibres and matrix components with both X-ray CT, where the two materials have similar absorption characteristics, and with immersion ultrasonic C-scans, where the two materials have similar acoustic impedances. X-ray CT was able to detect defects such as voids with a diameter larger than the fibre diameter, fibre pullout, matrix and fibre cracks, and fibre matrix debonding. Ply by ply information was obtained and the fibre layout was extracted. However, the obtained contrast was not high enough to differentiate between the individual fibres and their matrix environment. As for immersion C-scans, the fibre layout was observed both on the surface and internally, and defects such as fibre debonding and matrix cracks were also observed. However, fibre pullout below the surface could not be unambiguously determined, even at high frequencies. In [18], a quantitative comparison between X-ray CT and immersion ultrasonic imaging was performed to evaluate defect distribution in ceramic matrix composite plates. The plates used included a woven and a cross-ply composite plate. A reasonable correlation between the CT and ultrasonic images was found for the detection of porosity and internal flaws within the composite plates.

Other comparisons often found in the literature are between different X-ray imaging techniques, including XPCi: In [94,98], contrast agent X-ray CT imaging was compared to conventional X-ray CT imaging and XPCi CT for crack detection in CFRP, showing that, while the use

of contrast agents in X-ray CT improves the contrast and detectability of cracks relative to conventional imaging, it is limited as it can only highlight surface breaking defects. This is not the case for XPCi, which can detect the cracks better than the other two techniques thanks to its inherent enhancement of the interfaces that form at cracks. In [133], grating-based XPCi CT (voxel size 43 μm^3) was used to investigate the degree of anisotropy of fibres in glass fibre reinforced polymers through the dark field signal, and compare it with conventional X-ray CT imaging (voxel size 6.5 μm^3). It was shown that the dark field signal could characterise the different fibre orientation and their properties comparably to the high-resolution X-ray CT scan.

A few studies comparing XPCi and ultrasonic imaging have been carried out in the literature. The first was the EVITA (Non-Destructive EValuation, Inspection and Testing of Primary Aeronautical Composite Structures) project, funded by the European Union [134]. In this project, two ultrasonic imaging methods, immersion through-transmission imaging and phased array pulse-echo imaging, were used to benchmark grating interferometry XPCi as a viable NDE technique. The samples were advanced carbon fibre epoxy pre-preg composites with different low impact damage defects, including cracks and porosity. The dark field images proved to be highly sensitive to porosity in the samples, as they lead to a change in fibre arrangement. Crack detection was also achievable using XPCi and was quantified, with the average crack density and shape measured. All the results obtained were benchmarked against other established NDE techniques, including ultrasonic imaging techniques. It was observed that even though both XPCi and ultrasonic imaging were able to observe porosity in the sample, XPCi offered a much better quantification than the ultrasonic phased array and through-transmission techniques. In [135], both planar and CT grating-based XPCi was used to detect and identify micro-cracks in CFRP, and compared with conventional X-ray CT and ultrasonic pulse-echo imaging. It was shown that the addition of dark field imaging allowed

for a better identification and quantification of damage in the structures, as well as the detection of interlaminar delamination and intralaminar cracks, which were not visible in the other standard NDE methods. Lastly, in [136,137], ultrasonic C-scans and EI XPCi were used to characterise low velocity impact damage in a cross-ply composite plate. It was observed that the ultrasonic C-scan imaging was able to detect defects such as delaminations and macro-cracks. The phase-based X-ray images, and the dark field images particularly, presented an advantage in detecting much smaller defects, such as micro-cracks and debonding. The images were also compared with conventional X-ray images, and a clear advantage was observed in the XPCi images, as several defects visible in the phase enhanced images were not visible in the conventional X-ray ones.

2.8 Scientific gap and Motivation

CFRP are widely used across several industries and are becoming more popular every year. However, due to their brittle nature, the need for efficient, non-destructive monitoring of such structures is of utmost importance. Whilst the current methods (mostly ultrasonic and conventional X-ray CT imaging) offer good detection capabilities of damage in CFRP, they have disadvantages. Ultrasonic imaging is easy to setup and can be used *in-situ*, but encounters difficulties to identify multiple defects across the thickness of the sample, as well as micro-defects, and requires compromises on resolution for the analysis of thicker specimens. Conventional X-ray imaging offers high resolution imaging, but encounters severe limitations in terms of detecting defects using 2D planar imaging. As a result, time-consuming X-ray computed tomography (X-ray CT) scans need to be performed for better visualisation of damage, which also imposes smaller specimen sizes. Moreover, in CFRP contrast limitations exist due to similarities between the attenuation coefficients, leading to more difficulties in resolving features [6].

XPCi offers an advantageous approach as it offers two new phase-based signals in addition to the conventional attenuation signal, which were proven to detect fibre anisotropy and damage in CFRP in previous studies. However, the XPCi methods used in these investigations are more difficult to implement and were mostly performed at synchrotron facilities. As EI XPCi is easier to implement in a laboratory environment and with standard X-ray sources, it offers a degree of increased robustness compared to other XPCi methods. It was thus chosen as the ideal candidate for the benchmarking of a new, viable NDE method for damage detection in CFRP. This benchmarking is achieved by comparing EI XPCi to the most commonly used NDE techniques in industry, i.e. ultrasonic and conventional X-ray imaging. This allows to demonstrate EI XPCI capabilities for damage detection, for both in-service defects and manufacturing defects.

2.9 Conclusion

This chapter introduced composites materials, manufacturing processes and different defect types occurring during manufacturing and in-service. The different NDE techniques used for the detection of such damage were described, with a focus on ultrasonic imaging and conventional X-ray imaging. A state-of-the-art review of the research involving these two techniques for damage detection was presented, highlighting the advantages and disadvantages of each technique. The concept of X-ray Phase Contrast Imaging, and of Edge Illumination XPCi was introduced, with their basic principles explained. A review of the research using different XPCi techniques for damage detection in composites was described, along with a list of investigations comparing the extent of damage detectable in composites using XPCi methods to conventional NDE techniques, more specifically ultrasonic imaging, and conventional X-ray imaging.

3 Experimental Methodology: Ultrasonic Immersion C-Scan Imaging and Edge Illumination X-ray Phase Contrast Imaging

3.1 Introduction

This chapter presents details of the different experimental setups of the used imaging systems, i.e., Edge Illumination X-ray Phase Contrast and ultrasonic immersion C-scan imaging. Additional techniques were used for confirmation of the observations made using XPCi, as they are often used for defect detection and analysis in fibre reinforced composites. These are described in the respective chapters in which they are used, along with the description of the used specimens. New image analysis tools are presented here, aimed at correcting artefacts from source and mask movements during the EI XPCi image acquisitions.

3.2 Specimens

Three types of specimens were used in this study to investigate different defects induced in fibre-reinforced composite plates. The first was supplied by Nikon and was a small cross-ply CFRP plate with severe impact damage, including a 4mm diameter indent visible on the surface; the second sample was supplied by the Composite System Innovation Centre at the University of Sheffield and was a larger cross-ply CFRP with impact damage induced using a hemisphere with an impact energy of 7.4J[138]. The final series of specimens, consisting of 9 plates, was provided by the National Composites Certification and Evaluation Facility (NCCEF) at the University of Manchester, and was originally produced for Rolls Royce. The plates were cross-ply woven CFRP with porosity varying between 0.7% and 10.7% deliberately induced during manufacturing. All specimens are further described in the respective chapter in which they are used, with more details about manufacturing and the damage inducing processes.

3.3 Ultrasonic imaging

Ultrasonic imaging is widely used for the NDE of composite plates in industry. In this study, immersion ultrasonic imaging was chosen as it is the most common NDE technique used for assessing damage extent in composite plates. Two imaging methods were used to inspect those: pulse-echo double through transmission and through transmission.

3.3.1 Double Through Transmission

In the pulse-echo double through transmission imaging method, a transducer acts as both the transmitter and the receiver of the ultrasonic signal [139,140]. The transducer, immersed in water, emits a short ultrasonic pulse which propagates through the water to the specimen and a metal reflector plate placed underneath it. The signal is reflected by the metal reflector and goes through the specimen a second time before being captured by the transducer [82,141]. The transducer is connected to a pulser/receiver unit (Panametrics 5601T), an oscilloscope (LeCroy 9304), and a positioning system, which moved the transducer across the sample. A thick stainless-steel plate was positioned at the bottom of the water tank and served as a metal reflector. The composite specimen was placed a distance D_c above the surface of the steel plate, as shown in Fig. 3-1. This distance was chosen considering that a few wavelengths allow for a clear time separation of the double through transmission signal and the pulse-echo signal reflected from the composite specimen [140].

Various transducers, with different frequencies (10 MHz to 30 MHz), focal spots and beam diameters were used. For the focussed transducers, the correct positioning at the focal length F_z with respect to the sample was achieved using the wave velocity in water and by calculating the expected pulse arrival time, using Equation 3-1.

$$v = \frac{2F_z}{t} = \lambda * f \tag{3-1}$$

Where v is the wave velocity, λ is the wavelength, t is the pulse arrival time, and f is the transducer centre frequency. The wave velocity in water is assumed as 1500m/s [142]. This velocity can easily be verified by moving the transducer a known distance from the specimen and measuring the change in arrival time of the reflected signal.

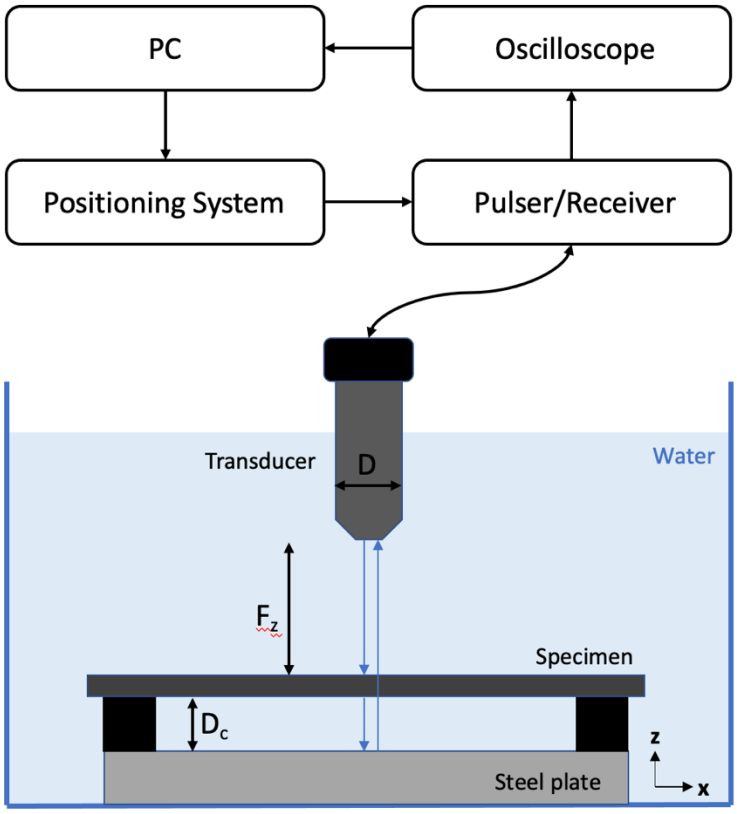

Figure 3-1 *Experimental setup of the immersion double through transmission imaging technique.*

The focussed beam diameter, D_f, of the transducer, was calculated using Equation 3-2, to decide on a sensible step size for the transducers. The average step size for the pulse-echo double through transmission scans was approximately 200μm for the specimens studied here.

$$D_f = 1.44 \frac{F_z \lambda}{D} \tag{3-2}$$

where D is the transducer diameter. A longitudinal wave was emitted from the transducer and the reflections from both the immersed specimen and reflector steel plate were recorded, producing A-scans, as is shown in Fig. 3-2, which were saved as Matlab files.

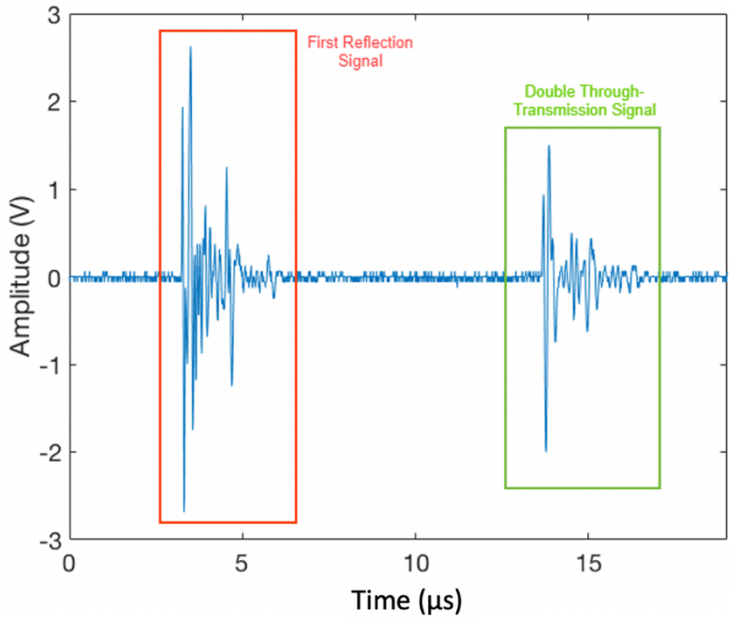

Figure 3-2 *Time-gated A-scan obtained from immersion double through transmission scan of the Nikon composite sample, showing a first reflection from the plate, and a second reflection from the reflector steel plate.*

A-scans are representations of the amplitude of the received signal as a function of time, for different locations across a given sample. Two different types of measurements were extracted from each A-scan. The earlier signal is attributed to the first reflection in the A-scans, which arises from the reflection of the incident wave from the composite plate itself, and was used to produce B- and C-scans. C-scans are a surface representation of the sample obtained by plotting the peak amplitude of the received signal within a chosen arrival time window. B-scans are transversal cuts through the sample, obtained by plotting a sequence of A-scans along a given direction, showing color-

coded variations in the reflected amplitudes. B-scans are used to represent the different plies and possible damage within the sample, including features that are not necessarily visible from C-scans due to their orientation (i.e., parallel as opposed to perpendicular to the beam). The maximum amplitude of the second pulse in the A-scan was extracted, which corresponds to a double-through transmission measurement, i.e., the reflection of the wave from the surface of the steel plate, having propagated twice through the composite specimen. This gives an indication of the cumulative damage across the thickness of the sample, and was used to detect delaminations within the sample (areas of very low detected amplitude), and the presence of other types of severe damage (e.g. cracks) [12].

The C-scans produced for the composite sample were obtained by plotting either the positive maximum or negative minimum of the time-gated A-scans. The choice between the positive maximum or the negative minimum depended on the mismatch in the acoustic impedance of the different components involved [83], as shown in Equation 3-3:

$$R = \frac{Z_2 - Z_1}{Z_2 + Z_1} \tag{3-3}$$

Where R is the normal incidence reflection factor, and Z_1 and Z_2 the acoustic impedance of the two media involved. When there is a high mismatch in acoustic impedance between two media, the fraction of the energy reflected at the interface is larger [143,144]. When looking at the difference in acoustic impedance between the two interfaces, a transition from a medium with high acoustic impedance (Z_1) to a medium with a lower acoustic impedance (Z_2) will result in a negative reflection amplitude (i.e., negative R), whereas the opposite will result in the use of the positive reflection. The acoustic impedance of water is $1.5*10^6$ $kgm^{-2}s^{-1}$, and for steel is $46*10^6$ $kgm^{-2}s^{-1}$ [145]. The acoustic impedance of a carbon-based composite plate is approximately 5.5-

$6.2*10^6$ ($kgm^{-2}s^{-1}$) [146]. The acoustic impedance, Z, of a medium, is a function of its density, $\boldsymbol{\rho}$, as well as the sound velocity, v, of the wave through the material, shown in Equation 3-4 [143,144]:

$$Z = \rho * v \tag{3-4}$$

As a result, using the respective densities and sound velocities in each individual component, the respective acoustic impedance can be calculated. For CFRP, the composite system and lay-up, as well as the fibre and matrix volume fractions need to be known to enable density and sound velocity estimations.

3.3.2 Through Transmission

The second scanning method used was single through transmission imaging. In this setup, two different transducers are used, one as a transmitter and the other as a receiver [68]. Here too both transducers are immersed in water; A signal is created by the pulser/receiver unit (Panametrics 5601T), which is then emitted by the transmitting transducer. The pulse then propagates through the water onto the specimen. The transmitted signal is then captured by the receiving transducer, which is also connected to the pulser/receiver unit, and the output signal is displayed by an oscilloscope (LeCroy 9304), as shown in Fig. 3-3. Unlike with the double through transmission measurements, the sample was positioned vertically, and was scanned along the y- and z-axes.

The single through transmission imaging method was used for the porosity specimens, since the presence of porosity leads to an attenuation of the signal, as it is scattered by the small voids [12]. A series of transducers of varying frequencies (2.5 MHz to 5 MHz) were used for comparing the relation between frequency and signal attenuation. Both unfocussed and focussed transducers were used on the porosity specimens. The unfocussed transducers were both

placed at a distance away from the sample beyond the near field distance of the transducers. The near field corresponds to the area where the beam amplitude fluctuates, and the near field distance is the point at which the beam becomes uniform and is at its maximum strength, allowing optimal detection [147]. The near field distance is given by

$$N = \frac{D^2}{4\lambda} = \frac{D^2 f}{4v} \tag{3-5}$$

Where D is the beam diameter, λ is the signal's wavelength, f is its frequency and v is the wave velocity. In water, this velocity is approximately 1500m/s [148]. For both the single through transmission and double through transmission measurements, the focussed transducers were placed at a distance equal to the focal length of the transducers.

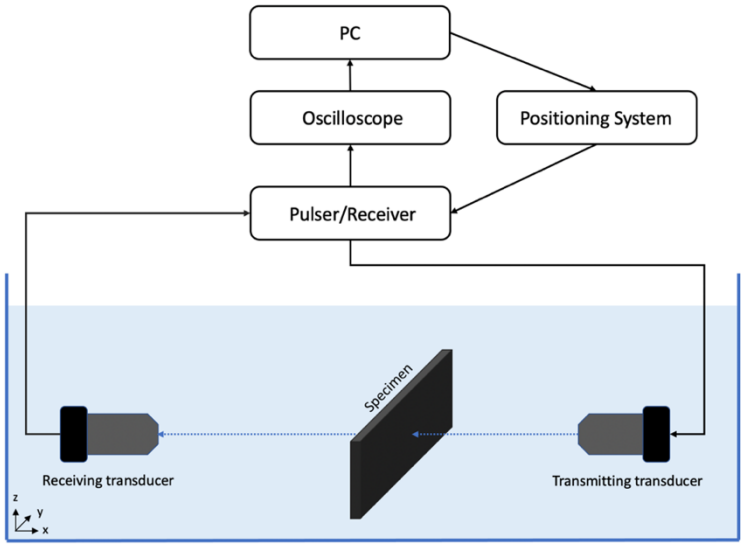

Figure 3-3 *Single through transmission experimental setup.*

Here too, full A-scans of the received signal were recorded at each measurement point; however, this time they represent the signal transmitted through the sample. From those A-scans, the signal attenuation (dB) in the plates was calculated. To measure the signal

attenuation of the plate, a first scan was acquired with no sample in the beam path. This was done to measure the average signal transmitted through water by measuring the maximum amplitude for each of the A-scans and taking the average. Once the average signal amplitude was calculated in water, it was then compared to the signal amplitude transmitted through each individual plate, and the signal attenuation was calculated as:

$$\Delta I\ (dB) = 20 \log \frac{V_{water}}{V_{plate}} \tag{3-6}$$

Where ΔI is the signal attenuation (dB), V_{water} and V_{plate} are the averages of the maximum signal amplitude through water (V) and through the specimen, respectively [52,86]. These signal attenuation values were calculated for each entire specimen for comparison with the manufacturer's values, for the investigation of the signal attenuations across different frequencies, and for the creation of C-scans representing the variation in signal attenuation across the plates. Small ROIs were also used for signal attenuation calculations for comparison with the X-ray signals and are discussed further in Chapter 6.

3.4 Edge Illumination X-ray Imaging

An Edge Illumination system was set up at UCL using apertured masks, as described in Chapter 2.6.3. It was used to acquire both planar and CT scans of the specimens.

3.4.1 Experimental Setup

The experimental setup of the Edge Illumination system at UCL included a Rigaku MicroMax 007 HF rotating anode molybdenum X-ray source. It features a 70 μm focal spot, and in this research was used with 40 kVp voltage and 20 mA current. The detector was a Hamamatsu C9732DK CMOS flat panel with a 50x50 μm^2 pixel size.

A CMOS sensor was selected in this setup as it offers direct coupling between sensor and scintillator, as well as a higher readout speed and a larger active surface than a CCD sensor. The source to detector distance (Z_{SD}) was 0.85m, with the sample placed on a stage 0.7 m away from the source, and the source to sample mask distance (Z_{SM}) of 0.65 m, as shown in Fig. 3-4. No special modifications were made to this system for this project, as it had already been optimised for previous experiments. System optimisation depends primarily on the systems components (source, detector and masks), and only marginally on the investigated samples, as long as they have similar attenuation characteristics and a comparable resolution level is required.

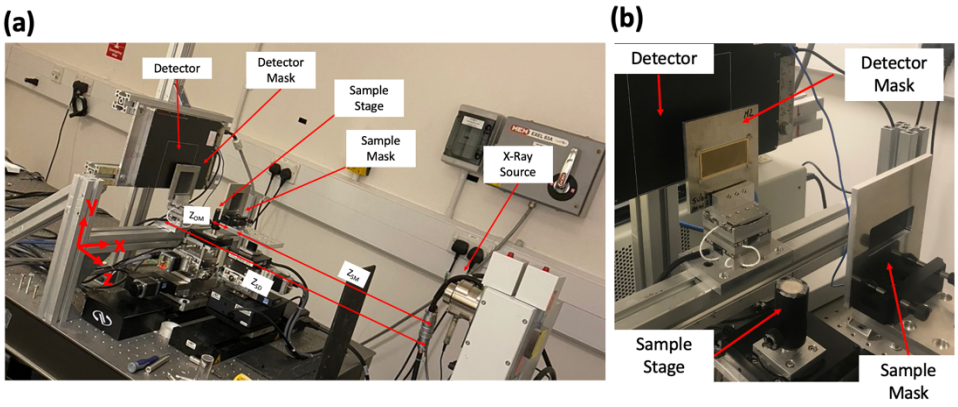

Figure 3-4 *(a) EI XPCi laboratory setup at UCL used in this project, showing the source, detector, sample stage and the set of apertured masks; (b) close up on sample mask, sample stage, detector mask and detector; the sample mask is placed upstream of the sample, and the detector mask placed in front of the detector.*

The two masks were placed between the source and the detector; the sample mask was placed upstream of the sample, 0.05 m away from the sample stage (Z_{MO}), and the detector mask was placed directly in front of the detector. The masks were made of gold on a graphite substrate and were fabricated by MicroWorks. The system's magnification, *M*, due to the divergence of the beam, and given by

$$M = {Z_{SD}}\Big/{(Z_{SM} + Z_{MO})} \tag{3-7}$$

and was calculated to be 1.214. The whole system was sensitive to phase variations in 1D along the x-direction. The detector mask is designed specifically for the detector used to match the pixel spacing. The sample mask size is determined by the system's magnification. The aperture size of the sample mask is chosen based on the desired resolution of the system. As with any X-ray system, there is a radiation risk which requires for the system to be in a shielded room or enclosure.

For the acquisitions of the severely damaged composite plate in Chapter 4, the sample mask used had an aperture of 12 μm and a period of 38 μm, and the detector mask has an aperture of 20 μm and a period of 48 μm. Those masks, in which every pixel has an aperture associated with it, are called non-skipped masks, and the detector mask design for a non-skipped system is shown in Fig. 3-5(b). As is the case with all indirect conversion x-ray detectors using a scintillator (as the Hamamatsu C9732DK does), the resolution is affected by cross-talk between neighbouring pixels, with 25% of the signal spreading in all directions to the next pixel, and a further 5% to the second neighbouring pixels [149], as shown in Fig. 3-5(a). EI XPCI offers an option to correct for this effect at the expense of resolution (or of scan time if "dithering" is used, see below) by doubling the mask period, with every other pixel becoming obscured by the mask septa. Such masks are called skipped masks, and this correction was introduced for the acquisitions of the cross-ply composite plate and the porosity specimen (Chapters 5 and 6, respectively).

The skipped mask concept is shown in Fig. 3-5(c), where the periods of the sample and detector masks were doubled, resulting in an aperture of 12 μm and a period of 78 μm for the "skipped" sample mask, and an aperture of 20 μm and period of 98μm for the "skipped" detector mask. This resulted in every other pixel being shadowed,

reducing the effect of cross talk between neighbouring pixels, and ultimately improving the system resolution when dithering is used.

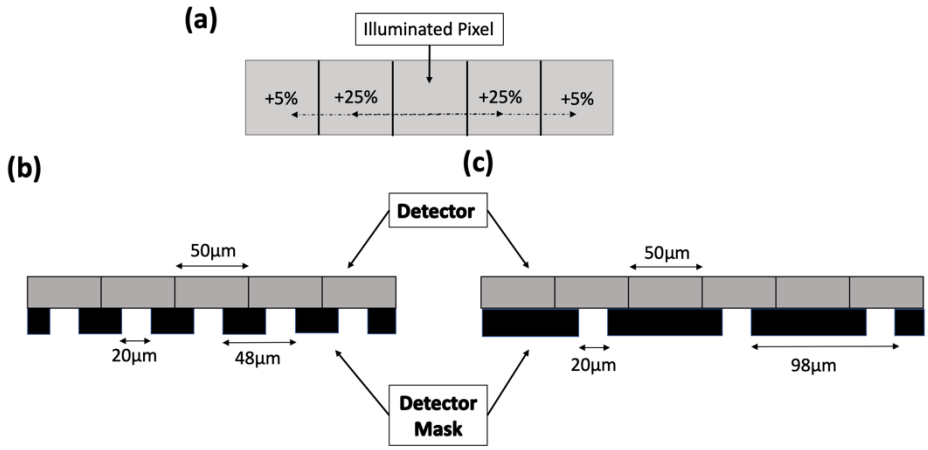

Figure 3-5 *Schematic of cross-talk between pixels (a) as well as comparison of non-skipped (b) and skipped masks (c) with respective aperture and period size compared to detector pixel size.*

The image acquisition process included the acquisition of a set of flat fields, which has to be repeated for every relative displacement of sample and detector masks. These displacements are used to obtain the illumination curve, which is a bell-shaped curve well approximated by a Gaussian, representing the variation of the detected intensity as a function of the sample mask position relative to the detector mask [10,92]. For the planar images of all samples involved, a selection of flat field images with 19 “points” along the illumination curve were taken, where a “point” corresponds to a chosen sample mask position relative to the detector mask. 19 points were taken in order to maximise the signal statistics of the scans. 9 points were taken symmetrically on each side with respect to the centre position (where the sample and detector masks are perfectly aligned and the detected intensity is maximised), corresponding to the top of the illumination curve. The step size of each sample mask position was 2 µm in the x-direction between each consecutive IC point. The sample was then mounted on a stage which could be moved along the x-axis. The sample data acquisition was carried out by taking 19 frames with the

sample mask positioned at the same relative positions as previously done for the illumination curve. In order to increase the resolution, the samples were also dithered, i.e., repositioned at sub-pixel locations, for each sample mask position [150]. The dithering step size was calculated using Equation 3-8:

$$Dithering\ step\ size = \frac{Sample\ mask\ period}{Number\ of\ dithering\ steps} * G \tag{3-8}$$

Where *G* is the geometric magnification between the sample stage and the sample mask position, with $G = 1.053$ for the EI XPCi setup used here. The dithered frames were then recombined to achieve an image with a higher resolution.

3.4.2 Phase Retrieval

The images acquired using the EI XPCi system described above contained a mix of signals from different contrast channels. A phase retrieval procedure was applied to the acquired images to extract the attenuation, differential phase, and dark field images of the sample. The principal phase retrieval method described here, discussed in [11], assumes that the illumination curve, defined as the variation in detected intensity as a function of the sample mask positions relative to the detector mask, can be represented by a Gaussian function. Fig. 3-6 shows a typical illumination curve obtained by scanning the sample mask with respect to the detector mask, without a sample in the beam, and measuring the corresponding intensities.

In an EI XPCi system, every pixel can be treated independently. In order to obtain the attenuation, differential phase and dark field images, a Gaussian, $I_N(x)$, is first fitted to the illumination curve measured in the absence of a sample:

$$I_N(x) = t_N \exp\left[-\frac{(x-\Delta x_N)^2}{2\sigma_N^2}\right] \quad (3\text{-}9)$$

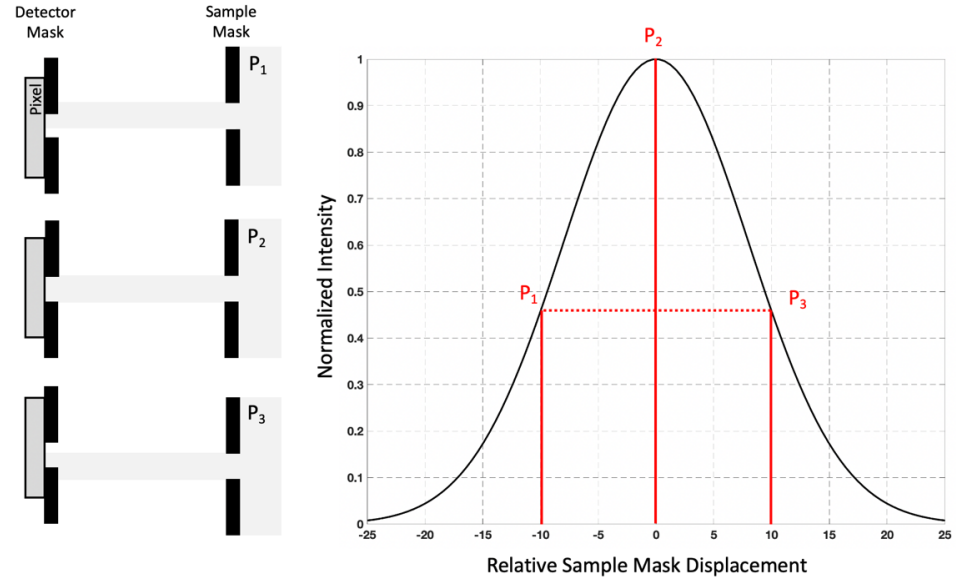

Figure 3-6 *Typical illumination curve obtained by scanning the sample mask with respect to the detector mask, showing variation in recorded intensity; the maximum intensity corresponding to the sample and detector being perfectly aligned, and the minimum intensity detected when they are out of phase.*

A second Gaussian, $I_M(x)$, is then fitted to a series of sample images acquired at different sample mask positions, such that, for each individual pixel:

$$I_M(x) = t_M * \left\{t_N \exp\left[-\frac{(x-\Delta x_M)^2}{2\sigma_M^2}\right]\right\} \quad (3\text{-}10)$$

where t_N and $t_N * t_M$ represent the areas of the curves, Δx_N, Δx_M the curve centres, and σ_N^2, σ_M^2 the curve widths obtained without and with the sample, respectively.

By comparing the three parameters of the Gaussians fitted with and without sample, the three channels can be obtained [151]. t_M represents the "conventional" attenuation image, while the refraction Δx_R and scatter images σ_0^2 are be obtained as:

$$\Delta x_R = \Delta x_M - \Delta x_N$$
$$\sigma_0^2 = \sigma_M^2 - \sigma_N^2 \quad (3\text{-}11)$$

In practice t_M represents the (relative) reduction in curve area, Δx_R its lateral shift, and σ_0^2 its relative broadening, as shown in Fig. 3-7. While in principle only three measurements at different sample mask displacements are needed to retrieve the three desired parameters, often more measurements are taken to increase the fit robustness.

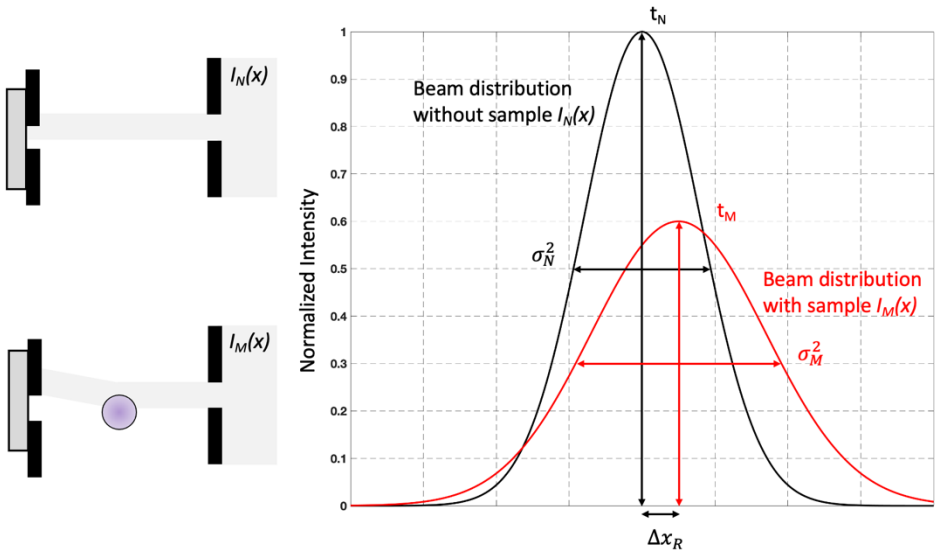

Figure 3-7 *Changes induced to the illumination curve due to the introduction of a sample into the beam, with the amplitude t_N decreased by absorption, the centre position of the Gaussian shifter by Δx_R by refraction and the broadening of the Gaussian by a factor σ_M^2 due to small angle scattering.*

However, due to the combination of a low scattering signal and excessive cross-talk between the pixels, the above method struggled to reliably retrieve the desired contrasts, especially the scattering signal. To solve this problem, a new retrieval method, developed by Maughan Jones [152], was used, which takes into account the fact that neighbouring pixels are not independent from one another. This method involved fitting three overlapping Gaussian distributions,

separated by the sample mask period, to three horizontally adjacent pixels, as shown in Fig. 3-8.

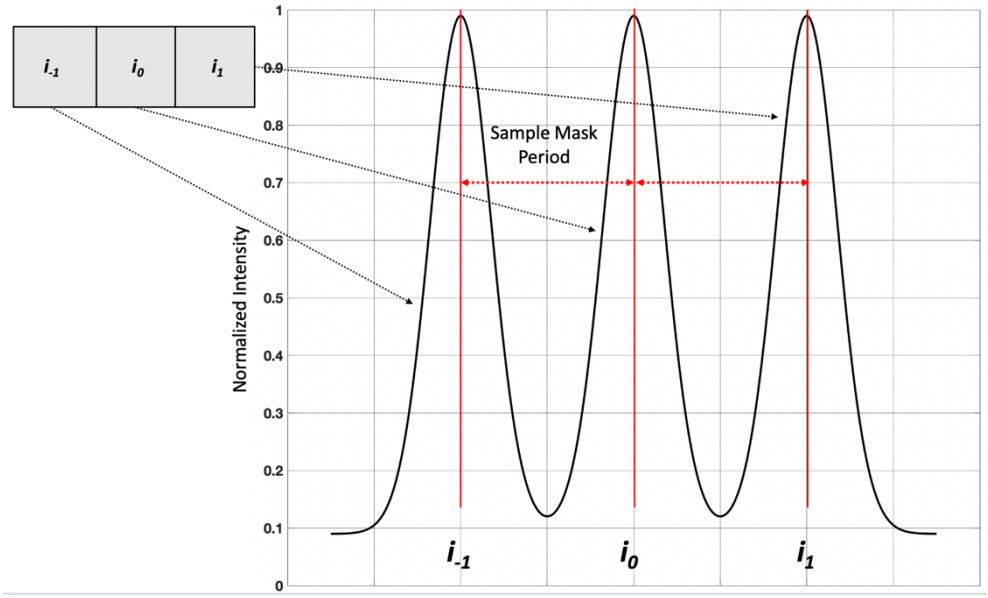

Figure 3-8 *Sum of three Gaussians for three adjacent pixels used for the phase retrieval, separated by the sample mask period. Only the parameters of the central Gaussian, corresponding to the central pixel, were used for the retrieval of the absorption, differential phase and dark field images.*

Here too, the three parameters of the Gaussians (area, position of the maximum and variance of the curve) were extracted from the Gaussians fitted to the illumination curve, and to the measured intensity from the sample for three adjacent pixels. However, only the coefficients of the central Gaussian (*i=0*), which corresponds to the central pixel, were used for the retrieved images. By applying this principle in a “rolling” fashion, every pixel can be individually retrieved while discarding the negative influence of its two nearest neighbours [152].

3.5 Additional Imaging methods

The main aim of this project was the comparison of the EI XPCi system with ultrasonic imaging for the detection and identification of defects in fibre-reinforced composite plates. Other imaging techniques were

used in this project, either for the confirmation of the observation made using EI, or to enhance the capabilities of EI XPCi compared to other conventional imaging techniques. High-resolution conventional X-ray CT imaging was used for the severely damaged composite plate (Chapter 4), and contrast agent enhanced planar X-ray imaging was used for the second damaged composite plate (Chapter 5). Each of the additional imaging methods are described in the respective chapters.

3.6 Image Processing Techniques

In the planar image acquisitions described in Chapter 5 and 6, several image artefacts were observed due to the long acquisition times performed for these CFRP samples, which required different acquisitions parameters compared to other samples. These artefacts were due to movements of the system components, including both the source and the sample mask. As a result, post-acquisition image processing tools were developed to correct those image artefacts and remove them from the images without affecting the qualitative and quantitative quality of the images.

3.6.1 Mask lines Correction

The sample and detector masks are manufactured by electroplating (absorbing) gold onto a (transmitting) graphite substrate, resulting in a periodic array of gold and graphite columns. This splits the X-ray beam into an array of thin vertical beamlets going through the graphite. In order to provide stability to the structure, the vertical apertures in the gold layer have periodic interruptions (gold horizontal “bridges”). From the retrieved images acquired in Chapter 5, a mask lines artefact, due to the gold bridges in the masks apertures, was observed throughout all images, which was caused by a vertical source movement during the acquisition [153].

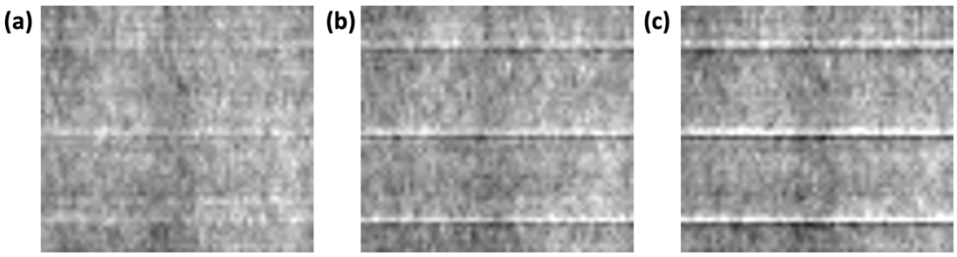

Figure 3-9 *Region of interest (ROI) of undamaged area of CFRP sample from the dithering steps 1 (a), 8 (b) and 16 (c) of the attenuation channel, showing the appearance of the mask lines artefact with scanning time.*

This movement projected the horizontal bridges onto slightly different vertical positions at the detector over time, resulting in the appearance of the horizontal lines which, in the absence of movement, would be removed by the flat field correction. The scanning time for each of the acquisition was about an hour, and the mask lines became more prominent as the scan progressed. Fig. 3-9, which separately shows subsequent dithering steps, shows how artefacts related to the masks' horizontal lines appear as the step number increases.

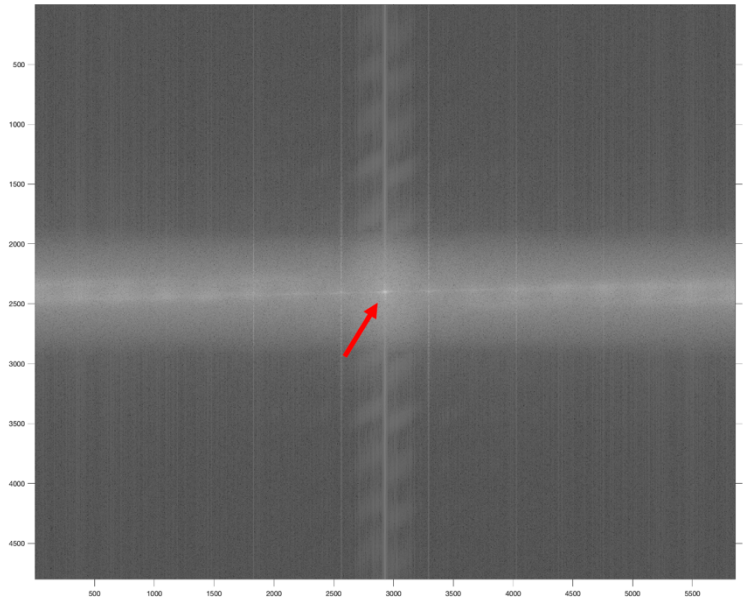

Figure 3-10 *2D Fourier Transform of the 0˚ attenuation channel, with the main spike corresponding to the mask lines artefact highlighted by red arrow.*

To remove these artefacts, a Fourier approach was used. The bright vertical point in the middle of the 2D Fourier Transform of the image

(Fig. 3-10) corresponds to the high frequency signal from the mask lines artefact. This spike was thresholded and removed.

Once this spike was removed, the inverse Fourier Transform was applied to obtain the final images. The resulting images with reduced mask lines artefacts are shown in Fig. 3-11. The images were then combined to include both the 0˚ and 90˚ orientations in a single image, as described in Chapter 5.3.2.

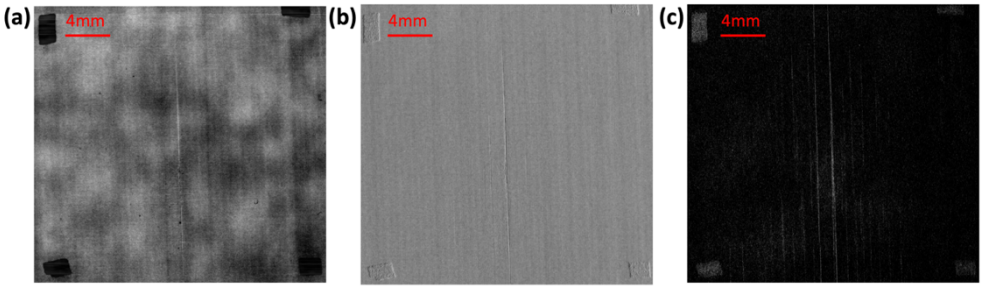

Figure 3-11 *Attenuation (a), differential phase (b) and dark field (c) channels of the 0˚ orientation scan of the CFRP sample from Chapter 5, with the mask lines artefact removed, without affecting the sample; axial splitting cracks observed.*

3.7 Gradient Correction

A common problem encountered in the EI XPCi imaging system is the misalignment of the apertured masks. The robustness of the EI XPCi system against potential misalignments has been tested and it was shown that a misalignment within a 1˚ range across all three angular degrees of freedom, as well as up to 1 μm translation do not affect the quality of the image [154]. After the acquisitions of the porosity specimens in Chapter 6, a gradient was observed across the full differential phase images, as well as a distinct change in intensity across the dithering steps, as shown in Fig. 3-12.

This gradient was associated with the movement of the masks (more specifically, the sample mask) during the acquisition, which was longer than a standard planar acquisition due to the high statistics required (1 hour vs. a few minutes for a standard planar image). This movement

led to a substantial variation in intensity (as shown in Fig. 3-12) between dithering steps. To resolve this issue, the movement of the masks was tracked using the images of the individual dithering steps. In each image, the average signal in different areas was used to estimate the relative mask movement and correct for it.

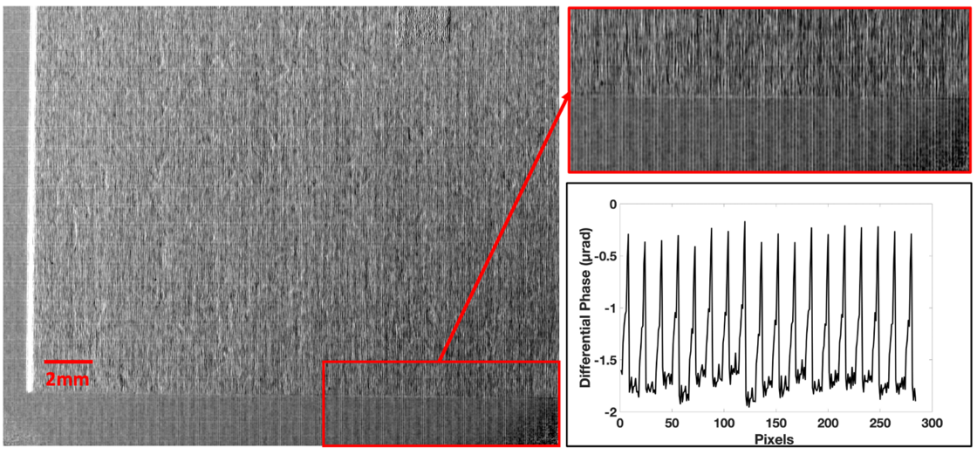

Figure 3-12 *Dithering artefact observed throughout the porosity samples images, where a periodic variation in the intensity (in μrad) across the dithering steps can be observed.*

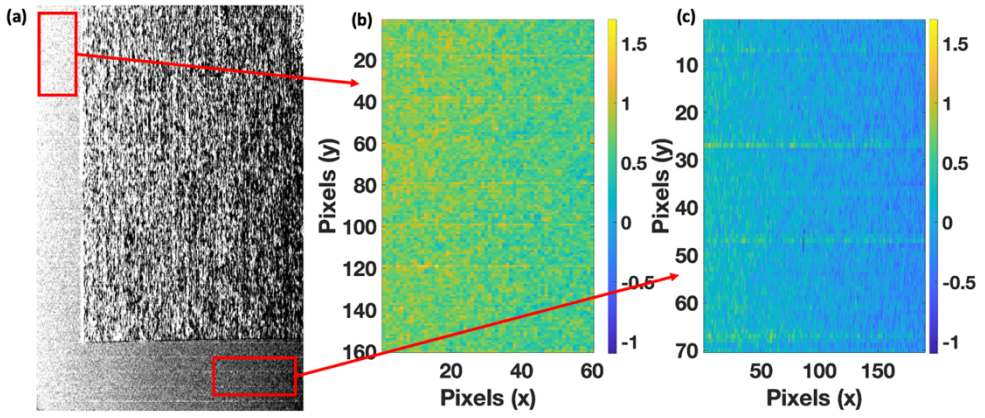

Figure 3-13 *Variation in intensity (in μrad) observed across a single dithering step (a), both in the top left corner (b) and bottom right corner (c), showing a gradient across both the x- and y-directions.*

As can be observed from Fig. 3-13, a clear variation in background intensity could be observed. A first gradient in the x-direction can be observed in both Fig. 3-13(b) and (c), indicating a slight rotation of the mask around the y-axis. A second gradient can be observed in the y-

direction, by comparing the average intensity in Fig. 3-13(b) and (c), showing a clear decrease, indicating a rotation of the mask around the x-axis [155]. To correct for this gradient, a correction map was created by fitting a polynomial to the background signal of each individual dithering step. The background in the image was thresholded by plotting the standard deviation of the differential phase image: The standard deviation was calculated over an area of 7x7 pixels, on a pixel-by-pixel basis, as shown in Fig. 3-14(a). This was done as the standard deviation of the background was substantially lower than the sample's, hence simplifying the thresholding task. The resulting threshold image is shown in Fig. 3-14(b).

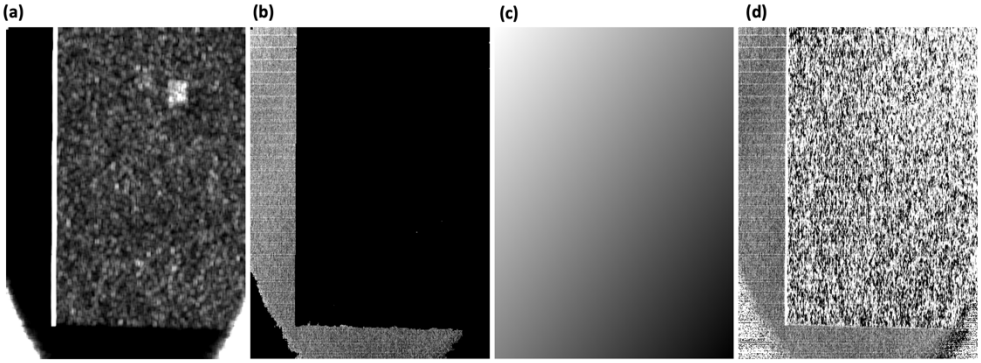

Figure 3-14 *Standard deviation of the differential phase for a single dithering step image, calculated on a pixel-by-pixel basis (a) over area of 7x7 pixels, used to threshold background (b); correction map (c) created using background and new, gradient free dithering step (d).*

An investigation was carried by Doherty et al. [155] to quantitatively determine the variation in the illumination when one mask is misaligned relative to the other in a given degree of freedom. This investigation was used to determine the degrees of freedom involved in the misalignment during the acquisitions of the planar sample images, and as a result determine the order of the polynomial needed for gradient correction. The polynomial fitted to the background of the differential phase image was two dimensional (to correct in both the x- and y-direction) and had the form:

$$P(x, y) = axy + bx + cy + d \tag{3-12}$$

where *a*, *b*, *c* and *d* are integers. The correction maps were then subtracted from their corresponding images, with the resulting corrected image in Fig. 3-14(d). This was repeated for images acquired at all dithering steps. The dithering steps were then recombined to form the higher resolution differential phase image. A comparison showing the differential phase signal before and after the gradient correction is shown in Fig. 3-15.

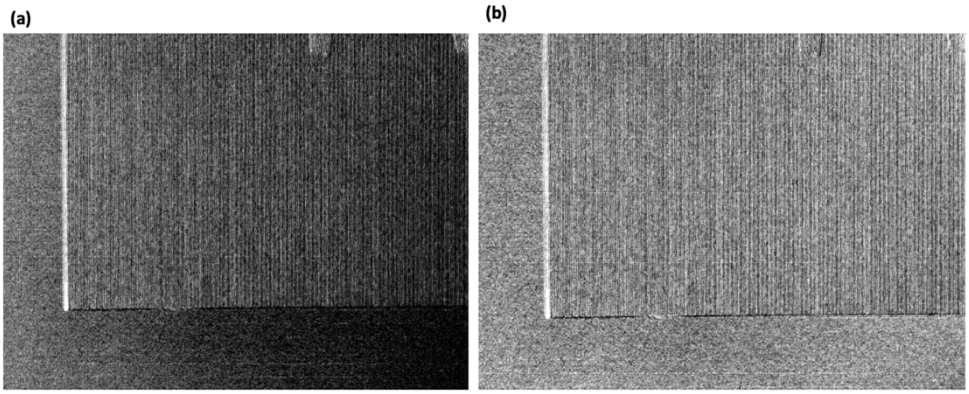

Figure 3-15 *refraction image of recombined dithering steps before (a) and after (b) gradient correction.*

The contrast was stretched in order to enhance the change in the background from one image to another. A clear improvement can be observed after the implementation of the gradient correction. The background of the gradient corrected image is uniform across the image, averaging 0, without the correction affecting the features of the sample.

3.8 Conclusions

This chapter presented the two main imaging methods used for the detection and identification of defects in fibre-reinforced composite plates, ultrasonic immersion C-scan imaging and phase contrast X-ray imaging, as well as two new post-acquisition image processing tools developed to remove imaging artefacts from source and sample mask

movements. The results and specific details of the experiments are described in Chapters 4 to 6. In Chapter 4 the double through transmission ultrasonic immersion C-scan imaging of a severely damaged composite plate is compared to the Edge illumination system, both for planar imaging and CT, to benchmark EI XPCi as a viable NDE method. The comparison and conclusions from the two imaging systems are then further confirmed by the acquisition of a high-resolution conventional CT scan of the composite sample. In Chapter 5, the EI XPCi system, and more specifically the differential phase and dark field signal channels are compared to contrast agent-enhanced radiography, reinforced by ultrasonic double through transmission immersion C-scan imaging. Lastly, in Chapter 6, the porosity specimens are quantitatively studied and a possible correlation between phase-based signal and ultrasonic attenuation is investigated, obtained using single through transmission ultrasonic immersion C-scans.

4 Benchmarking EI XPCi as an NDE Technique for Damage Detection in Composite Plates by Comparison with Ultrasonic Imaging

4.1 Introduction

This chapter presents a comparison between EI XPCi planar and CT imaging, and ultrasonic immersion C-scan imaging for an investigation of the type, extent, and location of impact damage in a small composite plate sample in which damage was clearly visible as an indent of approximately 4mm diameter and a protrusion of 5.5 mm diameter at the back. The aim of this chapter was to benchmark EI XPCi as a viable NDE method. In the first part of this chapter, a full investigation of the sample using ultrasonic imaging is presented, with both B- and C-scans of the samples at different areas of the sample shown. The second part of this chapter presents an initial investigation of the sample using planar EI XPCi, imaging the sample in different orientations. In the third part of this chapter, a full comparison between the ultrasonic B-scans and the EI XPCi CT images is performed for three different areas of the sample, including an undamaged area, delamination, and a severely damaged area. The last part of this chapter presents a high-resolution, conventional X-ray CT scan of the sample to confirm the observations made from the differential phase and dark field images of this sample. The main results presented in this chapter are included in a first author paper published in the journal Composites Part B, “Enhanced Composite Plate Impact Damage Characterisation using X-Ray Refraction and Scattering Contrast Combined with Ultrasonic Imaging” [156].

4.2 Specimen

A 2 mm thick, 19*19 mm^2 carbon fibre/epoxy resin cross-ply laminate sample containing severe impact damage was provided by Nikon, shown in Fig. 4-1. The 16 plies were each measured to be

approximately 125 μm thick (See section 4.5.1), and the top and bottom laminae were observed to have a woven structure. The sample contained an indent induced by impact, approximately 4 mm in diameter and 1.2 mm in depth, which resulted in a small protrusion on the back of the plate, approximately 5.5 mm in diameter and 0.5 mm deep.

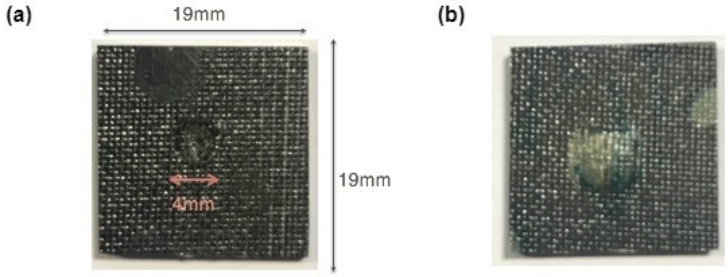

Figure 4-1 *Photograph of specimen: (a) impact damage on front surface; (b) protrusion on back surface.*

No further information about the manufacturing of the sample was provided, nor any details about how the defect at the centre of the sample was caused. As a result, the number of plies, lay-up and stacking sequence, as well as the impact mechanism and energy were not known. While it is customary to choose samples with BVID for benchmarking of a new NDE technique, here a sample with severe impact damage was chosen as it ensured the presence of different types of damage across multiple scales, thus enabling to test the capability of EI XPCi over a wide range of damage sizes and degrees of severity.

4.3 Experimental Methods

The composite sample was imaged using ultrasonic immersion C-scan imaging, EI XPCi, with both planar imaging and CT imaging for a full investigation of the damage. High resolution X-ray CT imaging was also performed.

4.3.1 Ultrasonic Imaging

Ultrasonic immersion C-scan imaging was performed on the specimen, using the setup described in Chapter 3.3.1. This was done using three different transducers: a ½ inch (13 mm) diameter, unfocussed 10MHz transducer, and two ¼ inch (6 mm) diameter, focused longitudinal transducers, with frequencies of 20MHz and 30MHz. The frequencies were chosen for this sample by taking into consideration the ultrasonic wavelength, which should be short enough to allow ply layer separation, signal attenuation that increases with frequency, and the achievable lateral resolution, determined by the transducer beam diameter. The focussed transducers were positioned at the focal length of ¾ inch (19 mm) above the surface of the sample. The transducers focal spot diameters were calculated to be 650 µm and 400 µm in water, and wavelengths of 140 µm and 90 µm, respectively, using an estimated velocity in the composite sample of 2800 m/s (calculated using the thickness of the sample and Equation 3-1). The wavelength of the 10MHz transducer was calculated to be 280 µm. However, the 10MHz unfocussed transducer, with a nominal diameter of 19 mm (½ inch), was not sensitive enough to obtain an accurate representation of the sample, or the damage within it. As a result, only the scans obtained from the focussed transducers were analysed further. Initial scans were taken with different step sizes to investigate which step size would provide enough information. The step size was chosen as 200 µm, which was the smallest step size allowed by the system used and corresponds to half of the focal spot diameter of the 30MHz transducer. The A-scan acquisition was done over an area of 130*130 steps, resulting in an area of 680 mm^2, to contain the full sample, with a sampling rate of 100MHz. The scanning time was about 8 hours on a laboratory system. The A-scans were used to generate both B- and C-scans for comparison with EI XPCi CT slices.

4.3.2 EI XPCi

The experimental setup described in Chapter 3.4.1 was used to acquire EI XPCi CT images of the sample. The detector used was a Hamamatsu C9732DK flat panel CMOS detector with a 50 x 50 μm^2 pixel size. Due to cross-talk between neighbouring detector pixels caused by the diffusion in the scintillator, the effective resolution of the detector was approximately 100 μm [157]. EI XPCi was implemented using a set non-skipped masks: The sample mask had an aperture of 12 μm and a period of 38 μm, and the detector mask had a 20 μm aperture and a 48 μm period [158]. For the planar images acquisition, 19 points along the illumination curve were taken, with 9 points taken symmetrically on each side with respect to the centre position (i.e. where the sample and detector masks are perfectly aligned and the detected intensity is maximised). The sample mask was translated by 2 μm along the x-direction between each point, with an exposure time of 1.2s, the longest time achievable without saturating the detector. The sample was mounted on a stage which could be moved along the x-axis. The sample data acquisition was carried out by taking 19 projections with the sample mask placed at the same relative positions as done for the illumination curve. In order to increase the resolution, the sample was also dithered, i.e., repositioned at different sub-pixel locations, for each sample mask position. The dithered images were then recombined in a single image with a higher resolution. The sample was dithered 10 times for each mask position, moving by 4 μm along the x-direction for each dithering step, calculated using Equation 3-5. Both the surface and the thickness of the sample were imaged using 2D planar XPCi imaging. As the system is only sensitive to refraction of the beam in the x-direction, two sets of images were acquired, in both the 0˚ and 90˚ orientations, to obtain sensitivity along the two main axes for two sets of sample orientations (i.e. for the face on and through thickness scans).

The CT images were taken using the same experimental setup described above, using the non-skipped sample and detector masks.

Five sample mask positions were used to obtain the illumination curve, with a 6 μm translation along the x-direction, and no dithering was applied. For each sample mask position, 1800 projections were taken, with a sample rotation of 0.2° per projection. Each projection had a 1.2s exposure time, resulting in an overall acquisition time of 12 hours (3 hours live scanning time) due to overheads in the non-optimised system. The image acquisition procedure required acquiring a flat field for every sample position, thus the sample was removed from the field of view after every projection acquired. This was done to account for any possible movement of the system during the acquisition, which lasted for almost a day. The voxel size was 41*41*41μm^3.

Phase retrieval was carried out on the both the planar and CT image sequences using the three Gaussians method described in Chapter 3.4.2 to obtain the attenuation, differential phase, and dark field projection images. The CT retrieved channels were then reconstructed using a CT reconstruction algorithm provided by Nikon, which was a Feldkamp-type reconstruction. The reconstructed CT images were then segmented and visualised using Drishti, a volume exploration and presentation tool [159].

4.3.3 X-Ray CT imaging

An additional high-resolution X-ray scan of the sample was performed using a commercial X-ray system (Nikon XTEK XTH 225kV). The scan was performed using 40 kV beam energy and 358 μA beam current. A PerkinElmer 1620 flat panel detector was used, with 200 μm pixel size. The system had a geometric magnification of 14 resulting in an effective pixel size of 14 μm. The exposure time per projection was 1 s, and a total of 3185 projections were acquired, resulting in a scanning time of approximately 1 hour. The experimental setup for this system is described in [160].

4.4 Ultrasonic Imaging

The composite sample was scanned using the ultrasonic immersion C-scan imaging described in Chapter 3.3.1 and 4.3.1, using a variety of frequencies. Multiple frequencies were used to optimise the damage assessment in the sample for a comparison with EI XPCi.

4.4.1 C-scan Ultrasonic Imaging

The Nikon sample was initially imaged using 20 MHz and 30 MHz focussed transducers to obtain double through-transmission C-scans, with a 200μm step size. Double through-transmission scans are used to detect severe damage, nominally delaminations, within the sample, clearly visible as areas with little or no signal. However, they give no indication as to what depth within the composite plate the damage is located. Unfortunately, the 30 MHz focussed transducer suffered from high attenuation, and a double-through transmission signal was not observable. Therefore, only one double-through transmission C-scan with high sensitivity was obtained from the 20MHz focussed scan, as shown in Fig. 4-2.

The overall damage detected was much larger than the indent visible on the surface of the sample, with dimensions of 8.2*7.8 mm^2. The low signal observed on either side of the sample are due to attenuation from the sample holders, which were placed between the sample and the stainless-steel plate (See Fig 3-1). The high signal at the bottom of the scan is due to the smooth area on the surface of the sample, which is thought the be where the sample was held when the damage was incurred (Fig.4-2). As the depth and thickness of the delamination could not be obtained from the double through-transmission C-scan alone, a further investigation of its location within the sample was needed. The sample was scanned twice, alternating for the front and the back surface facing the transducer, using the 20 MHz and 30 MHz focussed transducers. The surface scans for both orientations and frequencies are shown in Fig. 4-3.

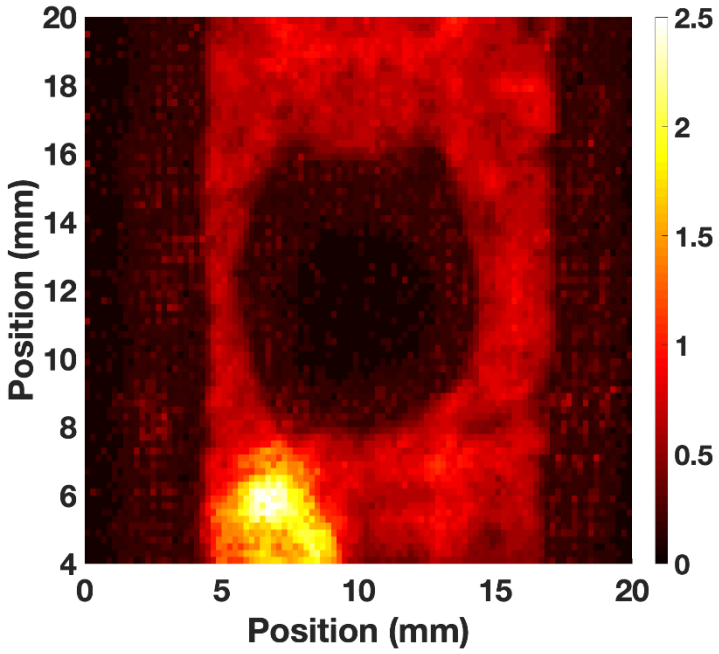

Figure 4-2 *Double through-transmission C-scan of the sample using the 20MHz focussed transducers with a 200μm step size, showing the overall damage detected within the sample, including a delamination, covering an area of approximately 8.2*7.8mm^2.*

The C-scans were obtained from the peak reflections from the sample surface closest to the transducer. Only the damage on the surface is visible, and no indication of any internal damage can be obtained from these scans. The measurement carried out with the 30 MHz focussed transducer gave similar results to the 20 MHz C-scans, as can be seen in Fig. 4-3(c) and (d). The front surface scans look very similar, with the smooth surface in the bottom left corner showing up more clearly in the 30MHz than in the 20 MHz scan. The indent at the centre of the plate is visible in both scans, and the woven structure of the surface ply can be observed in both scans. The back-surface scans effectively look the same at 20 MHz and 30 MHz. Here too, the woven structure of the ply is observed in both frequencies, with the 30 MHz scan showing a slightly better reflection around the protrusion area. However, it can be observed that the reflections of the 20 MHz scans are of a higher amplitude to the 30 MHz scans. The best suited transducer to be used on this sample was thus determined to be the

20 MHz focussed transducer. It was found to offer a better resolution than the 10 MHz transducer thus allowing a better assessment of the damage. The 30 MHz focussed transducer was found to be too attenuated, resulting in a lack of a double through transmission signal, without offering a more accurate visualisation of the damage than the 20 MHz focussed transducer. As a result, all the images obtained by EI XPCi and the high-resolution X-ray CT imaging shown later on were compared with scans from the 20 MHz scans.

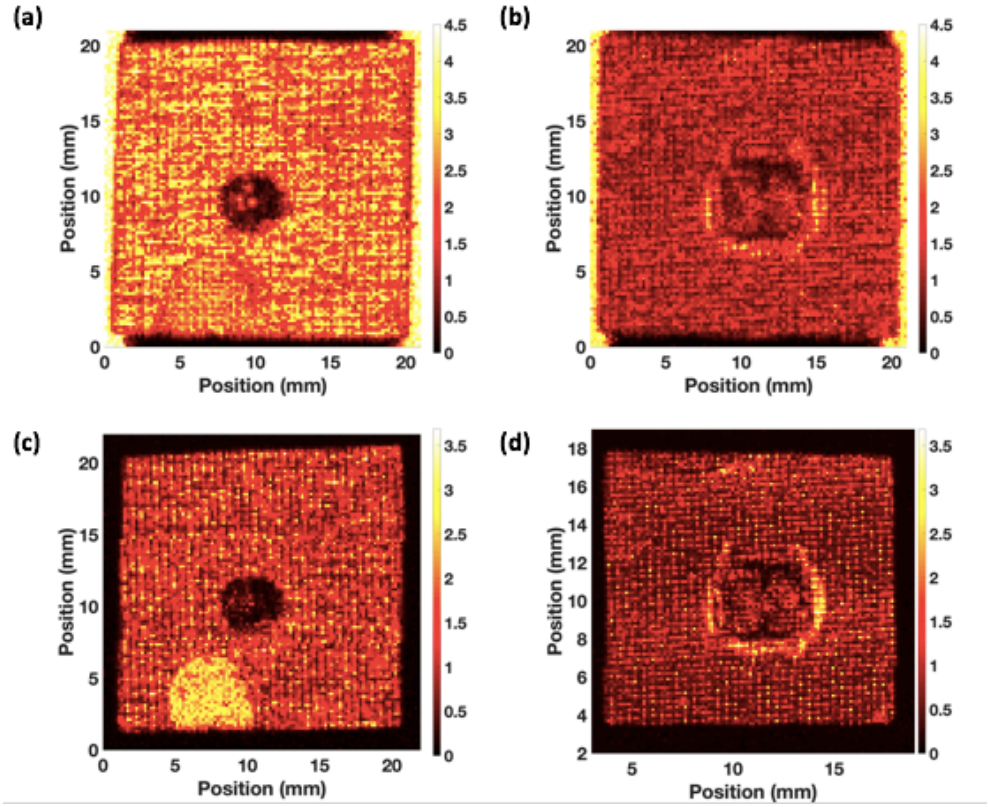

Figure 4-3 *Front (a) and back (b) C-scan of the sample using 20MHz focussed transducers; front (c) and back (d) C-scan of the sample using 30MHz focussed transducers with 200μm step size, showing the front surface indent as well as the back surface protrusion.*

Further C-scans were produced by time-gating the A-scans around areas of interest, mainly the lower-surface C-scan, showing the peak from the surface furthest from the transducer, and the sub-surface C-scan, showing the maximum amplitude peak from the inner reflections of the sample, as shown in Fig. 4-4. For the sub-surface C-scan, the

positive maximum amplitude is plotted, whereas for lower surface scans, the negative minimum is plotted, due to the difference in acoustic impedance (See Chapter 3.3.1). The sub-surface and lower-surface scans from both the front and back scans for the 20MHz transducer are shown in Fig 4-5.

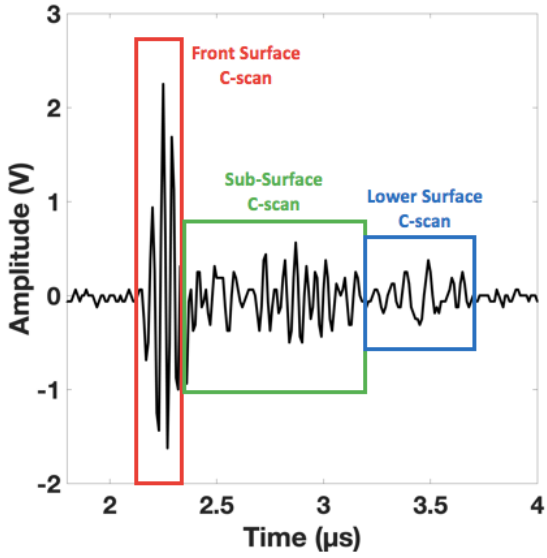

Figure 4-4 *Time-gating of the sample reflection to obtain the front surface C-scan (red), sub-surface C-scan (green) and back surface c-scan (blue).*

From the sub-surface scans from both sides (Fig. 4-5(a) and (c)), the damage from the indent is clearly visible, extending over an area of 4.7x4.0 mm^2 for the front surface scan and 6.1x5.5 mm^2 for the back-surface scan. In both scans, the cross-ply structure of the sample is visible. High reflections can be observed around the indent and protrusion, indicating the presence of damage around the impact area. In the lower surface scans (Fig. 4-5(b) and (d)) the extent of the damage is more similar, extending over an area of 8.2x7.3 mm^2. In the lower surface C-scan from the front surface scan (Fig. 4-5(b)), the damaged area at the centre is observed to have almost no signal, due to damage observed in the sub-surface C-scan, with dimensions 5.8*5.4 mm^2, surrounded by a ring of strong reflections, indicating further damage present close to the lower surface of the sample. Such strong reflections could indicate the presence of a ring-shaped defect

around the indent close to the lower surface of the sample. This was not observed in the back-surface scan (Fig. 4-5(d)), where the lower surface C-scan corresponds to the side with the indent, and the entirety of the damage was already shown by the sub-surface C-scan. However, the overall damage in the plate has the same shape in both lower-surface scans, and is observed to be almost circular in both scans, with two extensions visible in the top area, and a small extension in the bottom left part of the damage. The lower-surface C-scan looks very similar to the double through transmission scan shown in Fig. 4-2, which is expected, as the signal in this scan has been all the way through the plate and back. This was further investigated by plotting the B-scans of the sample across the damaged area of the sample, showing the ring-shaped damage.

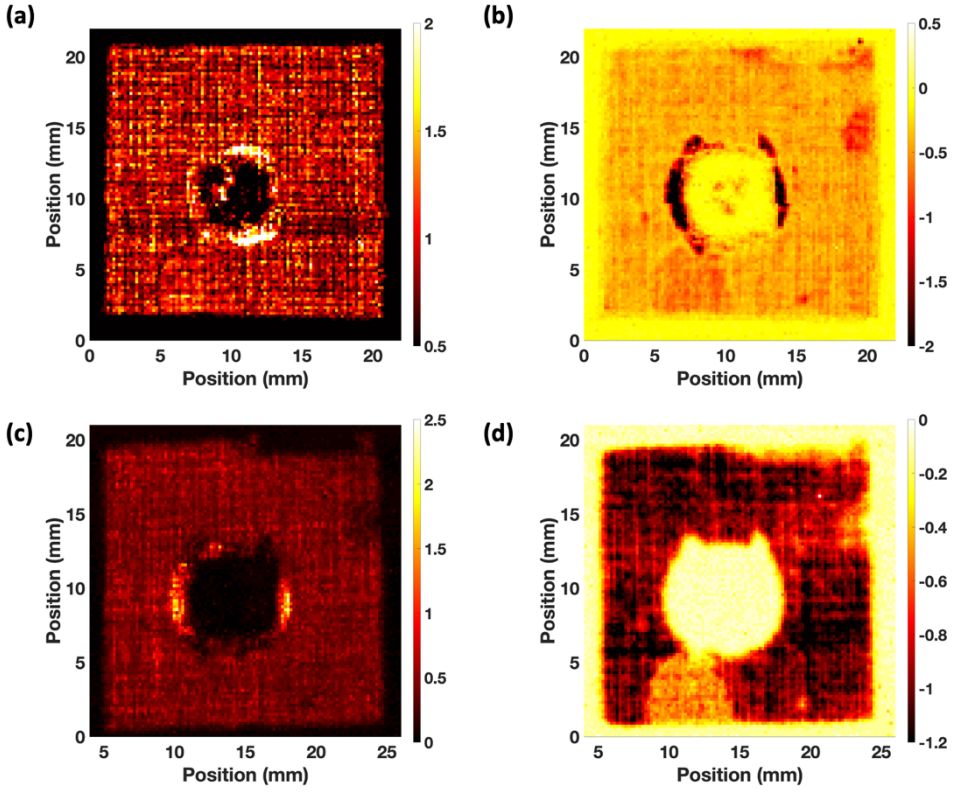

Figure 4-5 *Sub-surface (a) and lower-surface (b) C-scan of the sample using front surface scan; sub-surface (c) and lower-surface (d) C-scan from the back surface scan for the 20MHz focussed transducer with 200μm step size, showing the internal damage detected at different depths, for both front and back surface scans.*

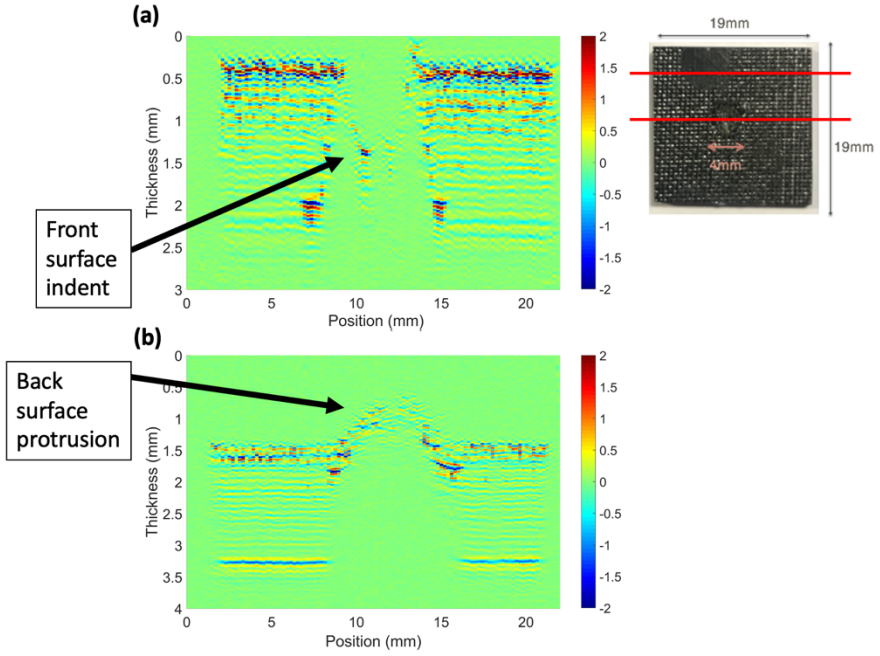

Figure 4-6 *B-scans of the Nikon sample for 20MHz focussed transducer with 200μm step size at 8.6mm from top of sample (a) from front surface scan and (b) from the back surface scan showing both front surface indent and back surface protrusion.*

The damage is clearly visible in B-scans (Fig. 4-6(a)), where the indent and surrounding damage can be seen. As expected, no signal was reflected from the sample beyond the damage, and the lower surface of the sample in that area was not visible. Strong reflections can be observed from the edges of the damage closer to the lower surface in Fig. 4-6(a), indicating the possible presence of a delamination in that area observed earlier in Fig. 4-5(b). The damage at the back surface of the sample is clearly visible in Fig. 4-6(b) with, also in this case, a complete lack of signal from the area beyond the damage. Here too, stronger reflections are observed on either side of the protrusion closer to the surface, matching the assumed delamination in that area observed in Fig. 4-5(b).

4.5 Planar EI XPCi

The damaged sample was imaged using planar EI XPCi for an initial assessment of the damage extent observable. This was compared with the known features observed from the ultrasonic imaging. The

attenuation, differential phase and dark field signals were retrieved. Images were acquired both through the surface and through the thickness of the sample, and due to the 1D sensitivity of the system, the sample was imaged twice for each orientation, rotated 90° clockwise in the x-y plane (i.e., in the plane normal to the X-ray beam, see Fig 2-6) to achieve sensitivity along the two main axes, as shown in Fig. 4-7.

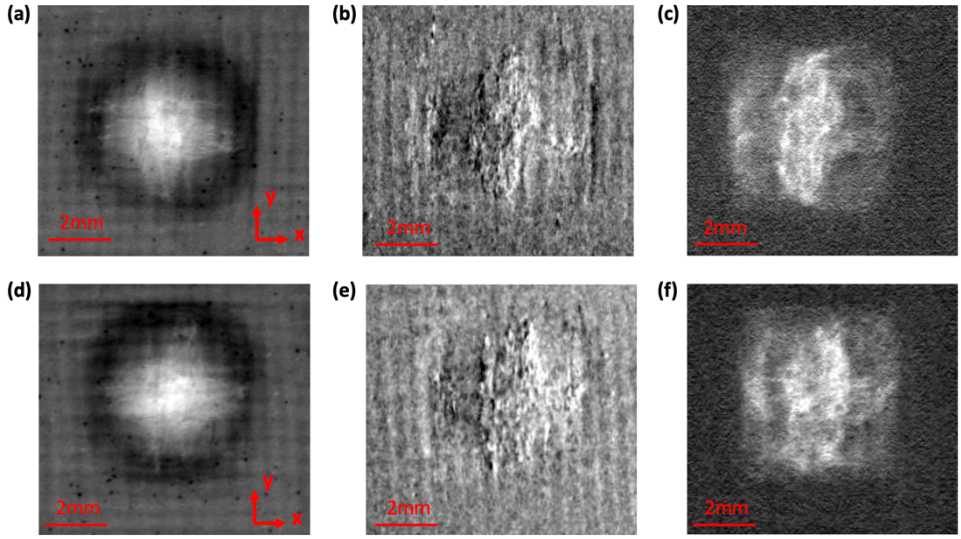

Figure 4-7 *Planar images of the surface of the sample for the 0° (top) and 90° clockwise rotation (bottom); Retrieved attenuation (a, d), differential phase (b, e) and dark field (c, f) images.*

The impact has a round outline in the attenuation images, which is comparable to the shape observed in the double through transmission ultrasonic C-scan (Fig. 4-2). It shows the material displacement due to the impact damage, with the bright signal in the middle of the impact corresponding to an area with less material, and the dark ring around it corresponding to a denser area. However, especially the dark field images show a square outline of the damage area, different to the circular shape visible in the ultrasonic C-scan (shown in fig 4-5 with larger damaged area detected). This shape of the damage is expected due to the cross-ply nature of the sample and the directionality of the signal's sensitivity. As the phase-base signals are only sensitive to

vertical features and the sample was rotated in the 90˚ scan, different features are observed in the two scans. In the differential phase image from the 0° sample orientation (Fig. 4-7(b)), a very strong vertical feature can be observed on the right-hand side of the damage. This was later identified as a delamination using the EI XPCi CT images (see Chapter 4.6.2). This feature was not observed in the 90˚ scan as it was no longer oriented along the direction of maximum sensitivity. Vertical features are observed all around the main damage area, which could be due to damaged fibre bundles of the cross-ply structures. The cross-ply structure is visible in the attenuation image, with only the vertical fibre structure visible in the differential phase images due to the 1D sensitivity. In the dark field images, the square shape of the damage is more pronounced than in the differential phase images, with clear outline of the extent of the damage shape and larger extent than observed in the differential phase and attenuation signals. In both sample orientations, the dark field signal shows a strong vertical stripe in the main damage area, which is also observed in the differential phase images, indicating that some sub-pixel scale features accompany the main damage, and that the damage extends further than expected. Such damage could be due to fibre damage or micro-cracks present in the matrix, as well as the extension of the damage observed in the differential phase into a much smaller scale.

Profile plots were taken across the planar images of the sample to assess the damage extent across the damaged area of the sample. The extent of the damage was measured to be approximately 5.9*5.4 mm^2, 5.9*5.7 mm^2 and 6.6*7.3 mm^2 for the attenuation, differential phase and dark field signals, respectively. As expected, the dark field signal indicated a larger damage extent than the attenuation and differential phase signals, due to its sensitivity to sub-pixel features. The extent of the damage measured in the dark field signal is still smaller than the dimensions of the damage measured in the double-through transmission C-scan of the sample (8.2*7.8mm^2, see chapter 4.4.1). This is due to the double through transmission C-scans being

sensitive to delamination, which is harder to detect using planar EI XPCi. The sample was also imaged through its thickness, in order to be sensitive to the fibre orientation in the cross-ply plate, as can be seen in Fig. 4-8.

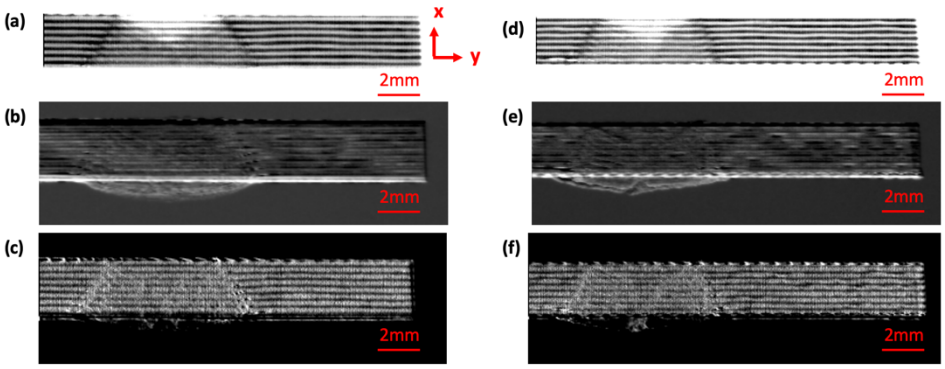

Figure 4-8 *Planar images of the thickness of the sample for the 0° (left) and 90° clockwise rotation (right); Retrieved attenuation (a, d), differential phase (b, e) and dark field (c, f) images.*

In the images acquired through the thickness, the different plies can be clearly seen, with both the attenuation and dark field images showing different intensities for the alternating plies. This effect should not be observable in the attenuation images, as there is no difference in the thickness or attenuation coefficients between the individual plies, with the only difference being fibre orientation. This was later attributed to a bleeding of the dark field signal into the retrieved attenuation image (See Chapter 5.3.3). These were used to confirm the number of plies in this sample as the individual plies are well defined and can be separated (unlike the ultrasonic B-scans in Chapter 4.4.2). The protrusion at the back of the sample was initially visible in the attenuation and dark field images, however the contrast stretching applied in order to be able to see the individual plies rendered the protrusion invisible. However, some damage is visible within the protrusion in the dark field images. The dark field and differential phase images also show the individual plies: In the differential phase images, the interface created by adjacent plies leads

to a strong signal. In the dark field images, the plies are defined by variations in contrast depending on the orientation of the plies, with plies in bright signal corresponding to the fibres parallel to the X-ray beam (i.e. the fibres scatter laterally, increasing the signal), and dark plies corresponding to plies where the fibres are orthogonal to the beam (i.e. the fibres scatter up and/or down, not affecting the signal). The damage in the sample is clearly visible in all three channels, and it can be observed that the damage propagated in a cone shape from the point of impact through the thickness of the sample. The indent can be seen in the attenuation images as the intensity of the sample there is brighter due to the displaced material from the impact. The propagation of the damage is less visible in the differential phase images, however the displacement of the plies in the damaged area can still be observed. It should be noted, however, that the XPCi system used was a low-resolution system which can be improved by using a skipped mask and/or a higher resolution detector. This was done for the samples in chapter 5 and 6, where “skipped” masks were used for improved resolution.

4.6 CT EI XPCi and comparison with Ultrasonic Immersion Imaging

To obtain a better understanding of the damage in the plate in addition to the ultrasonic imaging and the planar EI XPCi, an EI XPCi CT scan was performed on the sample. The results obtained from the ultrasonic C-scans and EI XPCi CT scans are presented as 2D slices taken from different cross-sections of the sample. For each cross-section, two B-scans are presented with, respectively, the front and back surface of the sample facing the transducer, with the front surface containing the indent, and the back surface the protrusion. Three retrieved signals (attenuation, differential phase and dark field) are shown for the matching CT slices. An additional qualitative comparison between the three image sequences retrieved from the sample’s CT scans was carried out by merging them as an RGB image, with the attenuation

images represented by the blue channel, the differential phase images represented by the green channel, and the dark field images represented by the red channel. 3D renderings of the CT datasets are also shown for a complete representation of the areas of interest. Three sets of figures are shown, one from an undamaged area of the sample, one showing a delamination across the sample, and one from the most severely damaged part of the sample.

4.6.1 Undamaged Area

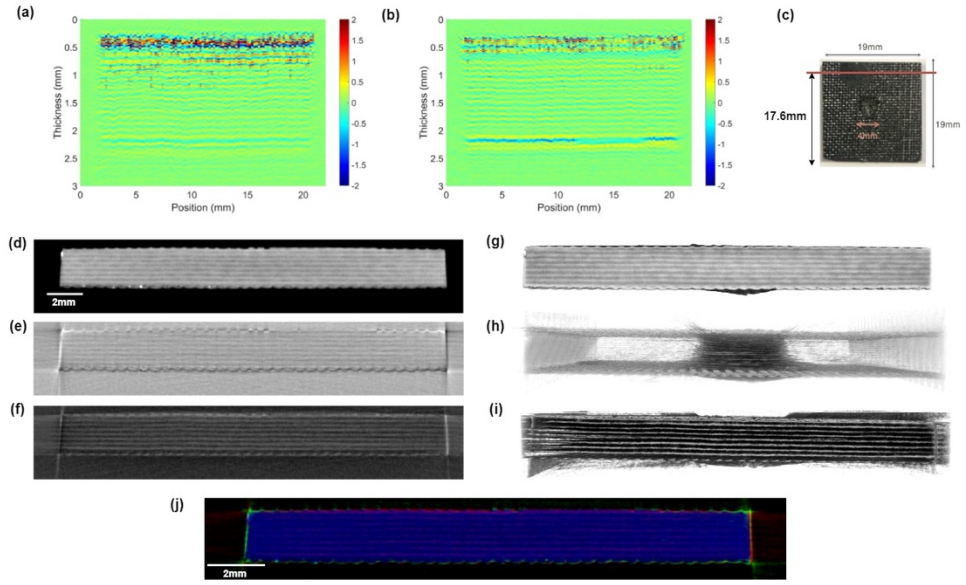

Figure 4-9 *Undamaged area of sample: ultrasonic B-scan with (a) front surface (indent) and (b) back surface (protrusion) facing the transducer (colour scale signal voltage in volts); (c) position of B-scans and cross sections within the sample; 2D cross-section of retrieved X-ray (d) attenuation, (e) differential phase, (f) dark field CT reconstructions; 3D rendering of the sample for retrieved (g) attenuation, (h) differential phase, (i) dark field; (j) superposition of the retrieved EI XPCi CT images with attenuation (blue), differential phase (green), dark field (red).*

The images for an undamaged area of the sample taken using immersion ultrasonic C-scan imaging and EI XPCi CT are shown in Fig. 4-9. The ultrasonic B-scans (Fig. 4-9(a) and (b)) and the X-ray images (Fig. 4-9(d) to (f)) show reasonably uniform ply layers. The ultrasonic B-scan images show strong reflection from the surface and back wall, with weaker reflections from the inner plies. Due to surface unevenness, the reflection from the front (impact side, Fig. 4-9(a)) is

larger and more irregular than that from the back surface (Fig. 4-9(b)). The reflections from the inner plies in both B-scans indicate reasonably homogeneous and aligned plies, but potentially with some waviness. The matching X-ray attenuation CT slice (Fig. 4-9(d)) shows contrast due to the cross-ply layup of the sample, with regular plies visible. The contrast can be enhanced (Fig. 4-9(g)) for the uneven sample surfaces to be observed better. Plies are clearly defined, with a signal from the ply interfaces visible in the differential phase image (Fig. 4-9(e)), with the intensity of the intra-ply area matching the background grayscale. This points toward a homogeneous distribution of plies and ply alignment. This homogeneity is more clearly visible in the 3D rendering of the differential phase signal in Fig. 4-9(h), where the contrast was adjusted to highlight the interfaces in the sample, resulting in a strong signal from the surfaces of the sample and a lack of signal from the intraply area within the sample. The only visible signal is due to the impact damage at the centre of the sample, which has only become visible due to the lack of signal from the undamaged area of the sample, as opposed to the inhomogeneities from the ply structure. The dark field images (Fig. 4-9(f) and (i)) show clear signals from the ply layer interfaces, suggesting small, sub-pixel inhomogeneity. Fig. 4-9(e) and (f) show some imaging artefacts in the CT reconstruction at the specimen edges due to the specimen shape. The 3 X-ray retrieved images were superimposed in Fig. 4-9(j) to highlight the complementarity of the signals. For the undamaged part of the sample, the edges are clearly visible, and an indication of the ply layers can be observed from the attenuation (blue) and dark field signal (red).

4.6.2 Delamination

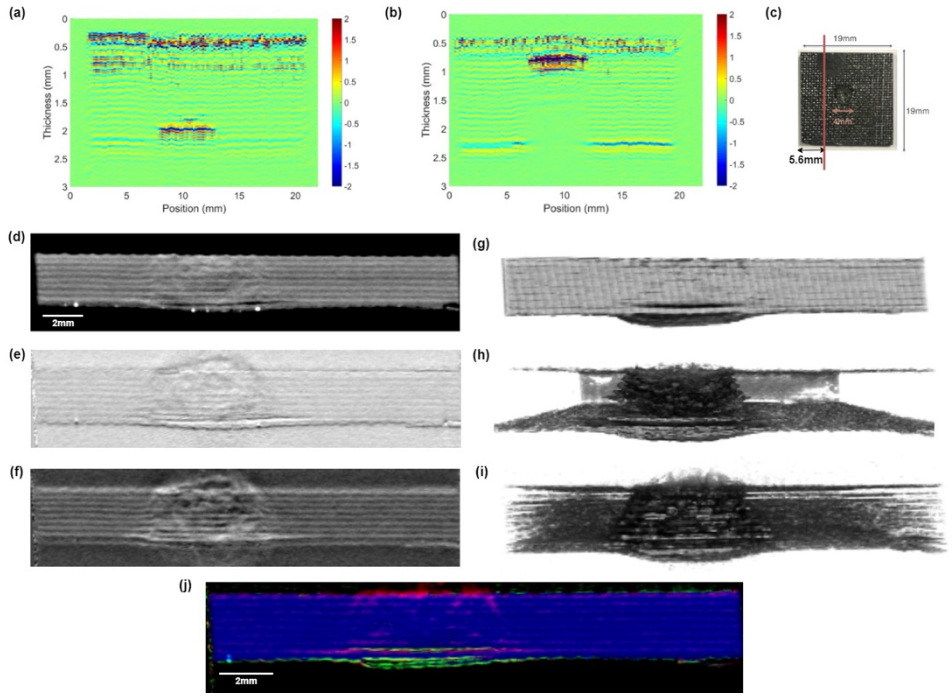

Figure 4-10 *Delamination: ultrasonic B-scan with (a) front surface (indent) and (b) back surface (protrusion) facing the transducer (colour scale signal voltage in volts); (c) position of B-scans and cross sections within the sample; cross-section of retrieved X- ray (d) attenuation, (e) differential phase, (f) dark field CT reconstructions; 3D rendering of the sample for retrieved (g) attenuation, (h) differential phase, (i) dark field; (j) superposition of the retrieved EI XPCi CT images with attenuation (blue), differential phase (green), dark field (red).*

Fig. 4-10 shows a cross-section about 5 mm from the impact centre, where no indent can be observed. Delamination is detected by the ultrasonic B-scan and X-ray images close to the bottom of the sample. The delamination was localized between plies 14 and 15 from the X-ray images, in agreement with the ultrasonic B-scan images, as the first reflection from the delamination in both scans was found to be approximately 0.3 mm from the back surface of the sample, which corresponds to the thickness of the two plies. The delamination was easily detected in the B-scans from the strong reflection observed (Fig. 4-10(a) and (b)), as is characteristic of that type of damage [7]. This was initially not as evident in the X-ray images, until they were overlaid

in Fig 4-10(j). From the X-ray retrievals, the delamination length at that location was measured to be approximately 5 mm in length from the attenuation and differential phase images. This was in good agreement with the measurement of approximately 5.5 mm from the ultrasonic B-scans, considering the system resolution (0.2mm step size).

In the slices and the 3D rendering of the X-ray images, the delamination is visible in all three retrievals, with the attenuation images showing a separation between the plies (Fig. 4-10(d), with stretched contrast in Fig. 4-10(g)). A strong signal is observed in the differential phase retrieval (Fig. 4-10(e) and (h)) due to the interface created between the delamination and the neighbouring plies. A strong dark field signal is also observed around the delamination (Fig. 4-10(f) and (i)), indicating the presence of the sub-pixel damage. Identification of the features observed in the dark field signal is not directly achievable, but it could indicate that either the delamination (ply-separation) extends further than observed in the attenuation and differential phase signal (Fig. 4-10(j)), or additional micro-damage, e.g., debonding, micro-matrix cracks, or fibre damage. These features are better visible in the 3D renderings shown in Fig. 4-10(h) and (i) with enhanced contrast to highlight the interfaces of the delamination in the differential phase signal and the surrounding damage in the dark field image, respectively. These micro-features are unique to the dark field signal and offer a more accurate representation of the possible damage extent, which could not be observed in the other signals due to the scale of those features. The complementarity of the dark field signal allows to observe features of different magnitudes and nature and thus to better understand the defects present in the sample.

The 2-dimensional cuts through the 3D rendering of the X-ray signals (Fig. 4-11) show that the delamination is not complete, but is shaped as a ring around the impact damage which pushed the central part of the specimen downwards and caused the protrusion. The differential

phase and dark field renderings show smaller interfaces and delaminations within the protrusion, in addition to the main delamination.

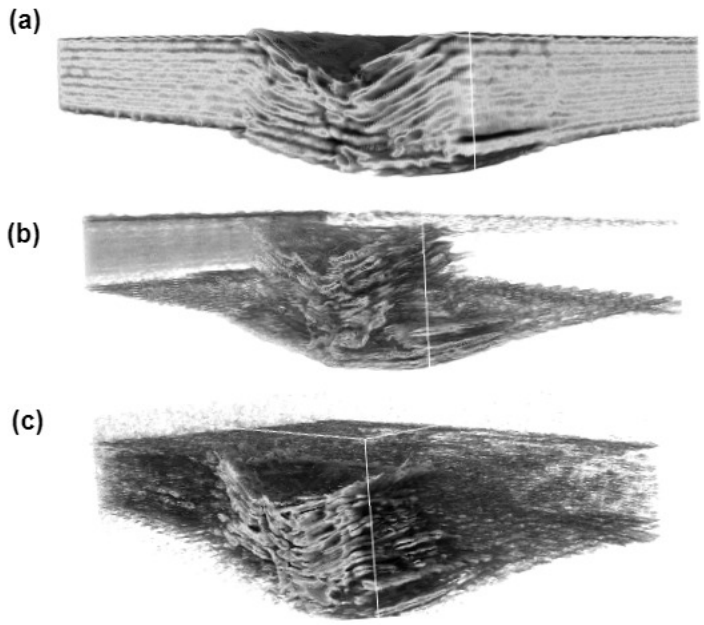

Figure 4-11 *2-directional cut through 3D rendering showing the shape of the delamination around the main impact damage in the retrieved X-ray (a) attenuation, (b) differential phase, and (c) dark field signals.*

4.6.3 Center of Damage

The impact caused damage across the sample, as can be seen from both the ultrasonic B-scans (Fig. 4-12(a) and (b)), and the X-ray images across the impact centre. The ultrasonic B-scans exhibit one of the limitations of ultrasonic testing for damage detection in composite plates. The indented front surface and protrusion cause strong reflections and scattering, potentially causing internal defects being missed due to lack of signal past the damage closest to the surface. An example of such a situation is observed here, where a crack across the thickness of the sample was only observed in the X-ray images (Fig. 4-12). The macro-crack was observed in all three X-ray retrievals, however they indicate different features; the attenuation CT slice (Fig. 4-12(d)) shows clear damage in the sample, with the

crack and further damage better visible with enhanced contrast (Fig. 4-12(g)). The differential phase signal (Fig. 4-12(e) and (h)) highlights the interface of the crack through the sample, whereas the dark field signal (Fig. 4-12(f) and (i)) indicates further micro-damage in the sample surrounding the crack. This level of accuracy in the measurement of the damage extent is unachievable using ultrasonic imaging or conventional attenuation-based CT alone, represented here by the retrieved attenuation images (Fig. 4-12(d)).

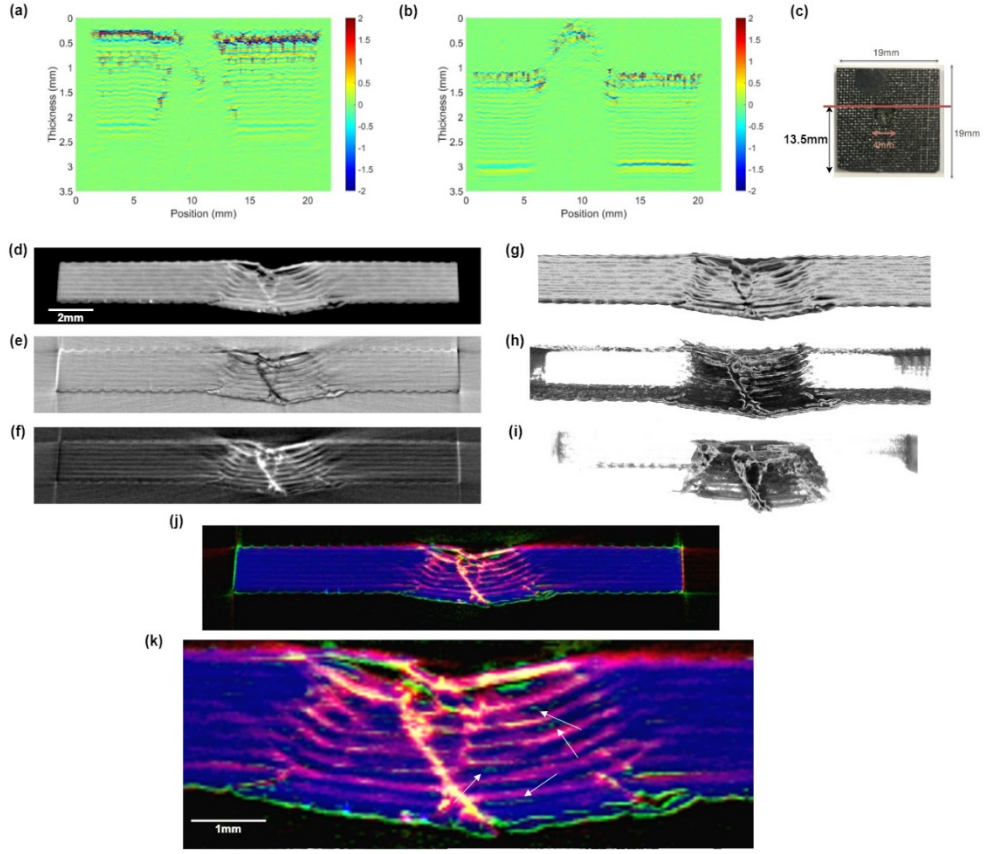

Figure 4-12 *Center of damage: ultrasonic B-scan with (a) front surface (indent) and (b) back surface (protrusion) facing the transducer (colour scale signal voltage in volts); (c) position of B-scans and cross sections within the sample; cross-section of retrieved X-ray (d) attenuation, (e) differential phase, (f) dark field CT reconstructions; 3D rendering of the sample for retrieved (g) attenuation, (h) differential phase, (i) dark field; (j) superposition of the retrieved EI XPCi CT images with attenuation (blue), differential phase (green), dark field (red); (k) zoom impact damage.*

Moreover, a clear dark field signal can be observed throughout the damaged area of the sample. The presence of signal in the different retrievals indicates the presence of different types of damage (Fig. 4-12(j)). The signal in the differential phase images is due to the small voids created by the separation of plies in the inter-ply area originating from the material being displaced when the damage occurred, as shown in Fig. 4-12(k). The dark field signal is due to the micro-damage that occurs within the plies due to the material displacement. The multimodal imaging of the sample, as well as the superposition of all three retrievals in an RBG image, as shown in Fig. 4-12(j) and (k), thus allows locating and clearly visualising the damage, as well as identifying the scale of damage involved. Refraction and scattering images provide a more accurate representation of the extent of the damage, which complements the information available from the absorption and ultrasonic images.

4.7 High-Resolution X-Ray CT imaging

The features observed in the EI XPCi signals were compared to a high-resolution X-ray CT scan performed using a commercial system with voxel size of $14\mu m^3$, as shown in Fig. 4-13. The higher resolution attenuation CT scan (Fig. 4-13(b)) confirms the features observed from the lower resolution differential phase, and dark field signals. This is more clearly visible in Fig. 4-13(c) and(d), where respectively the differential phase and dark field signals were superimposed on the high-resolution attenuation scan. The interfaces and delaminations observed in the differential phase signal are confirmed by the high-resolution scan (Fig. 4-13(c) arrows). The presence and extent of those interfaces confirm the interpretation as to the nature of the differential phase signal. Small voids created between the plies, not visible in the low-resolution attenuation scan (Fig. 4-13(a)), became visible in the high-resolution attenuation scan (Fig. 4-13(b)), and match the superimposed dark field signal (Fig. 4-13(d)).

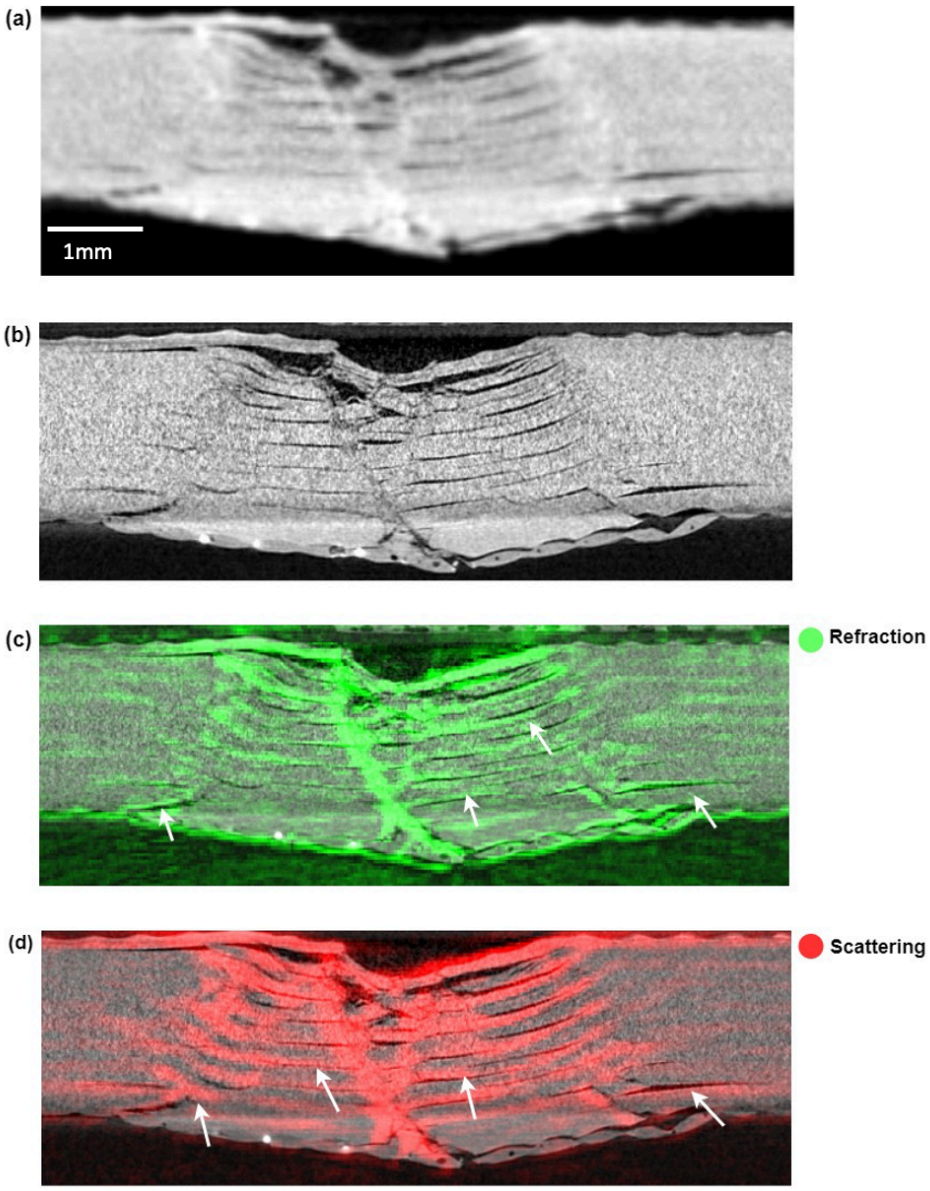

Figure 4-13 *Comparison of CT slices showing crack observed in the sample for (a) low resolution attenuation scan; (b) high resolution attenuation scan using a commercial system; superposition of the high-resolution attenuation scan with (c) low resolution differential phase signal (green) and with (d) low resolution dark field signal (red). White arrows representing features observed in the phase based signals and confirmed using the high resolution X-ray CT, nominally the interlaminar separations in the damaged area observed in the differential phase signal (c) and the extent of the delamination observed in the dark field signal (d),*

The dark field signal extends beyond the damage visible in the high-resolution scan in certain areas, suggesting that an even higher resolution scan would be needed to observe these features to their full

extent. This confirms our hypothesis that the dark field signal indicates micro-damage at a scale below the resolution of the imaging system.

4.8 Conclusions

A severely impacted CFRP was used for the evaluation of damage using different NDE techniques. The main, severe indent was accompanied by a range of adjacent damages on smaller and intermediate scales, offering the possibility to localise and differentiate between defects of different size and severity using the EI XPCi contrast channels, highlighting their complementarity. Further research should be conducted to benchmark the sensitivity of EI XPCi for the detection of small defects, e.g., using a sample with BVID.

An ultrasonic investigation was carried to evaluate the best frequency needed to assess the damage in a severely damaged CFRP. Three different frequencies were used, resulting in a 20MHz focussed transducer yielding the best results, as it offered better resolution than an unfocussed 10Hz transducer, and detected the same extent of damage as a focussed 30MHz transducer, with less signal attenuation. A delamination was observed to surround the main damage area using double through transmission C-scan imaging and located within the thickness of the sample using B-scan imaging. A qualitative comparison between ultrasonic immersion C-scan imaging and EI XPCi images was performed on a small, cross-ply composite sample with severe impact damage to investigate the different features observable using the two imaging techniques. Standard ultrasonic immersion C-scan imaging allowed the detection and sizing of the overall damage, using both B-scans and C-scans time-gated at different areas of the sample thickness. The delamination close to the bottom layer was accurately sized with good contrast from the C-scans (Fig. 4-2). However, two main limitations of ultrasonic scanning were observed. Good penetration depth and a clear reflection of the respective back wall was seen, but the chosen ultrasonic frequency (20 MHz) corresponded to a wavelength comparable to the ply layer

thickness. Together with a non-smooth sample surface, this made an accurate measurement of ply layer thickness and waviness difficult. The second limitation can be seen in Fig. 10(a) and (b), and Fig. 12(a) and (b), where strong reflections at large defects (e.g., delamination) prevented the detection of additional, internal defects.

EI XPCi resolves some of these limitations by offering a higher resolution as well as visualisation of the full sample. The multimodal imaging using EI XPCi allowed for the retrieval of attenuation, differential phase, and dark field images. Planar images allowed to assess the damage to a comparable extent to the ultrasonic imaging (Fig. 4-7 and 4-8), with a square shaped damage observed in the phase-based signals, that were not observed in the attenuation images or the ultrasonic imaging. Even though the area of damage detected by the double through transmission ultrasonic imaging was larger than the area observed by the planar EI XPCi, the shape and scale of the damage was better identified using the phase-based signals of EI XPCi. The improved resolution of the system allowed for a better visualisation of the different plies within the sample, which could not be achieved using ultrasonic imaging. However, the planar EI XPCi images did not allow for the localisation of the damage through the depth of the plate.

EI XPCi CT was used for the detection of internal defects and features that are not visible using ultrasonic imaging or planar x-ray imaging, more specifically in this case, a crack through the thickness of the sample (Fig. 4-12). The multimodal imaging using EI XPCi, resulting in the retrieval the three signal channels, contributes to the identification of the defects occurring in the damaged area. The differential phase signal highlights interfaces due to the separation of plies (small voids and delaminations), and the dark field signal corresponds to sub-pixel features which indicate micro-damage accompanying the main defects. Combining the features observed from the different X-ray retrievals, an accurate estimation of the

damage extent can be obtained from a low-resolution system relative to ultrasonic imaging or higher resolution conventional X-ray CT. Based on the physics of the different signals, some assessment of the detected damage type can be obtained, but below the system resolution only the presence of damage can be obtained from the scattering signal, not its nature – other than it takes place on a length scale smaller than the system's resolution.

5 Contrast Agent X-ray Imaging for Damage Detection compared with EI XPCi and Ultrasound

5.1 Introduction

This chapter follows up from the benchmarking of Chapter 4 and presents a comparison between planar EI XPCi and Ultrasonic immersion C-scan imaging with contrast agent X-ray imaging, another common NDE technique used for damage detection in composite plates. A composite plate sample with severe impact damage was imaged for an investigation of the type, extent, and location of the damage in the plate. In the first part of this chapter, the images of the sample from each of the imaging techniques are shown, along with a description of the damage observed. The second part of this chapter aims to compare the damage detection capabilities of each imaging technique by overlaying the images, discussing which types of defects are observed and to what extent, as well as their observed limitations. Part of the analysis presented in this chapter was submitted to Composite Structures in a paper entitled “A Comparison between Edge Illumination X-Ray Phase Contrast Imaging, X-ray Contrast Agents and Ultrasonic Immersion C-scan Imaging for Damage Detection in Composite Plates” (under peer-review).

5.2 Specimen

The specimen used in this investigation was produced by the University of Sheffield using conventional layup and autoclave method. The pre-preg was manufactured using carbon-fibre Tenax HTS (65%) pre-impregnated with Cytec 977-2 epoxy resin (35%). The 250 μm thick plies were layered symmetrically in a [0,90] sequence of 8 plies in total, forming a 2 mm thick panel. A flexible printed circuit board made of polymide film was placed between the 7^{th} and 8^{th} plies. This film was used to measure electrical resistance, for a previous

study at the University of Sheffield. Impact damage was induced in the plate using a hemispherical 1 kg mass of 15 mm in diameter, which was dropped onto the plate from a height of 0.75 m, resulting in an impact energy of 7.4 J [138,161]. A small crack and indentation are visible on the surface of the composite plate due to the impact, as seen in Fig. 5-1.

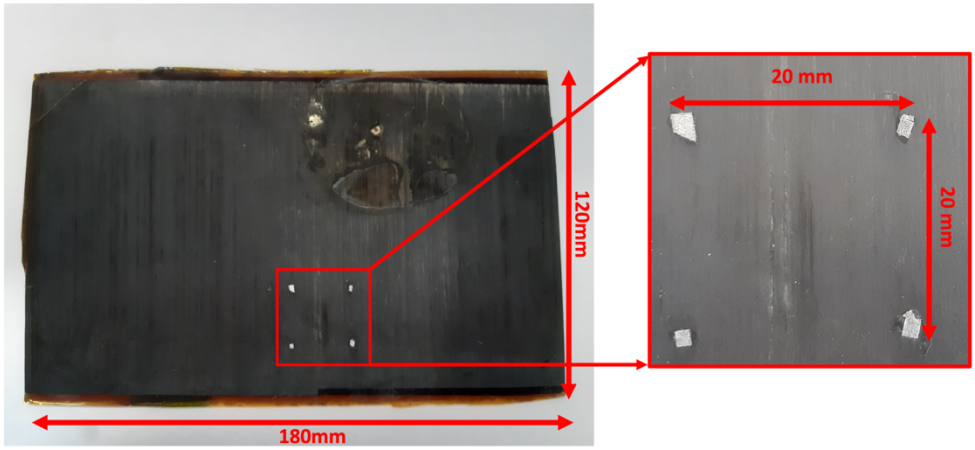

Figure 5-1 *Photograph of cross-ply composite sample, 8 plies of [0,90] with a mid-plane symmetry, with close-up on impact damage in plate (right), induced using a hemispherical object dropped with impact energy of 7.4J.*

An ROI of 20*20 mm^2 was delimited around the visible indentation using reflective tape to be used as markers for all imaging methods.

5.3 Experimental Methods

The composite plate specimen was imaged using ultrasonic immersion C-scan imaging and EI XPCi as explained in Chapter 3.3.1, as well as with contrast agent X-ray imaging.

5.3.1 Immersion Ultrasonic C-scan Imaging

The sample was imaged using ultrasonic immersion double-through transmission, similar to the way the Nikon sample was imaged as discussed in Chapter 4. A 15 MHz focussed transducer was used to scan the sample in water, with a ¼ inch (6 mm) diameter and a focal length, F_z, of ¾ inch (19 mm). A scan of 131 by 181 steps was taken, with a step size of 250 µm, covering an area of 32.75*45.25 mm^2, and

a resulting scanning time of about 8 hours. The full A-scans of the reflections obtained from the sample scans were recorded and processed offline in Matlab, to produce both B- and C-scans of the sample to evaluate the damage detected.

5.3.2 Edge Illumination X-ray Phase Contrast Imaging

The Edge Illumination XPCi system described in Chapter 3.4.1 was used for the image acquisition of the composite plate. The images were acquired using the "skipped" masks system. The image acquisition included 19 points on the illumination curve, with 9 taken on either side of the curve and one at the top, where both masks are perfectly aligned. 5 images of 1.2 s exposure were taken at each point of the IC for a total exposure time of 6 s, to increase image statistics. The sample was also dithered 16 times, by moving it by 4 μm along the x-axis at each dithering step. Since the system was only sensitive to phase effects in the x-direction, the sample was scanned twice, in both 0˚ and 90˚ orientations, and images combining both orientations were obtained by subtraction (for the differential phase and dark field channels), using the reflective tape markers as reference. This removes the common background and highlights the relevant signal (e.g., cracks) with sensitivity in both orientations. For the attenuation channel, the two images were combined using alpha blending, which is a process allowing to combine one image with the other using partial transparency [162].

The retrieval of the attenuation, differential phase and dark field signal was done with a different method from that described in Chapter 3.4.2. Due to the relation between the attenuation signal and the dark field signal, the three Gaussians retrieval method described in the methodology chapter led to a "spill-over" of the dark field signal into the attenuation channel. This artefact was first observed when the two attenuation images from the different orientation scans were

compared, and different features were observed in the two images, as shown in Fig 5-2.

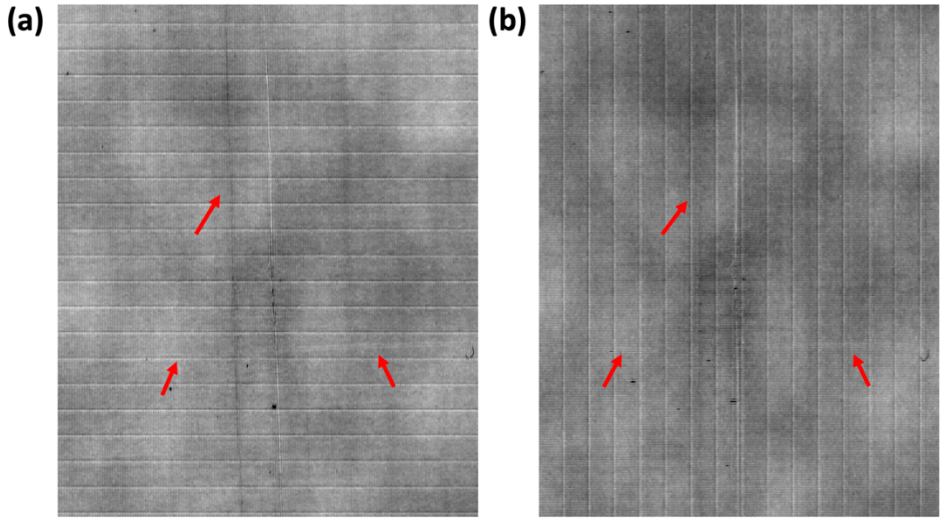

Figure 5-2 *Different orientations of the attenuation channel from EI XPCi scan: 0˚ (a) and 90˚ (b), with red arrows pointing to artefacts visible in only one orientation. The 90˚ image (b) was rotated to show the sample orientation as the 0˚ image. Mask lines are visible in both images, corrected post retrieval (see section 3.6.1).*

As can be seen from Fig. 5-2, several features are more prominent or only visible in one of the orientations, with a large vertical crack only visible in the 0˚ scan, and multiple horizontal cracks only visible in the 90˚ scan. The periodic lines observed in both images are mask lines artefacts and will be discussed later (Chapter 5.3.4). To account for the relation between the attenuation and dark field signal and separate the two channels better, a different retrieval approach was used, in which a normalised Gaussian is fitted to the beam distribution, using Equation 5-1:

$$G(x) = \frac{A}{\sqrt{2\pi\sigma^2}} exp\left(\frac{-(x-\mu)^2}{2\sigma^2}\right) \quad (5\text{-}1)$$

The addition of the variance parameter to the normalisation coefficient allows for a better fit of the different coefficients of the Gaussian, and for a better separation of the attenuation and dark field signals.

Furthermore, in this retrieval a single Gaussian was fitted instead of three. This did not affect the quality of the retrieval as the three Gaussians fit was aimed at correcting the effect of the cross-talk between neighbouring pixels, which was already rectified in this system by the use of skipped masks. The use of a normalised Gaussian corrected the dark field signal artefact in the attenuation images to a certain degree. This was checked by subtracting the attenuation images acquired in the two orientations, as the attenuation channel is not directional and should therefore yield the same image regardless of sample orientation. It was observed that some of the features were still more in one orientation with respect to the other, indicating some residual dark field signal spillover, but to a much lower extent. A reduction of 54% in the intensity of the “spilled over” features was measured when using the normalised Gaussian retrieval. The retrieved attenuation, differential phase and dark field images were corrected using the mask line removal processing tool described in Chapter 3.6.1, to remove the artefacts created during the image acquisition.

5.3.3 Contrast Dye X-ray Imaging

The composite sample was soaked in a contrast agent after the EI XPCi images were acquired. The dye used was a zinc iodide (ZnI_2), commonly used for damage detection in composite samples when contrast enhanced radiography is used [94], as described in Chapter 2.5.2. Zinc iodide is soluble both in water and alcohol, and a mixture of all three components, as well as a wetting agent, was prepared. An alcohol-based staining was favoured as it allowed for a faster drying[93]. The preparation of the dye was based on the method described in [98], where, for 250 g of zinc iodide, 80 ml of distilled water, 80 ml of isopropanol and 1ml of wetting agent were added to the mixture. Here, 50 g of zinc iodide were used, requiring the addition of 16 ml of distilled water, 16 ml of isopropanol and 0.5 ml of wetting agent. Once the mixture was prepared, the composite was left to soak

in a container for 24 h. The sample was then removed from the dye and left to air dry for a further 24 h before being scanned using conventional radiography. Unfortunately, the original markings around the damaged area were washed off by the dye, and new markers were placed around the visible crack, as shown in Fig. 5-1 and 5-3.

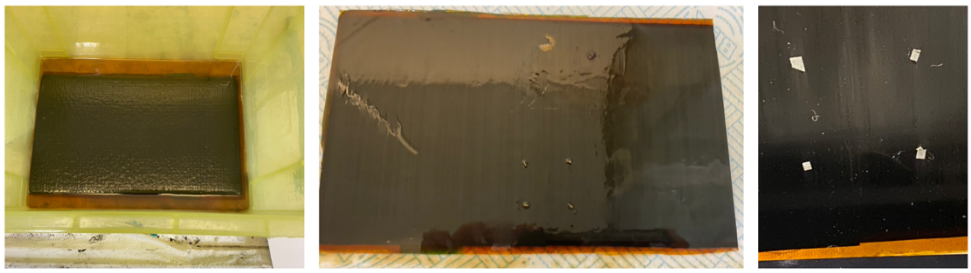

Figure 5-3 *Preparation of the cross-ply composite plate by soaking in zinc iodide dye (left) for 24h; sample removed from dye and air dried (middle); new markers (right) around the visible crack.*

The setup used to scan the composite sample with contrast dye was the EI system, with the sample and detector masks removed, which transforms it into a conventional radiography system. The current had to be reduced to 10 mA to prevent the detector from saturating; however, since this was not sufficient, an additional 0.8 mm thick aluminium filter was positioned in front of the source to reduce the x-ray flux. The addition of the aluminium filter reduced the photon count substantially and altered the X-ray spectrum, reducing the fraction of low energy photons thus resulting in a higher percentage of high energy ones. The molybdenum source spectra, filtered by 0.8 mm of aluminium and by the 0.8 mm graphite substrates used in mask fabrication (to replicate the situation encountered in EI XPCI imaging) are compared in Fig. 5-4.

Both spectra are dominated by the molybdenum characteristic emission spectral lines, at 17.5 and 19.6 keV, which leads to a comparable average energy with both filters, with the EI XPCi system averaging at 18.0 keV, and the maskless system with the aluminium filter averaging at 21.9 keV. This notwithstanding, it is expected for the

contrast achieved by the maskless system to be slightly lower than the attenuation images of the EI XPCi system.

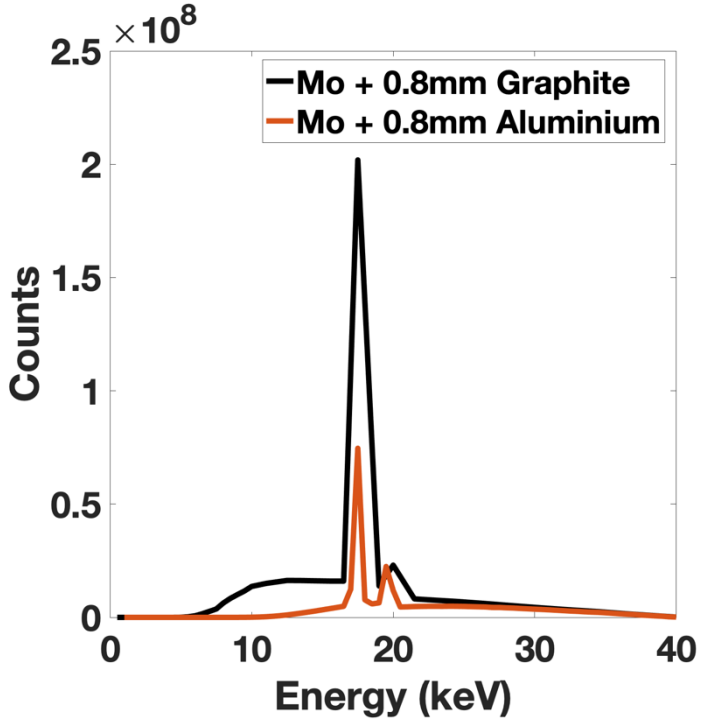

Figure 5-4 *Spectrum of the emitted x-rays with masks' graphite substrates (black) and with the addition of an aluminium filter (maskless system) (red).*

The acquisition time was adjusted so that the overall photon count for the EI images and the conventional radiography images were approximately matching. This was achieved with a total exposure time of 2.4 s, obtained by summing two 1.2 s images. The images were then corrected by subtracting a dark image (acquired with the source turned off) and flat field corrected (divided by a flat field image). The composite sample was imaged using the maskless system before and after soaking in the zinc iodide dye, so that both conventional and contrast-enhanced x-ray imaging could be compared to EI XPCI.

5.4 Ultrasonic Imaging

The A-scans obtained from the ultrasonic immersion imaging were used to produce different types of C-scans, as well as B-scans and a 3D representation of the damage observed within the sample.

5.4.1 Ultrasonic C-scan imaging

C-scans were produced, showing the front surface of the composite sample, the lower-surface reflection, the sub-surface reflection, corresponding to the reflected signal between the front and back surface, and lastly the double through transmission C-scan, corresponding to the reflection from the stainless-steel plate placed below the composite sample. This was achieved by time-gating the signal around the respective reflections, as for the sample in Chapter 4.4.1, and plotting the positive maximum or negative minimum amplitudes for each scan point, respectively. Due to some uncertainty in the time gating of the lower surface, it is possible that some sub-surface features were included in the lower surface plot and vice versa. The C-scans in Fig. 5-8 show the scanned area centred around the damage.

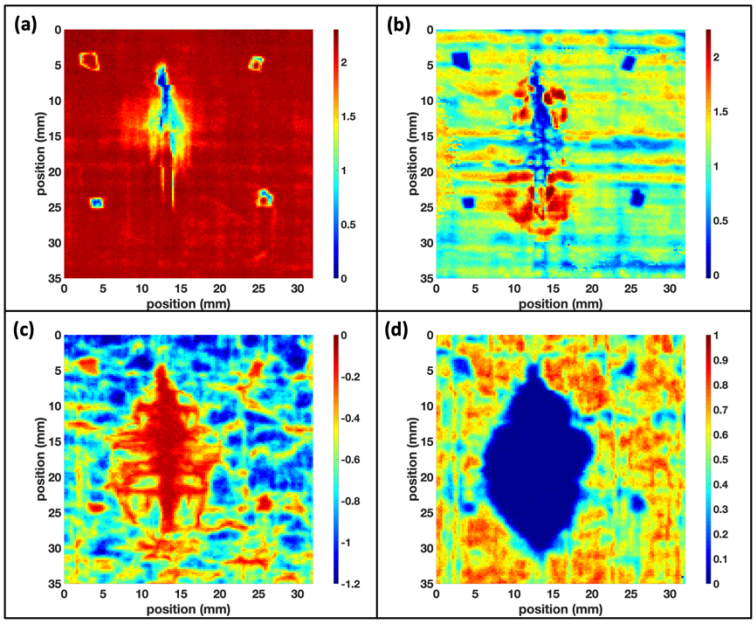

Figure 5-5 *Ultrasonic C-scans of the composite sample showing (a) the surface reflection, (b) the sub-surface reflection, (c) the lower surface reflection and (d) the double through transmission C-scan.*

The first scan to be analysed was the double through transmission C-scan (Fig.5-5(d)), as it gives an overall assessment of the damaged

area within the sample. It shows that the oval shaped damage extends over an area of approximately 25*15 mm^2, with a complete lack of signal indicating the presence of delaminations. Low reflection areas are also observed extending throughout the scanned area, and are thought to indicate the presence of fibre-associated damage across the plate, as those low amplitude reflections have an appearance that resembles the sample's cross-ply structure. From the front surface C-scan (Fig. 5-5(a)), the cracks visible on the sample surface can be seen, as well as the surface indentation from the impact. The damage on the surface covers an area of about 20*5 mm^2, with the four features in the corners of the C-scan corresponding the reflective tape strips used as markers. Two long cracks can be observed in the lower part of the surface of the sample, extending from the central indentation. The sub-surface C-scan (Fig. 5-5(b)) shows the extent of the damage around the main cracked area. Strong reflections (red) are observed around the surface cracks (blue) over an area of 25*10 mm^2, showing how the damage extends further within the sample. These strong reflections could be originating from delaminations around the main impact area, as observed in the double through transmission C-scan. Vertical and horizontal features are observed throughout the scanned area, which are thought to indicate fibre bundles-associated damage, however this was not confirmed using a different imaging method. Lastly, the lower surface C-scan (Fig. 5-5(c)) shows the overall damage across the plate, with a lack of signal (red) corresponding to damaged areas. The overall main damage is seen to extend across an area of 25*15 mm^2, with some additional features extending across the entire scanned area. Here too, areas of damage seem to extend beyond the main area surrounding the indentation, with lack of reflections visible throughout the scanned area.

5.4.2 Ultrasonic B-scan imaging

To further analyse the damage and localize it through the thickness of the plate, B-scans were generated using the estimated velocity in the

sample to convert reflection time to depth, looking at cross-sectional cuts at different locations in the plate.

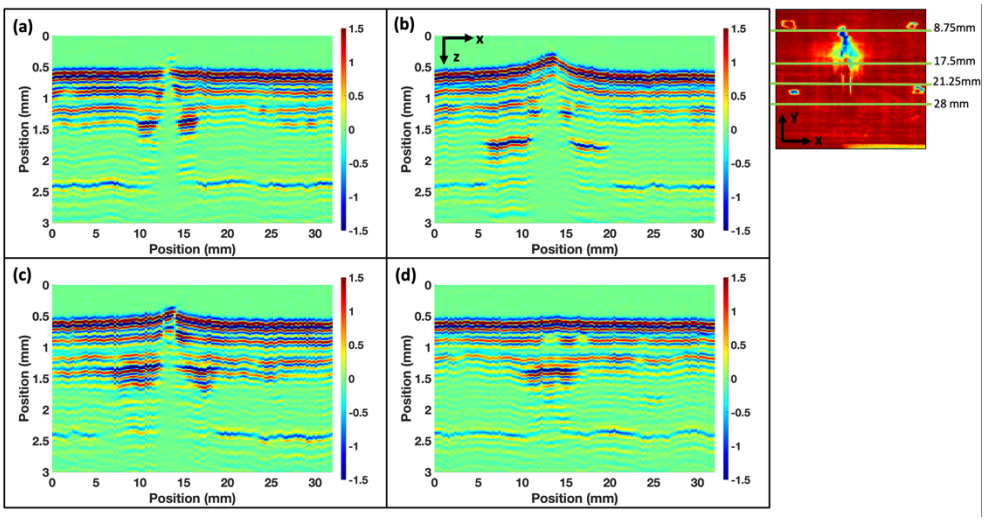

Figure 5-6 *B-scans slicing through the damaged area at different locations showing the internal damage, taken at (a) 8.75 mm, (b) 17.5 mm, (c) 21.25 mm and (d) 28 mm from the top of the C-scan (top left).*

The B-scans show the location of the damage within the sample and allow an understanding of how the defects propagated. At the top of the imaged area (Fig.5-6(a)), where the surface crack starts to form, a delamination can be observed from the strong reflections on either side of the crack, at 1mm depth from the surface, about 5 mm in length. From the B-scans at other locations of the damaged area (Fig. 5-6(b)), the strong reflections are observed at larger depths and are wider, about 15 mm in length. This could indicate that multiple, smaller delaminations have spread between different ply layers, due to the severity of the damage [163]. This is further confirmed by Fig. 5-6(c), where strong reflections are observed across several plies, but at a depth similar to the delamination observed in Fig. 5-6(a). The delamination extends beyond the surface damage, as can be seen from Fig. 5-6(d) in which, while the surface damage is no longer visible, the reflection from the delamination is still detected.

The A-scans of the composite sample were used to create a 3D rendering of the sample, showing the damage propagation through the whole scanned area, as shown in Fig. 5-7. This was done by thresholding the signal to only keep the strongest reflections, which correspond to reflections from the first plies and inner defects. The signal was then plotted using a 3D visualisation tool in Matlab. The maximum amplitudes rendering, which highlights the highest amplitudes across the whole volume, was also added as it enables a better visualisation of the damage within the sample.

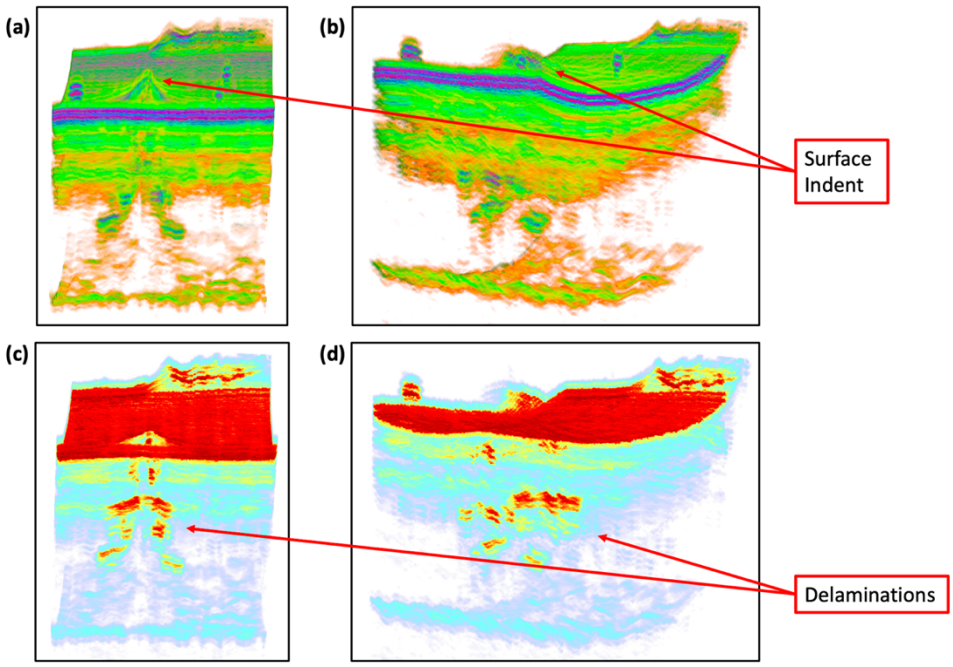

Figure 5-7 *3D rendering of the ultrasonic immersion through transmission scan, showing strong reflections throughout the thickness of the sample in different orientations (a, b) as well as the maximum amplitude for each A-scan (c,d).*

The propagation of the damage is clearly visible through the 3D rendering of the ultrasonic signal. The delaminations formed across different plies, propagating from the impact point and through the thickness of the sample, become wider with depth. This visualisation complements the observations made from the C-scans and the B-scans.

5.5 Contrast Dye compared to conventional X-ray imaging

The sample was imaged with the "maskless" EI XPCi system (corresponding to standard attenuation-based X-ray imaging) both with and without the contrast dye (ZnI_2), with the results shown in Fig. 5-8. The attenuation channel from the EI XPCi system is also shown here for comparison, so that attenuation images obtained with all three approaches can be compared directly.

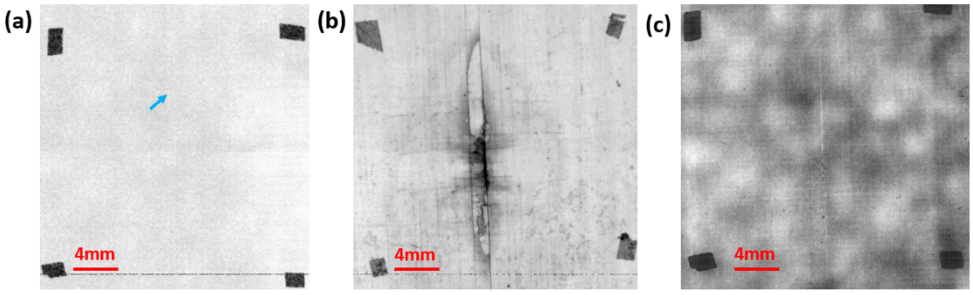

Figure 5-8 *Attenuation images of the damaged areas of the composite sample without (a) and with (b) the ZnI_2 contrast dye, and the attenuation channel retrieved from EI XPCi (c). The blue arrow (a) points toward the main crack in the attenuation image without contrast dye, which is barely visible.*

As can be observed, the use of contrast agent for conventional radiography significantly improves the contrast of the damage features and shows a much greater extent of the damage compared to the standard attenuation image. While in the attenuation image without contrast agent only a single vertical crack is faintly visible, the penetration of the highly attenuating contrast agent allows for the network of cracks to become visible, showing the two main vertical cracks previously observed in the ultrasonic C-scan images, along with smaller horizontal cracks surrounding the main impact area. The EI XPCi attenuation image shows the same vertical crack observed in the maskless attenuation image, with a better resolution. This is expected as the dithering of the EI XPCi scan allows to obtain a resolution equal to the sample mask aperture [157,164], i.e. 12 μm, compared with the conventional attenuation scan which has a resolution driven by the detector performance, i.e. 100 μm.

Additionally, the contrast of the EI XPCi attenuation image is also relatively higher than that of the maskless scan due to the additional beam filtration in the latter case. Furthermore, some features are also more pronounced in the EI XPCi attenuation image due to the dark field signal spillover mentioned earlier.

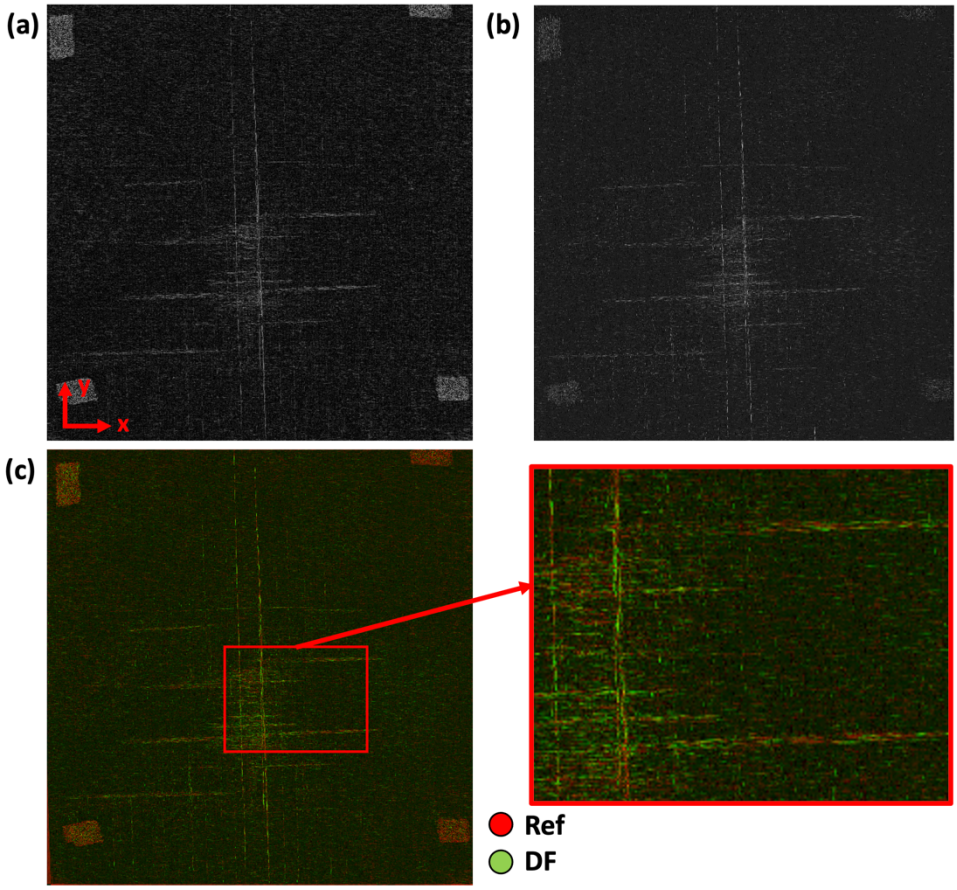

Figure 5-9 *Combined images from two orthogonal orientations of the EI XPCi differential phase (a) and dark field (b) signal, showing sensitivity in both the x- and y-directions, and an overlay of the differential phase (red) and dark field (green) signals (c), with an additional zoom-in of a severely damaged area with interlaminar cracks, showing complementarity between the two signals.*

The differential phase and dark field images were retrieved for both the 0˚ and 90˚ scans, and an image overlaying both orientations was produced to have sensitivity along both the x- and y-direction, as shown in Figure 5-9. An additional overlay of the differential phase and dark field signal shows the different features observed in both signals.

A clear network of cracks spreading from the point of impact can be observed in both the differential phase and dark field images, which was not observed in the ultrasonic imaging. Two main vertical cracks can be observed, which were also visible in the ultrasonic C-scan (Fig. 5-9(a)), called axial splits, and a series of large horizontal cracks around the impact point area, traditionally called matrix cracks, with additional smaller cracks propagating from the larger defects. Both types of cracks are known to trigger the formation of delamination in CFRPs. From the overlay of the two signals shown in Fig. 5-9(c), the contributions from the differential phase (red) and dark field (green) signals can be appreciated. As was previously shown in [165], the presence of signal in either differential phase or dark field reflects the different scales of the defects, with predominately red areas indicating that the cracks are of a scale equal to or above the system resolution (12 μm), while predominantly green areas indicate the presence of micro-cracks on a smaller scale (<12 μm). It can be observed that some cracks only show up in the differential phase signal, indicating that no micro-damage is accompanying them, while some larger cracks are surrounded by dark-field signal, suggesting that additional micro-cracks are emerging from the main crack. Additionally, some of the cracks observed are only visible in the dark field signal, indicating the presence of very fine micro-cracks. This complementarity between the differential phase and dark field signal allows a better understanding of the spread of the damage, as well as of the scale of the cracks, providing hints on the progression of the damage across the plate.

5.6 Comparisons of all Imaging Techniques

To compare the extent of detected damage across all X-ray imaging techniques, the two phase-based X-ray signals were overlayed on the contrast dye attenuation image, as shown in Fig. 5-10. The images were overlaid using the two vertical cracks as markers, since the reflective tape markers were washed away and had to be replaced. As

can be seen from Fig. 5-10, the extent of damage detected by EI XPCi is larger than that observed with the contrast dye. This is because the contrast agent can only enhance the features where it penetrated, i.e., if no direct path exists between a feature and the impact point, the contrast agent cannot reach it, thus leaving it undetectable. Several long cracks were detected in the differential phase signal, but were barely or not at all visible in the contrast dye images; these are highlighted with the blue arrows in Fig. 5-10(b). Additional features detected by the dark field but not by the differential phase signal are highlighted by the purple arrows in Fig. 5-10(c), corresponding to micro-cracks of a scale smaller than the system resolution.

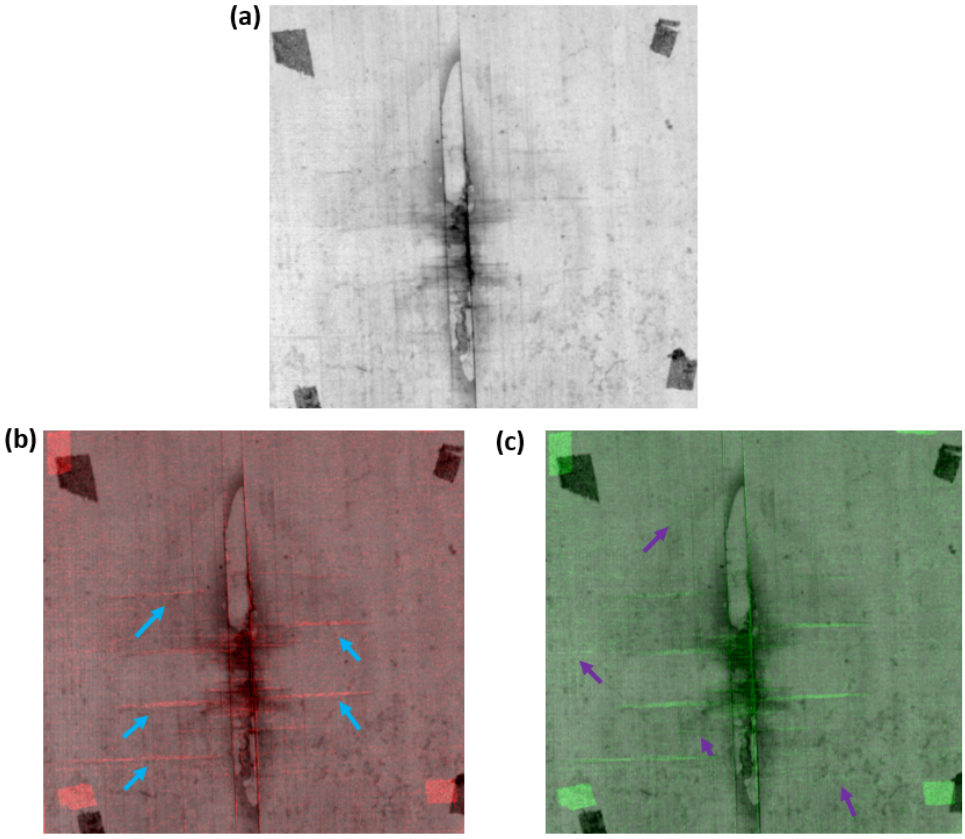

Figure 5-10 *ZnI_2 contrast agent attenuation image (a) with an overlay of the differential phase signal (b) in red and of the dark field signal (c) in green.*

This shows that EI XPCi can give a better estimation of the damage extent in the sample than conventional radiography even when this is enhanced with contrast agents. An additional advantage of EI XPCi is

the dark field signal, which complements the differential phase signal by allowing an estimation of the damage extent on a scale below the system resolution.

An additional comparison was done between the different X-ray imaging techniques and the ultrasonic C-scan imaging, by overlaying the contrast agent X-ray image (Fig. 5-10(a)), as well as the overlay of the differential phase and dark field images (Fig 5-9(c)), with the back-surface ultrasonic C-scan, shown in Fig. 5-11.

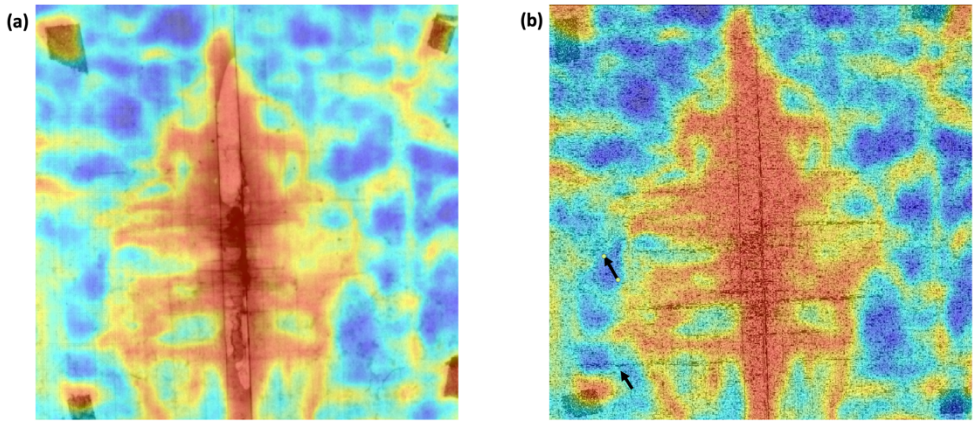

Figure 5-11 *Overlay of the contrast agent X-ray image (a) and of the combined differential phase and dark field signals (b) on the ultrasonic back-surface C-scan*

The overlay of the contrast agent X-ray imaging and the ultrasonic lower surface C-scan show an almost perfect match, with the extent of the damage detected by the X-ray comparable to the extent observed by the ultrasonic C-scan. Moreover, from the overlay of the differential phase and dark field signal X-ray image (Fig. 5-9(c)) with the lower surface C-scan (Fig. 5-11(b)), the two main, vertical cracks at the centre of the impact area match the damage observed with ultrasound. However, the individual horizontal cracks detected by EI XPCi are not visible in the ultrasonic imaging. The extent of the damage observed from the EI XPCi signals is in general similar to the extent observed in the ultrasonic images (i.e., an area of 25*15 mm^2). However, a number of the horizontal cracks observed in the differential phase and dark

field signal (black arrows in Fig. 5-11(d)) extend up to 5 mm further, showing damage extending beyond the boundaries detected by the ultrasound. It should be noted that neither of the X-ray imaging methods could detect the delamination observed in the ultrasonic imaging, thus showing the necessity of using multiple techniques for a complete assessment of the damage in the sample.

5.7 Conclusions

EI XPCi was used to image a CFRP plate with impact damage and compared to both ultrasonic immersion C-scanning and contrast agent-enhanced X-ray imaging, two standard methods for damage assessment. The main limitation of contrast agent X-ray imaging is the need for a direct path between the point of impact and the peripheral damage features, to allow for the contrast agent to reach a certain feature. This limitation is avoided in EI XPCi, which only relies on the presence of interfaces in the sample, in this case created by the impact. The dark field signal offers complementarity to the differential phase signal as it originates from features in the sub-pixel scale. Further micro-cracks were detected in the sample, and a rough estimate can be provided on the relative scale of the different damage features.

The refraction and dark field signals provided by EI XPCi were shown to detect cracks to a larger extent and with more detail than ZnI_2 contrast agent X-ray attenuation and ultrasonic immersion C-scan imaging. The use of ultrasonic imaging, however, is still needed as neither of the planar X-ray imaging methods could detect the delamination observed in the ultrasonic double through transmission scan. Delaminations cause slow and progressive density gradients in directions along the plate, which do not translate into noticeable X-ray refraction effects. While this applies only to projection (2D) imaging where the X-rays are orthogonal to the plate and could probably be solved by full (CT) or partial (laminography) 3D approaches, it

indicates a need to use EI XPCI in conjunction with ultrasonic imaging where only 2D projection imaging is possible (e.g., fast scanning on production lines).

6 Quantification of porosity in woven fibre composite plates using ultrasonic signal attenuation and EI XPCi

6.1 Introduction

This chapter presents the quantification of porosity in woven CFRP plates manufactured using an autoclave cure. The porosity was quantified by the University of Manchester using matrix digestion and ultrasonic imaging. In this chapter, both ultrasonic through transmission imaging and planar EI XPCi were used to quantify the porosity in the plates and compare them to the values obtained from matrix digestion. A new approach was introduced, using the standard deviation of the differential phase signal to quantify the porosity in the plates for features of a scale equal to or above the system resolution. The aim of this chapter was to investigate EI XPCi as a viable method for the quantification of porosity in composite plates, in addition to its already proven viability for damage detection. The first part of this chapter includes the ultrasonic analysis and porosity quantification using different transducer frequencies. The second part of this chapter introduces EI XPCi, with the dark field signal and the standard deviation of the differential phase showing a correlation with porosity values from matrix digestion. The result sections of this chapter have been submitted as a paper entitled “Quantification of Porosity in Woven Fibre Reinforced Composite Plates using Edge Illumination X-Ray Phase Contrast Imaging and Ultrasonic Attenuation” to Composites Part A (under-review) (6.5-6.8), and partly reported in the the proceedings paper “Composite Porosity Characterization using X-ray Edge Illumination Phase Contrast imaging and ultrasonic techniques” [166](6.9).

6.2 Specimens

A series of specimens, consisting of 9 plates, were provided by the National Composites Certification and Evaluation Facility (NCCEF) at the University of Manchester, initially manufactured for a different project led by Rolls Royce, along with the measured porosity values for each sample plate. Nine panels of dimensions 240mm by 160mm with a 10-ply cross ply woven structure were manufactured, with a layup of M21 epoxy-carbon woven fabric prepeg plies as per Rolls Royce instructions, using an autoclave cure. The manufacturing of the specimen at Manchester was achieved using the autoclave cure procedure recommended by Hexcel[167]: pressurised to 7 bar, heated at 2˚C/min, cure dwell at 180˚C for 120 min. Then, specimens were cooled down at 5˚C/min, depressurised when below 60˚C, all under 100% vacuum for the entire duration of the cure. Each manufactured panel underwent this cure with different variations of the pressure, heating rate, and intermediate dwell to introduce varying degrees of porosity. These variations included the introduction of a debulking of the panels for different amount of time every few plies during the ply lay-up, or no debulk at all, allowing for edge breathing in some of the panels, leaving the panel in vacuum prior to the cure for different lengths of time, introducing variations in the autoclave pressure (0.5 to 7 bar), as well as variations in the heating temperature profile. One of the samples, with porosity values of 1.55%, was manufactured differently to the other plates: Instead of creating a single panel of size 240*190 mm^2, containing both the 10 plies laminate on one side and the laminate with the adhesive film on the other, two sub-panels of dimensions 120*190 mm^2 were created, one for the 10 plies laminate and another for the laminate with the adhesive film. Four specimens of 100*50 mm^2 were then extracted from each panel. In this study, the lower left extracted woven specimens were made available and thus investigated (specimen X-1-1, see Fig. 6-1). A photo of a specimen is shown in Fig. 6-2.

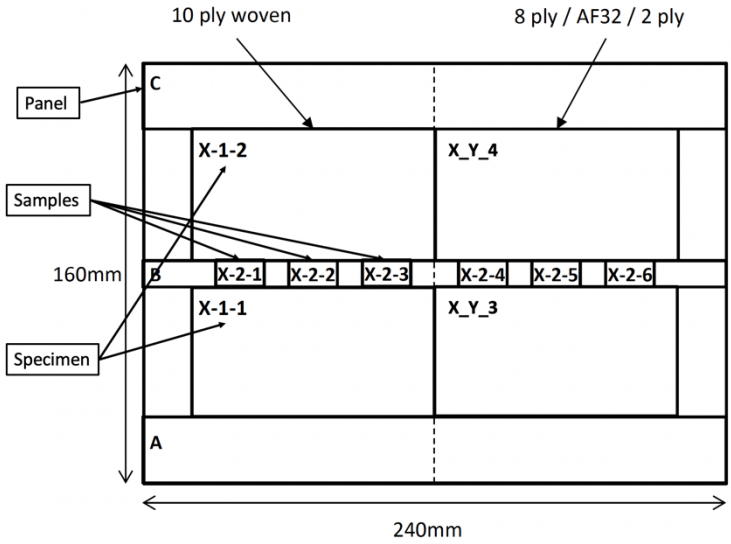

Figure 6-1 *Example of sample extraction of the porosity plates*[168].

Figure 6-2 *Specimen 1_1_1 (0.7% porosity); 10 plies woven composite plate, 100x500mm.*

In addition to the specimens extracted from the plates, a further six sub-specimens were extracted from the centre strip of each of the panels, three from each type of composite layup, as shown in Fig. 6-1. These 20*10 mm^2 sub-specimens were used for the destructive matrix digestion analysis [169] to determine the porosity content in the plates. The matrix digestion (ASTM D3171 Procedure B, BS ISO 14127:2008)[170] was carried out for void content calculations using a nominal density of 1.28 g/cm^3 for the matrix and 1.78 g/cm^3 for the fibres on all 54 sub-specimens, and used to estimate the average porosity of the extracted specimens. The calculated porosity values were 0.7%, 0.9%, 0.9% 1.3%, 1.5%, 3.9%, 5.9%, 6.6%, 10.7%[168].

The thickness of the samples was measured across all samples as well as within each of the samples. It was found that the samples had an average thickness of 3.1 mm, ranging between 2.8 mm and 3.5 mm across all plates.

An NDT evaluation was also carried out at the University of Manchester on the 9 panels prior to the specimens' extraction using ultrasonic through transmission C-scan imaging with 5MHz transmitter/receiver transducers. This analysis was used to correlate the average ultrasonic attenuation to the porosity content calculated from the matrix digestion and is shown in the results section of this chapter along with our own ultrasonic analysis.

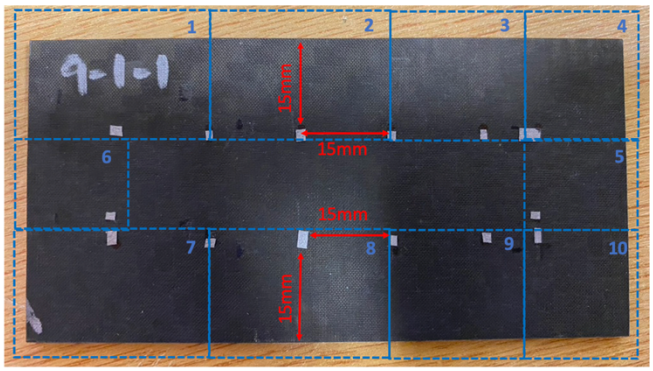

Figure 6-3 *ROI selection for porosity plates of dimensions 15mm*15mm, with corresponding X-ray scans done around the edges of the specimens delimited in blue.*

Due to restrictions from the X-ray field of view, as well as the need of a background area in the images for normalisation, the plates were split into 18 regions of interest (ROIs) of dimensions 15*15 mm^2 around the edges of the plate, which were imaged using 10 planar scans, resulting in 75% of the sample being imaged. The ROIs were delimited using reflective tape, which served as a marker visible in ultrasound and in all three channels of the X-ray imaging. The ROI selection and corresponding scanned areas are shown in Fig. 6-3. Each ROI was then analysed individually from the X-ray images and

was quantitatively compared to the corresponding ultrasonic signal obtained from the complete specimens' scans.

6.3 Experimental Setup

The nine woven composite specimens were scanned using ultrasonic through transmission C-scan imaging and Edge Illumination X-ray Phase Contrast imaging as explained in Chapter 3.

6.3.1 Ultrasonic Imaging

The ultrasonic single through transmission imaging method, described in Chapter 3.3.2, was used for the porosity specimens, as the presence of porosity leads to an attenuation of the signal, scattered by the pores in the sample[12]. A series of transducers of varying frequencies were used for comparing the relation between frequency and signal attenuation. Due to some of the plates being highly porous, thus strongly attenuating, a lower frequency was initially chosen for the scanning of the plates to ensure the signal was being transmitted through the plates. Initially, a 2.5 MHz unfocussed transducer was used for the first assessment of the plates, and subsequently a focussed 2.25 MHz transducer for higher resolution scans. Lastly, once the acquisition process was improved to ensure a sufficient part of the signal was transmitted through all samples, a 5 MHz focussed transducer was used for direct comparison with the manufacturer's scans.

A couple of unfocussed 2.5 MHz/2.5 MHz transducers (Transmitting/Receiving, respectively) were initially used. Both transducers had a 20 mm nominal diameter and were placed at a distance equivalent to the near field distance of the transducers. For the 2.5 MHz transducers, the near field distance was calculated to be 167 mm and the wavelength in water was calculated to be 600 μm using Equation 3-4. A 2 mm step was chosen for the preliminary scans of the plates with dimensions 100* 50 mm^2, resulting in 61*31 step scans. The second set of used transducers consisted of a focused

2.25 MHz (Olympus U8423330) / unfocussed 2.5 MHz. The 2.25 MHz focussed transducer had a 6.3 mm nominal diameter and a focal length of 10.2mm. The focal spot diameter was calculated to be 1.5 mm using Equation 3-1 for a wavelength in water of 667μm. The plates were scanned with a 1 mm step size for this transducer, resulting in 121*61 steps scans. The third pair of used transducers were focussed 5 MHz (Olympus U8420169) / focussed 5 MHz (Ultran XL50-5-P3) transducers. The transmitting 5 MHz transducer (Olympus) had a nominal diameter of 12.7 mm and a focal length of 19 mm. The focal spot diameter was calculated to be 650 μm for a wavelength in water of 300 μm. The receiving 5 MHz focussed transducer (Ultran) had a nominal diameter of 13 mm for a focal length of 76 mm. The focal spot diameter was calculated to be 2.6 mm. The plates were scanned with a 500 μm step size for an overall total of 221*121 steps. Prior to each sample scan, an “empty” scan (i.e., without sample) of 11*11 steps was acquired, with a step size of 2 mm in both the y- and z-directions. This was done to obtain the signal attenuation calculation described in Chapter 3.3.2, where the average attenuation of the ultrasonic signal is calculated by comparing the signal in water to the signal through the sample. The signal attenuation was calculated for the whole plates and C-scans were produced. Furthermore, the average signal attenuation over each ROI in the plate was also calculated for direct comparison with the X-ray images.

6.3.2 Edge Illumination XPCi

The edge illumination imaging setup and related methods described in Chapter 3.4 was used for the imaging of the porosity specimens. The system used was identical to the system described in Chapter 5.3.2. The image acquisition of the planar images included 19 points on the illumination curve. A longer exposure time was used to increase the signal, and 5 images of 1.2 s exposure were taken at each sample mask position and summed together, resulting in 6 s exposure time at each step. The samples were dithered 16 times, moving them by 4 μm

at each dithering step to reach a resolution in the x-direction determined by the sample mask aperture[157], i.e. 12 μm. The resolution in the y-direction was determined by the detector performance, i.e., 100 μm. The retrieval of the images was done using the three Gaussians method described in Chapter 3.4.2. After the retrieval, the differential phase images were corrected using the gradient correction processing method described in Chapter 3.6.2.

6.4 Varying Transducer Frequency for Ultrasonic Assessment of Porosity in CFRP

Three different frequencies were used in this investigation for comparing ultrasonic signal attenuation to porosity content. C-scans of the signal attenuation calculated for each of the frequencies used are shown in Fig. 6-4, along with the C-scans of the plates produced by the manufacturer using a 5 MHz transducer. Four plates were chosen out of the nine available, showing different levels of porosity across the specimens, with 10.7%, 6.6%, 3.4% and 0.7% porosity, respectively.

In the C-scans provided by the manufacturer, the light grey signal corresponds to low signal attenuation, i.e., lower porosity whereas the dark grey areas correspond to high signal attenuation, i.e., higher porosity levels. The signal distribution for all C-scans was also provided by the manufacturer and is compared to the 5 MHz measurements later. The C-scans of the signal attenuation performed using varying frequencies (2.5 MHz unfocussed, 2.25 MHz focussed and 5 MHz focussed) are shown on the same colormap scale across all four plates for each frequency. The resolution was improved, with the 2.5 MHz unfocussed scan having the largest step size (2 mm). The step size was reduced to 1 mm step size for the 2.25 MHz focussed measurement as the beam diameter was considerably reduced when compared to the unfocussed 2.5 MHz (focal spot diameter of 1.5 mm). The step size was further reduced to 500 μm for the 5 MHz focussed

transducer, resulting in an improved resolution thanks to both a smaller focal spot diameter and wavelength.

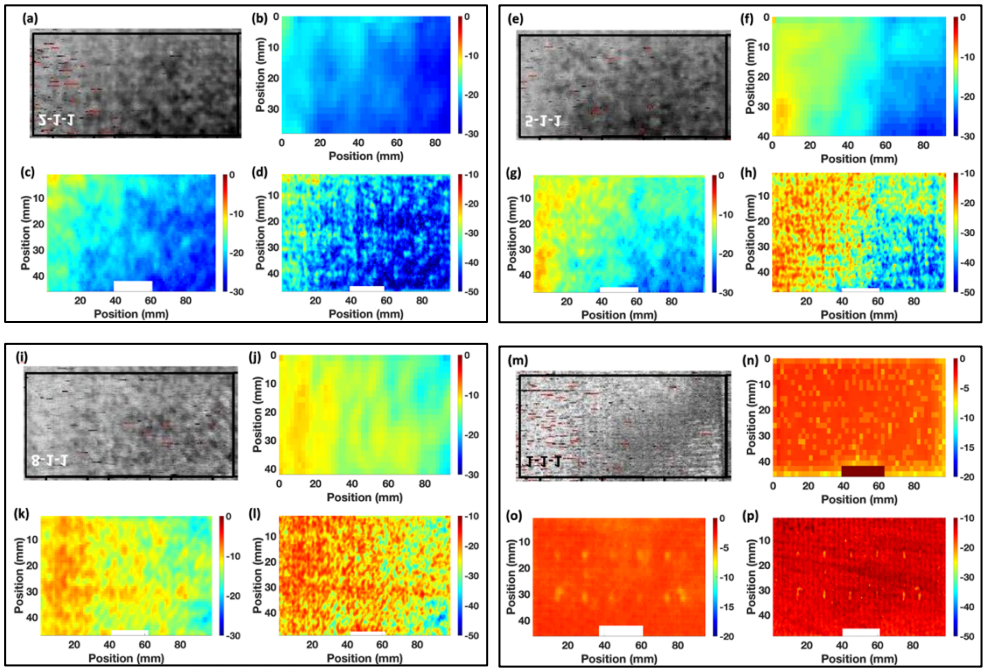

Figure 6-4 *Ultrasonic signal attenuation C-scans for four plates with varying porosity and frequencies: 10.7% (a-d), 6.6% (e-h), 3.4% (i-l) and 0.7% (m-p), showing the manufacturer's 5MHz C-scan (a, e, I, m), the 2.5 MHz unfocussed transducer C-scan (b, f, j, n), the 2.25 MHz focussed transducer scan (c, g, k, o) and 5 MHz focussed C-scan (d, h, l, p) performed as part of this thesis work for each of the four plates, respectively.*

Very similar features are visible from the comparison across frequencies for each of the plates. The manufacturer's step size was estimated to be approximately 250 µm, hence the features observed in the 5 MHz focussed C-scans are very similar to those visible in the manufacturer scans. The gradient in porosity going across all plates is visible throughout the scans, with specific small areas of high porosity visible in the two highest porosity plates. In the highest porosity plate (10.7%), a very high ultrasonic attenuation can be observed across all frequencies. The porosity is not uniform across the plate, with the highest porosity concentration observed in the bottom right part of the plate. For the 5 MHz signal attenuation C-scan, a range of 35 dB was measured across the plate, which averaged at -39 ± 6 dB, the highest

signal attenuation measured amongst all plates. For the second highest porosity plate (6.6%), the highest levels of porosity were also mainly concentrated in the bottom right corner of the plate, which had an average ultrasonic signal attenuation of -28 ± 6 dB for the 5 MHz scan, with a range of 35 dB. In both high porosity plates, it can be observed that the porosity features follow the woven pattern of the plates, as the features seem to follow both horizontal and vertical lines across the samples. This behaviour is less visible in the 3.4% porosity plate, where the porosity features seem to be following diagonal lines across the middle of the plate, but the majority of the porosity features seem to be more randomly distributed across the plate. The 3.4% porosity plate had an average signal attenuation of -23 ± 1 dB with a range of 25 dB. The lowest porosity plate (0.71%) had an average signal attenuation of -14 ± 1 dB with a signal range of 10dB, which points toward a very uniform plate with very little porosity. The yellow features observed in the plate are due to the reflective tape that was used as marker for the X-ray acquisitions and are not visible in the other three plates due to high porosity attenuation.

The average signal attenuation of each of the plate was plotted against the porosity values calculated from the matrix digestion for each of the frequencies used, as was the manufacturer's ultrasonic analysis, as shown in Fig. 6-5. The porosity values from matrix digestion were used as the baseline across the entire investigation, and both the ultrasonic attenuation and X-ray values were compared to those values.

A good correlation was observed between the ultrasonic signal attenuation and the manufacturer's ultrasonic values, and the calculated porosity values from matrix digestion for all frequencies. The lowest correlation between the ultrasonic attenuation and the porosity values was found to be for the manufacturer's analysis, with an R^2 of 0.88. However, since the no details on the used methodology are known apart from the frequency, it is difficult to understand the reasons for this. From observation, it appears that the manufacturer's

measurement of the highest porosity plate (10.7%) might be incorrect, as the average attenuation value for that plate is similar to the next two highest porosity plates (around 20dB), despite the highest porosity plate having almost twice the porosity. If highest porosity plate were to be discarded, the manufacturer's values would have a very good correlation with the matrix digestion values, with $R^2 = 0.98$.

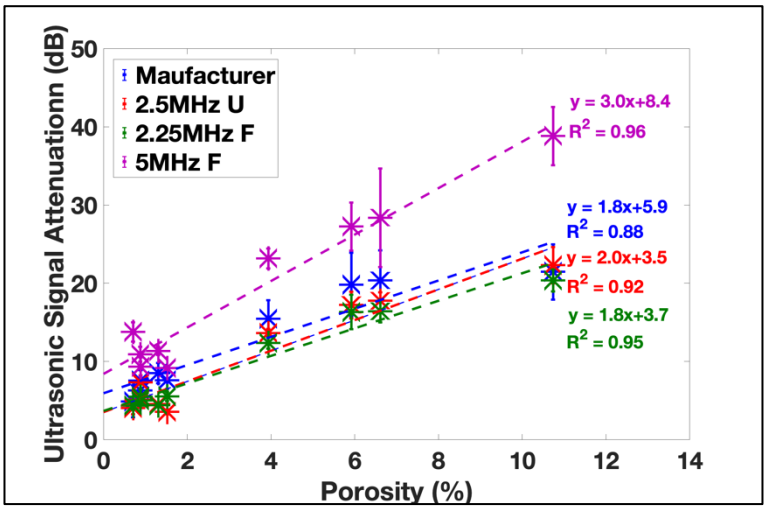

Figure 6-5 *Average ultrasonic signal attenuation for all nine plates at all investigated frequencies (Red: 2.5MHz unfocussed; Green: 2.25MHz focussed; Magenta: 5MHz focussed), plus results from the manufacturer's ultrasound analysis (Blue), plotted against the porosity content calculated from matrix digestion.*

The gradient of the fits for the 2.5 MHz and the focussed 2.25 MHz are similar, which is to be expected given the similar frequencies between the two sets of scans. The gradient of the focussed 5 MHz scans can be approximated to about twice the gradient of the 2.5 MHz, which is in line with the doubling of the frequency used. The gradient of the manufacturer's scans was expected to be similar to the 5 MHz focussed gradient, however it is lower and more similar to the 2.5 MHz and 2.25 MHz scans gradients. Since the scans parameters of the manufacturer were unknown, the reason for the discrepancy in the gradient remain unknown. For the three frequencies measured at UCL, the correlation increases with the use of focussed transducers and with the increase in frequency, which is expected as the increase in frequency leads to a better detection of porosity features. The

correlation observed from the scans varies from an R^2 of 0.92 for the 2.5 MHz unfocussed transducer scans to 0.96 for the 5 MHz focussed transducer scans, pointing toward a clear relationship between ultrasonic attenuation and porosity content in those specimens.

The correlations fit best for plates with porosity levels above 2% across all frequencies, including the manufacturer's analysis, where however the 10.7% plate does not fit the correlation either. For the plates with porosity below 2%, the ultrasonic attenuation values do not correlate well with porosity content. It was found in literature[171,172] that ultrasonic attenuation can indeed detect porosity below 2% and a correlation between the ultrasonic attenuation and porosity content can be expected, however this is not observed here.

6.5 EI XPCi for assessment of porosity in CFRP compared to matrix digestion

Planar images of all nine plates were acquired using the EI XPCi system. The X-ray attenuation, differential phase and dark field signals were retrieved, and an ROI from each is shown in Fig. 6-6 for the four plates previously shown in Fig. 6-4.

The X-ray attenuation images show similar features to the ones observed in the ultrasonic C-scans images. For the highest porosity plate (10.7%), both horizontal and vertical features can be observed throughout the ROI, indicating that the porosity features follow the woven pattern of the fibres. These features are also observed in the second highest porosity plate (6.6%), however in a less pronounced manner. On top of the features visible along the fibre yarns, additional randomly distributed features are observed across the ROI. In the mid-porosity plate (3.4%), the porosity features no longer follow the woven pattern of the fibre yarns, but are randomly distributed across the ROI. Lastly, in the low porosity plate (0.7%), no porosity features are observed in the ROI, which has an overall smooth signal distribution.

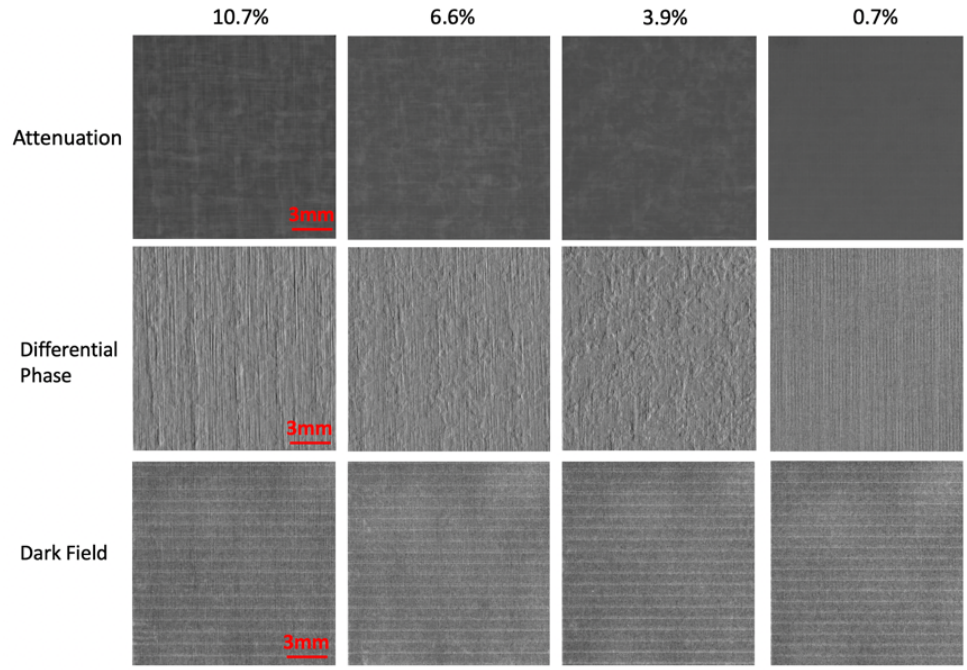

Figure 6-6 *Attenuation (top), differential phase (middle) and dark field (bottom) images of ROIs from four different plates with varying degrees of porosity (left to right: 10.7%, 6.6%, 3.4%, 0.7%).*

The XPCi system is only sensitive to phase effects in the x-direction, along which it has a resolution of 12 μm, determined by the aperture size of the sample mask. The resolution in the y-direction is determined by the detector performance, and approximately equal to 100 μm. The differential phase channel highlights the presence of inhomogeneities by enhancing their interfaces, hence showing the edges of the inhomogeneities present in the sample. The features observed in the differential phase signal images complement the observations made for the attenuation images, and the shape and structure of the features change from one plate to the other. In the highest porosity plate (10.7%), very wide vertical structures are visible, suggesting that the porosity features follow the woven structure of the plate. Only vertical features are visible, due to the one-dimensional sensitivity of the signal. Similar to the attenuation images, the vertical features are also present in the second highest porosity plate (6.6%), but in a less pronounced manner, and accompanied by additional

randomly distributed porosity features across the ROI. In the mid-porosity plate (3.4%), smaller, randomly distributed features are observed across the ROI. Lastly, in the low porosity plate (0.7%), no porosity features are observed either. The vertical lines appearing in the ROI are due to the structure of the specimen.

Lastly, in the dark field images of the ROIs, no specific features are observed for all porosity values. As mentioned above[136,165], the dark field signal is sensitive to variations in inhomogeneity distribution on the sub-resolution scale. Since no variations in contrast can be observed, while clear porosity features are observed in the differential phase images, it can be concluded that most these features have a scale above the system's resolution. This does not indicate a complete lack of sub-resolution features, but rather their tendency not to cluster at a given location. The horizontal lines seen across all images are artefacts caused by interruptions in the mask apertures.

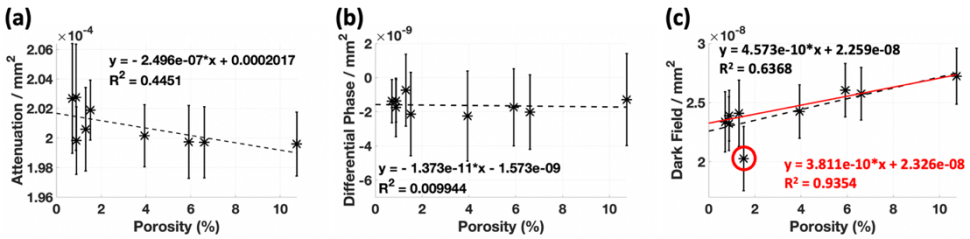

Figure 6-7 *Attenuation signal averaged per mm² (a), average differential phase signal per mm² (b), and average dark field signal per mm² (c) plotted against porosity values from matrix digestion.*

The X-ray attenuation and differential phase signals were averaged across the scanned area and compared to the average porosity values estimated from matrix digestion, as shown in Fig. 6-7. It can be observed that the X-ray attenuation signal only shows a small variation across the different plates, with no correlation for the low porosity plates, and a small decrease in signal for the higher porosity ones. The decrease observed in the attenuation signal across the plates is smaller than the standard deviations of the signal itself, which leads to

the conclusion that the attenuation signal has a very low sensitivity to variations in porosity up to 10.7%. The small changes in the attenuation signal could also be due to the variations in the plate thickness, which increased in thickness with increasing porosity, due to the different autoclave cures which could have led to different matrix concentrations, rather than due to the presence of porosity in the plates. No correlation can be observed for the differential phase signal when compared to the porosity estimated from matrix digestion. This is expected: as the differential signal highlights the presence of interfaces with bright and dark fringes, these cancel each other out when averaged over a large area.

Despite a lack of observable features in the individual dark field images, when averaging the signal across the whole plate, correlation can be observed between the average dark field signal and the porosity values estimated from matrix digestion (Fig 6-7(c)). As can be observed in the plot, a single outlier affects the correlation across all frequencies, circled in red. This point corresponds to the plate with 1.53% porosity, which was manufactured differently from the rest of the plates, as explained in Chapter 6.2. Since that point was a clear outlier, it was decided to discard it. This could indicate that the dark field signal is sensitive to changes in the porosity distribution on a microscopic level when modifying a single parameter of the manufacturing process. This could potentially be used for investigations of porosity formation and distribution in composite plates to perfect manufacturing process and minimise porosity. When discarding the 1.53% porosity plate, the R^2 increases from 0.64 to 0.94. This correlation supports the hypothesis that the dark field signal is sensitive to sub-pixel features occurring in porous plates, and the levels of sub-pixel scale inhomogeneity in those plates increases with increasing porosity.

Despite a high overall correlation between the dark field signal and the porosity values estimated from matrix digestion, for plates below 4%

porosity the correlation becomes weak, and the dark field signal for the mid-porosity plate (3.4%) is similar to the signal from the plates with porosity below 2%. This can indicate that, for plates with porosity below 4%, the average amount of sub-pixel features is similar. However, the variation in larger scale porosity between the mid-porosity plate and the low porosity plates is clearly visible in both the attenuation and the differential phase images in Fig 6-6, with the mid-porosity plate exhibiting many porosity features compared with the low porosity plate, where no features were visible. This evaluation supports the hypothesis that the dark field signal is sensitive to sub-resolution features, and that their prevalence increases with increasing porosity levels. However, the weak correlation for the low and mid-porosity plates, combined with the lack of visible features in the dark field images, suggests that a significant fraction of the porosity features is on a scale equal to or larger than the system resolution, and consequently outside the sensitivity range of the dark field signal.

6.6 Standard deviation of differential phase signal and comparison with ultrasonic attenuation

A new metric was introduced to compensate for the dark field signal only being sensitive to sub-pixel scale features, the standard deviation of the differential phase (STDP). It is a measure of how many “edges” of features are present per unit area, and as a result is a similar measure as the dark field signal, but for features on a scale equal to or above the system resolution. Images of the STDP were created for the same ROIs from the four plates shown in Fig 6-8, by calculating the standard deviation of the differential phase over an area comparable to the ultrasonic resolution at 5 MHz (300 μm), shown in Fig. 6-4. In these images, the contrast was enhanced independently for each image to highlight the observed features.

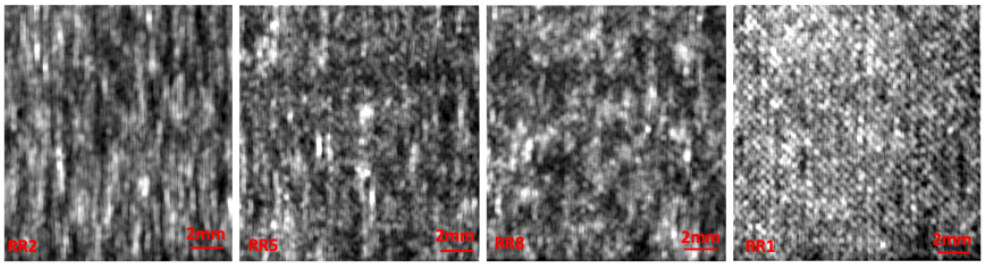

Figure 6-8 *Standard deviation of the differential phase images of ROIs from four different plates with varying degrees of porosity (left to right: 10.7%, 6.6%, 3.4%, 0.7%) taken over a 300*300μm².*

The bright areas in the images correspond to area with a high STDP, i.e., areas with a large variation in sample inhomogeneity. For the highest porosity plate (10.7%), long vertical lines are visible across the image, corresponding to the porosity following the woven yarns observed in the attenuation and differential phase images (Fig. 6-6). However, whereas the differential phase enhanced the porosity location within the image by highlighting their edges, here it is the local porosity concentration that is enhanced, with brighter areas corresponding to higher concentration of inhomogeneities. In the second highest porosity plate (6.6%), the vertical porosity features are still visible, however the most intense features are from the randomly distributed areas across the image, indicating a reduction in the porosity along the woven yarns of the plate. In the mid-porosity plate (3.4%), no vertical features are visible anymore, and the high intensity features are scattered randomly across the ROI, in accordance with the observations made from the attenuation and differential phase images. For the lowest porosity plate (0.7%), the contrast has been stretched considerably to enhance the features found in the ROI, however those do not correspond to porosity features, but to the regular structural features of the woven plate. It must be noted, however, that a gradient can be observed throughout the ROI, pointing toward the presence of some porosity features in the top-left part.

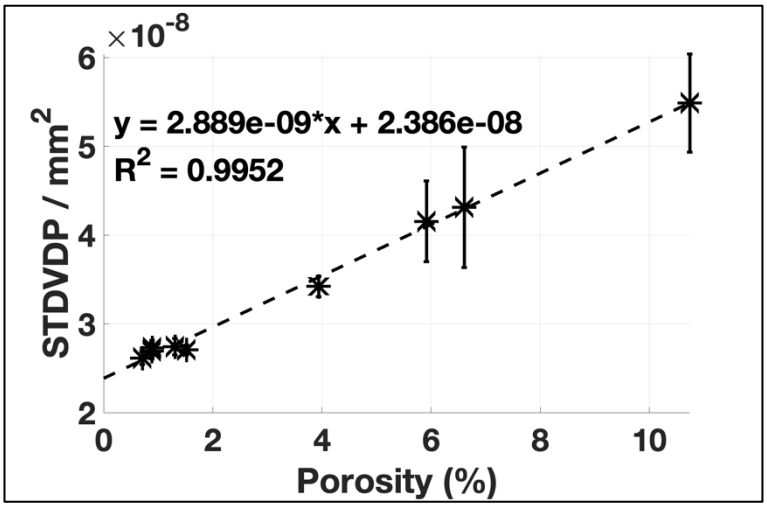

Figure 6-9 *Average standard deviation of the differential phase signal per mm^2 compared with porosity estimated from matrix digestion.*

The STDP signal was averaged across the scanned areas and compared to the average porosity values estimated from matrix digestion, as shown in Figure 6-9. An extremely good correlation can be observed between the STDP and the porosity values from matrix digestion. This demonstrates the capability of the STDP approach to quantify the degree of porosity in the specimens used, with an R^2 values of 0.99, the highest observed across all measurements – be they X-ray or ultrasonic. Moreover, unlike the ultrasonic attenuation values, a correlation can be observed between the STDP and the porosity values even for the lower porosity plates (<2%). The error bars in the figure correspond to the variation in the STDP across the individual plates and can be compared to the variation in signal observed from the ultrasonic C-scans in Fig. 6-4. As was observed in the ultrasound measurements, a wider range of attenuation values was observed for the high porosity plates, which corresponds to the correspondingly larger error bars in Fig. 6-9. Similarly, the low porosity plates were very uniform in the ultrasonic scans, which is mirrored here by very small error bars for low porosity.

These positive results lead to the further investigation of the STDP approach, by looking into the relationship between STDP and the

ultrasonic attenuation signals for the whole plates as well as on an ROI basis (section 6.9).

6.7 EI XPCi for assessment of porosity in CFRP compared to Ultrasonic Attenuation

The average attenuation, differential phase and dark field signals were also plotted against the ultrasonic attenuation signals for the 5 MHz focussed transducer values obtained at UCL, as shown in Fig. 6-10

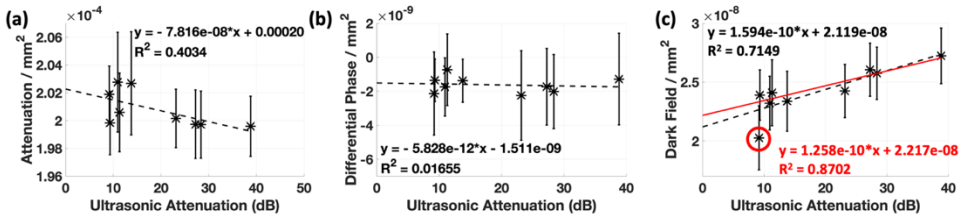

Figure 6-10 *Average attenuation (a), differential phase (b) and dark field (c) signal per mm² compared with ultrasonic signal attenuation for 5MHz focussed transducer.*

For the X-ray attenuation, a weak correlation was found with the ultrasonic signal attenuation, and no correlation was found for the differential phase. This result was expected, as similar correlations were found between those signals and the porosity from the matrix digestion, as explained above. The attenuation and differential phase signals were thus discarded from any further analysis, as they cannot be used as a measure for porosity in composite plates. As done before, for the correlation between the average dark field signal and the ultrasonic attenuation, the data point for the 1.53% porosity plate (which was manufactured differently) was discarded from the fit. The correlation between the dark field signal and the ultrasonic attenuation is comparable to the correlation with the porosity values from matrix digestion (R^2 = 0.93). Here too, a large difference can be observed in the measured ultrasonic attenuation signal between the low porosity plates and the mid-porosity plate.

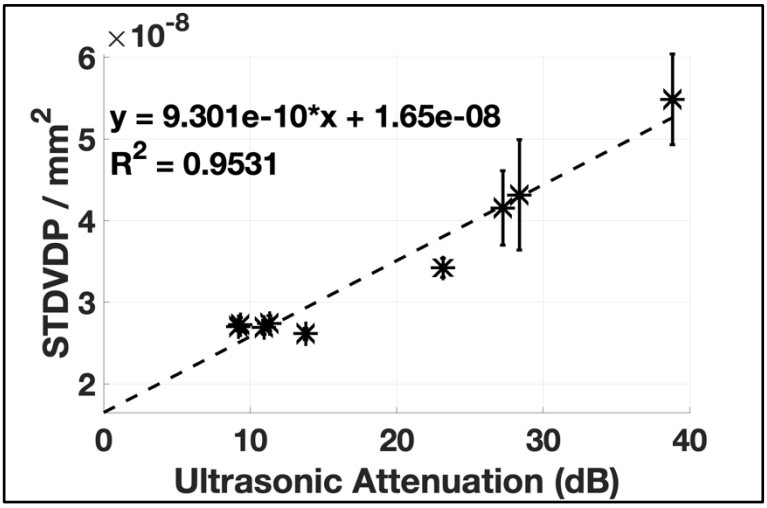

Figure 6-11 *Average standard deviation of the differential phase signals per mm^2 compared with ultrasonic signal attenuation for 5MHz focussed transducer.*

Finally, the STDP signal averaged across the scanned area was compared against the ultrasonic attenuation signals for the UCL 5 MHz focussed transducer values, as shown in Fig. 6-11. Again, a strong correlation can be observed (R^2 = 0.95), higher than correlation between ultrasound and dark field (R^2 = 0.71). However, while the correlation is strong for the high porosity plates, it no longer holds for the low porosity ones, as opposed to what happens with the porosity values from matrix digestion.

6.8 Relation between EI XPCi and Ultrasonic signal attenuation for porosity estimation in FRCP on an ROI by ROI basis

The next step involved the study of the two selected XPCi signals (dark field and STDP) when compared to the ultrasonic attenuation on an ROI basis. Both the XPCi signals and the ultrasonic attenuation signal were averaged over each ROI of all 9 specimens. The comparison between the ultrasonic attenuation and dark field signal is shown in Fig. 6-12. Despite a very good correlation between the average dark field signal across the whole plate when compared to both porosity from matrix digestion (Fig. 6-7(c)) and average ultrasonic attenuation signal (Fig. 6-10(c)), a different situation is observed when looking at smaller ROIs across the plates. The linear correlation between the

average dark field signal and ultrasonic attenuation is not observed when compared on an ROI by ROI basis (R^2 = 0.3).

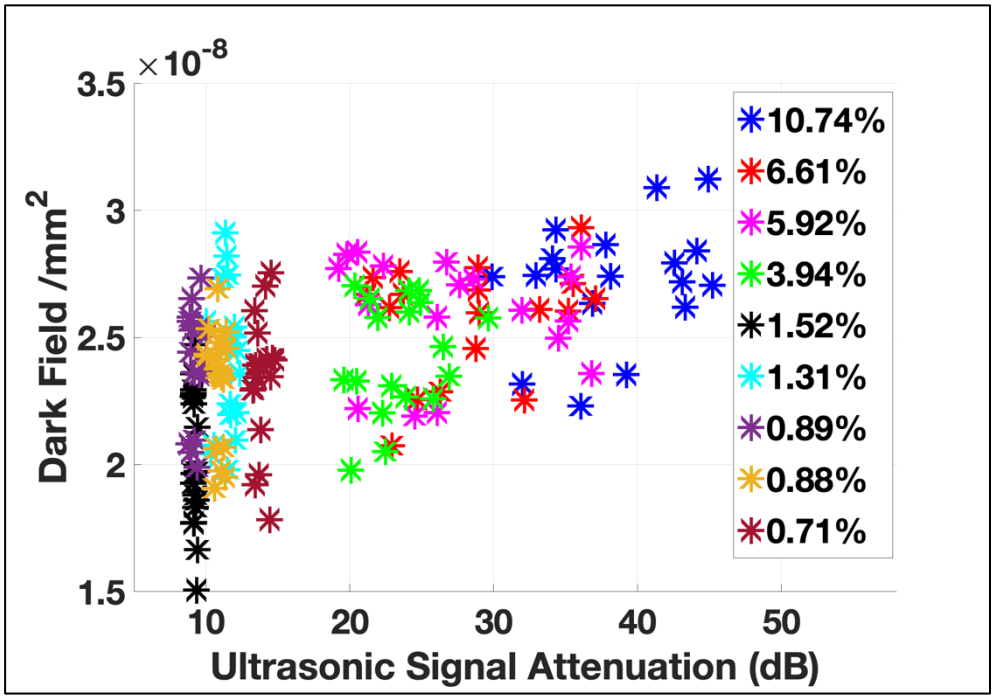

Figure 6-12 *Average dark field signal for all individual ROIs calculated for 9 specimens, plotted against the ultrasonic signal attenuation calculated over the same ROI for the 5 MHz focussed transducer.*

Moreover, the spread of the dark field signal for each individual plate across the low porosity plates is much larger than for the mid- and high porosity plates. This indicates a shift in the average size of the features from the low porosity plates to the higher porosity ones. In the high porosity plates, most of the features are equal to or above the system resolution; as a result, the large signal variation observed in the ultrasonic attenuation signals is not mirrored by the dark field signal, which is insensitive to them. In comparison, for the low porosity plates, only a very small variation is observed in the ultrasonic attenuation signal, indicating a more uniform structure and low presence of porosity features across the plates. Here, the dark field signal is extremely stretched, indicating a large variability in sub-pixel scale inhomogeneity across the plates. This could indicate the presence of microscopic (sub-pixel) porosity features in certain areas of the low

porosity plates, although not clearly visible in the images, which were not picked up by the ultrasonic attenuation signal due to their size. This is because the ultrasonic analysis in not sensitive to features of the scale observed in the dark field signal, and as a result cannot be compared.

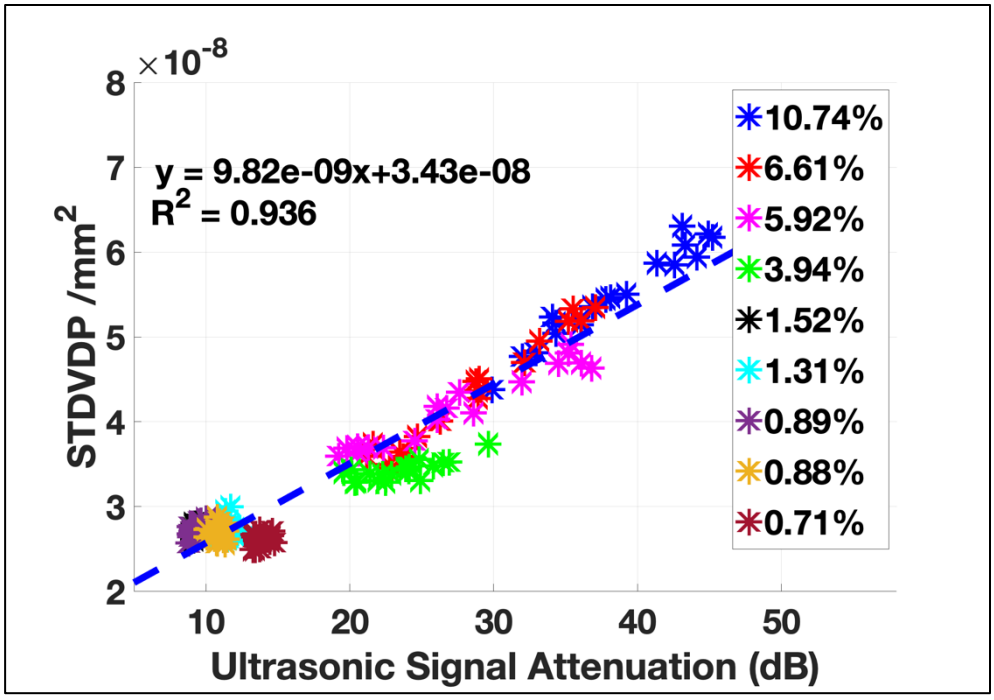

Figure 6-13 *Average STDP signal for all individual ROIs calculated for all 9 specimens, plotted against the ultrasonic signal attenuation calculated over the same ROI for the 5 MHz focussed transducer.*

This observation is further enhanced when comparing the local (i.e. ROI-based) STDP and ultrasonic attenuation signals, as shown in Fig. 6-13. Here, the linear correlation between the STDP and the ultrasonic attenuation signal is much stronger, with an R^2 of 0.94. This relation is especially apparent for the three highest porosity plates, where an increase in the average STDP over a given ROI increases with the ultrasonic signal attenuation. It can be observed that, for the mid-porosity plate (3.4%), the increase in the STDP with ultrasonic attenuation is on a different gradient compared to the high porosity plates. This is thought to be due to a shift in the porosity features towards smaller sizes, which are therefore starting to become more

prominent in the dark field signal as opposed to the STDP. Indeed, in Fig. 6-12, it can be seen that the spread of the dark field signal for that plate is larger than for the high porosity plates, but still smaller than for the low porosity plates. This could be due to the simultaneous presence of features above and below the system's resolution, with the porosity signal shared between the two contrasts as a result. For the low porosity plates, no spread can be observed in the STDP signal, with a corresponding relatively constant ultrasonic attenuation. The STDP also exhibits very small variation in the signal, indicating that for features of a scale equal to or above both the system resolution, the low porosity plate exhibits no variation in inhomogeneity and matches the ultrasonic predictions.

6.9 Conclusions

Planar Edge Illumination X-ray Phase Contrast imaging (EI XPCi) was used for the quantification of porosity in fibre reinforced woven composite plates, by comparing the three retrieved signals to porosity values obtained from matrix digestion and ultrasonic attenuation measurements. A correlation was found between the porosity content calculated using matrix digestion and the dark field signal, which is sensitive to variations in inhomogeneities in the sub-resolution scale (in this case, <12 μm). It was found that, for the set of specimens used in this investigation, despite the dark field signal offering complementary information about the microscopic features present in the plates, it did not lead to a better correlation with matrix digestion than ultrasonic attenuation. It does however allow measuring the variation in inhomogeneity across whole plate for varying degrees of porosity, showing that sub-pixel inhomogeneities increase with increasing levels of porosity. It was also observed that the dark field signal cannot be compared with ultrasonic attenuation for the quantification of porosity for the plates used in this investigation, as the scale of features observable by the dark field signal in the low porosity plates are too small to be observed by the ultrasonic attenuation and

vice versa. To compensate for difference in pore size detected by the dark field signal and ultrasonic signal attenuation, the use of the standard deviation of the differential phase (STDP) was introduced, on the assumption that it provides a similar function as the dark field signal (i.e. detecting inhomogeneities) for features equal to or above the system resolution. Overall, the STDP was shown to have a better correlation than ultrasonic attenuation when compared with porosity values from matrix digestion, including for low porosity specimens (<2%), where the ultrasonic attenuation and dark field signals showed the smallest correlation. The STDP allows for the quantification of porosity using only planar images, enabling faster scanning, at the expense of the localisation of the porosity through the plate thickness, which can be achieved through longer CT scans. It should however be noted that planar imaging allows scanning large panels without having to cut them or otherwise reduce them in size, while CT can only accommodate specimens of limited size. The variation in porosity distribution which should be further investigated with relation to the STDP (See section 8). These results indicate significant potential for this new evaluation metric in the non-destructive assessment of porosity content for fibre-reinforced composite plates.

7 Conclusions

CFRP are widely used across a range of industries thanks to their low weight and high strength. However, due to their brittle nature, they are prone to defects, both in-service and during manufacturing. Several NDE techniques exists in order to detect and identify defects in CFRP, with the most common ones being ultrasonic imaging and X-ray CT imaging. However, both techniques have disadvantages, with ultrasonic imaging offering relatively low resolution, and X-ray CT being costly, time consuming and imposing limitations on the sample size. During this PhD research, EI XPCi was benchmarked as a new, viable NDE technique for damage detection in CFRP specimens. EI XPCi and ultrasonic immersion C-scan imaging were used to assess the damage in a small pre-preg CFRP plate with severe impact damage. Both qualitative and quantitative comparisons were performed to evaluate the extent of the features observed using the two imaging methods. On a quantitative level, the ultrasonic and EI XPCi imaging techniques are comparable and allow for the detection and measurement of different features in the sample. However, the EI XPCi imaging proved to offer a more detailed identification and localisation of damage, as ultrasonic C-scan imaging has limited resolution and detection capabilities for multiple defects across the sample thickness. Moreover, the dark field images provided information regarding fibre damage which was not visible in ultrasonic C-scan imaging or in attenuation and differential phase X-ray images. CT EI XPCi allowed for the detection of multiple delaminations across the sample thickness, as well as a crack across the sample thickness. These features were not observed using ultrasonic imaging or in the planar EI XPCi images. These observations were confirmed using a high-resolution conventional X-ray CT imaging, where the features and extent of the damage observed in the dark field signal were also observed. It can thus be concluded that EI XPCi imaging, and more specifically CT imaging, can provide a more precise tool for damage detection and localisation, as well as for quantitative evaluation of

damage in composite plates, as the inclusion of the differential phase and dark field signals offer complementarity to the conventional attenuation and allow for the identification of different types of defects.

A comparison between EI XPCi and ultrasonic immersion C-scan imaging was done for damage detection in composites using planar imaging instead of CT. A severely damaged cross-ply pre-preg CFRP plate was used, with all three X-ray channels compared to both B-scan and C-scan imaging. A network of cracks was observed using the differential phase and dark field signal, with some cracks only visible in the dark field signal, indicating the presence of micro-cracks across the damaged area of the sample. As expected, the individual cracks were not observed in the ultrasonic C-scan, however the extent of the damage was mostly observed through the ultrasonic imaging, with the cracks observed in EI XPCi extending a few mm outside of the area observed through the ultrasonic imaging. These observations were then confirmed using contrast agent X-ray imaging, which is used to enhance the contrast in conventional X-ray imaging and highlight the presence of damage in the plate. However, contrast agent-enhanced X-ray imaging has an important limitation in that it requires a direct path between the surface and a given feature for the dye to penetrate, and therefore for the feature to become visible. This limitation was overcome by EI XPCi, where both the differential phase and dark field signals were able to detect cracks that were not visible using the contrast agent X-ray imaging due to a lack of a direct path to those defects. Neither planar EI XPCi and contrast agent-enhanced X-ray imaging could detect the presence of a delamination, which was detected using the ultrasonic immersion double through transmission C-scan. This was expected as features perpendicular to the X-ray beam, such as delaminations, can only be detected using CT imaging and are typically not visible in planar imaging. It was concluded that the combination of both planar EI XPCi and ultrasonic immersion imaging was necessary for a complete assessment of the damage and its extent in CFRP plates.

Planar EI XPCi was then used for the detection of manufacturing defects in CFRP. In particular, the differential phase and dark field signals were used for the quantification of porosity content in cross-ply pre-preg woven fiber-reinforced composite plates with porosity content varying from 0.7% to 10.7%. The three EI XPCi signals were compared to ultrasonic immersion through transmission imaging and matrix digestion, the standard industry methods for non-destructive and destructive porosity content evaluation, respectively. The dark field signal showed reasonably good correlation with both matrix digestion and ultrasonic signal attenuation, however the same correlation was not observed for mid- and low porosity plates. Together with the observation of the differential phase images, it was concluded that, for the set of samples used in this investigation, the scale of the porosity was equal to or above the system resolution, and as a result the use of the dark field signal was not suitable. The use of the standard deviation of the differential phase (STDP) for the evaluation of porosity or voids on a scale equal to or larger than the system resolution was therefore introduced. The STDP fulfils a similar role to the dark field signal, in that it shows variations in the distribution of inhomogeneities in a sample, but for features on a scale equal to or above the system resolution. The STDP signal showed a very good correlation with both matrix digestion and ultrasonic signal attenuation. The use of the STDP allows for the use of planar imaging for porosity quantification in CFRP, which, when using conventional X-ray imaging, is only achievable with X-ray CT.

8 Future work

The PhD research has benchmarked EI XPCi as a viable non-destructive evaluation technique for damage detection in CFRP. The use of CT EI XPCi has shown the complementarity of the phase-based signals to the conventional attenuation signal, thus allowing for a better understanding of the damage extent, as well as the identification of different defects and their scale across the sample. The same was then shown by moving to 2D planar imaging, where the capabilities of EI XPCi to detect the damage extent and identify the different types of damage were maintained and shown to surpass contrast agent X-ray imaging. However, the need for complementary ultrasonic imaging was still necessary, as a large delamination found in the ultrasonic C-scans was not detected in either planar X-ray imaging techniques. Lastly, the introduction of the novel STDP opened the door to a new, fast, and efficient way for the detection and quantification of porosity in CFRP.

The novelty from this PhD project can lead to further work in different directions:

1. Computed Laminography EI XPCi

Despite being the most common NDE technique used in industry, as it offers high resolution and a comprehensive 3D imaging of the sample, CT imaging has a lot of limitations when scanning CFRP plates, the main one being the impractical aspect ratio of the plates. Laminography is a 3D imaging technique which involves tilting the axis of rotation of the scanned sample instead of having the rotation axis perpendicular to the incident X-ray beam, as is done in X-ray CT. By rotating the sample in such a way, a high-resolution scan is still obtained, whilst the issues which arise from the scanning of laterally extended objects such as composite plates, e.g., the high variation in the X-rays path lengths with the object rotation, are mitigated. This can also be used to explore damage detection in irregularly shaped composites. Such an imaging approach can also result in shortened

scanning times. However, this imaging technique leads to an incomplete sampling of the 3D Fourier domain of the sample, and thus to lower signal-to-noise ratios and artefacts compared to CT imaging[173]. Computed laminography (CL) inspection of damaged composite plates have been done using synchrotron radiation[174,175], however, it was never implemented in a laboratory environment for XPCi. Including CL as an X-ray imaging technique would provide an additional capability to EI XPCi as an NDE imaging method in comparison with ultrasonic imaging. Applications for such imaging will include the detection and quantification of delamination in CFRP, as well as investigation of porosity, mainly for mapping the porosity distribution and size within the samples.

2. The expansion of the STDP signal

The use of the STDP, in conjunction with the dark field signal, holds great promise to quantify porosity in composite plates; however, further research should be conducted on the relation between the newly investigated STDP and dark field signals, especially in terms of understanding the interplay between signals caused by features above and below the system resolution, and ultimately of developing effective means to combine them. Pores and defects above and below the system resolution would normally be expected to be present in the structure, and the results presented so far offer a way to assess them independently, but not to combine them. Scans with varying levels of resolution, performed for example by means of masks with different aperture sizes, may offer the possibility to independently analyse pore size distributions between certain pre-determined average dimensions, similarly to differential sieving, thus allowing for a more thorough characterization in the future. Furthermore, since the STDP is a measure of material interfaces, it is dependent on porosity content, pore size and porosity distribution. It would be interesting to test the response of the STDP signal to specimens manufactured using different methods leading to variations of porosity shape and distribution, while keeping in mind that the general principle of dark

field and STDP being sensitive to features below and above the system resolution (respectively) is a feature of the imaging method and not of the investigated sample. The STDP signal should be characterized and used for multi-modal, multi-scale imaging. The use of STDP can also be expanded to other applications, e.g. additive manufacturing structures, bone remodelling around porous implants, electrode corrosion in batteries and possible even tumours in soft tissue.

3. Scaling up of the technology for “real life” specimens

The use of EI XPCi for damage detection in CFRP was described here, showing good results for both in-service and manufacturing defects. However, small samples were used in this investigation adapted to the laboratory equipment. The next step would include the scaling up of the EI XPCi system for “real life” industrial specimens, typically large plate components requiring a much larger field of view. A pre-commercial prototype of the system already exists at the Nikon facility, providing a large field of view of 200*500 mm^2 [120]. As the angular resolution of the system is dictated by the aperture size and not the detector pixel size, scaling up can be achieved without compromising on the resolution. Other parameters, such as fast scanning, and the adaptation of the system large specimen was shown to be straightforward and require minimal engineering investment[120]. Actual aircraft parts could be tested to prove the efficacy of the technique for larger samples, with the possibility of going beyond the current largest field of view, thus accommodating for in-situ inspection in future.

References

1. Gholizadeh S. A review of non-destructive testing methods of composite materials. In: XV Portugese Conference on Fracture [Internet]. Elsevier B.V.; 2016. p. 50–7. Available from: http://linkinghub.elsevier.com/retrieve/pii/S2452321616000093
2. Tian Z, Yu L, Leckey C. Delamination detection and quantification on laminated composite structures with Lamb waves and wavenumber analysis. J Intell Mater Syst Struct [Internet]. 2015;26(13):1723–38. Available from: http://journals.sagepub.com/doi/10.1177/1045389X14557506
3. Birt EA, Smith RA. A review of NDE methods for porosity measurement in fibre-reinforced polymer composites. Insight. 2004;46(11):681–6.
4. Alves CL, Oliveira JS, Tannus A, Tarpani ACSP, Tarpani JR. Detection and imaging of damages and defects in fibre-reinforced composites by resonance magnetic technique. Materials (Basel). 2021;14(4):1–22.
5. Battams GP, Dulieu-Barton JM. Data-rich characterisation of damage propagation in composite materials. Compos Part A Appl Sci Manuf. 2016;91(1):420–35.
6. Jolly M, Prabhakar A, Sturzu B, Hollstein K, Singh R, Thomas S, et al. Review of Non-destructive Testing (NDT) Techniques and their Applicability to Thick Walled Composites. In: Procedia CIRP [Internet]. Elsevier B.V.; 2015. p. 129–36. Available from: http://dx.doi.org/10.1016/j.procir.2015.07.043
7. Scott IG, Scala CM. A Review of Non-Destructive Testing of Composite Materials. NDT Int. 1982;15(2):75–86.
8. Cloetens P, Pateyron-Salomé M, Buffière JY, Peix G, Baruchel J, Peyrin F, et al. Observation of microstructure and damage in materials by phase sensitive radiography and tomography. J Appl Phys [Internet]. 1997 [cited 2018 Apr 17];81(1):5878–86.

Available from: https://doi.org/10.1063/1.364374
9. Cosmi F, Bernasconi A, Sodini N. Phase contrast micro-tomography and morphological analysis of a short carbon fibre reinforced polyamide. Compos Sci Technol [Internet]. 2011;71(1):23–30. Available from: http://dx.doi.org/10.1016/j.compscitech.2010.09.016
10. Olivo A, Castelli E. X-Ray Phase Contrast Imaging: From Synchrotrons to Conventional Sources. Riv del Nuovo Cim. 2014;37(9):467–508.
11. Endrizzi M, Diemoz PC, Millard TP, Louise Jones J, Speller RD, Robinson IK, et al. Hard X-Ray Dark-Field Imaging with Incoherent Sample Illumination. Appl Phys Lett. 2014;104(2):3–6.
12. Adams RD, Cawley P. A review of defect types and nondestructive testing techniques for composites and bonded joints. NDT&E Int [Internet]. 1988;21(4):208–22. Available from: http://linkinghub.elsevier.com/retrieve/pii/096386959190924R
13. Cantwell and Morton, J. WJ. The impact resistance of composite materials - a review. Composites [Internet]. 1991;22(5):347–62. Available from: review - 106 refs
14. Park S, Seo M. Carbon Fiber-Reinforced Polymer Composites : Preparation , Properties , and Applications. In: Polymer Composites. Weinheim, Germany: Wiley-VCH Verlag GmbH & Co. KGaA; 2012. p. 35–183.
15. Richardson M, Wisheart M. Review of Low-velocity Impact Properties of Composite Materials. Compos Part A. 1996;27(96):1123–31.
16. Toozandehjani M, Kamarudin N, Dashtizadeh Z, Yee Lim E, Gomes A, Gomez C. Conventional and Advanced Composites in Aerospace Industry: Technologies Revisited. Am J Aerosp Eng. 2018;5(1):9–15.
17. Chai GB, Manikandan P. Low velocity impact response of fibre-metal laminates - A review. Compos Struct [Internet].

2013;107:363–81. Available from: http://dx.doi.org/10.1016/j.compstruct.2013.08.003

18. Kim J, Liaw P, Hsu D, McGuire D. Nondestructive Evaluation of Nicalon/Sic Composites by Ultrasonic and X-Ray Computed Tomography. In: Ceramic Engineering and Science Proceedings. Hoboken, NJ, USA: John Wiley & Sons, Inc.; 1997. p. 287–96.
19. D. Hull, Clyne TW. An Introduction to Composite Materials. 2nd ed. Cambridge: Cambridge University Press; 2012.
20. Naik NK, Chandra Sekher Y, Meduri S. Damage in woven-fabric composites subjected to low-velocity impact. Compos Sci Technol [Internet]. 2000;60(5):731–44. Available from: http://dx.doi.org/10.1016/S0266-3538(99)00183-9
21. Aktaş M, Atas C, Içten BM, Karakuzu R. An experimental investigation of the impact response of composite laminates. Compos Struct. 2009;87(4):307–13.
22. Hull D, Bing Shi Y. Damage mechanism characterisation in composite damage tolerance investigations. Compos Struct. 1993;23:99–120.
23. Nsengiyumva W, Zhong S, Lin J, Zhang Q, Zhong J, Huang Y. Advances, limitations and prospects of nondestructive testing and evaluation of thick composites and sandwich structures: A state-of-the-art review. Compos Struct [Internet]. 2021;256(112951):1–52. Available from: https://doi.org/10.1016/j.compstruct.2020.112951
24. Hassan MH. A mini review on manufacturing defects and performance assessments of complex shape prepreg-based composites. Int J Adv Manuf Technol. 2021;115(11–12):3393–408.
25. Liu X, Chen F. A review of void formation and its effects on the mechanical performance of carbon fiber reinforced plastic. Eng Trans. 2016;64(1):33–51.
26. Loos AC, Springer GS. Curing of Epoxy Matrix Composites. J Compos Mater. 1983;17(2):135–69.

27. Mathes V. The composites industry: plenty of opportunities in heterogeneous market. Reinf Plast [Internet]. 2018;62(1):44–51. Available from: https://doi.org/10.1016/j.repl.2017.05.002
28. Tang S, Hu C. Design, Preparation and Properties of Carbon Fiber Reinforced Ultra-High Temperature Ceramic Composites for Aerospace Applications: A Review. J Mater Sci Technol [Internet]. 2017;33(2):117–30. Available from: http://dx.doi.org/10.1016/j.jmst.2016.08.004
29. Mathes V. The composites industry: plenty of opportunities in heterogeneous market. Reinf Plast. 2018;62(1):44–51.
30. S H, W C. 3D Surface Profile Construction and Flaw Detection in a Composite Structure. Strength Mater. 2019;51(1):130–7.
31. Tuwair H, Drury J, Volz J. Testing and evaluation of full scale fiber-reinforced polymer bridge deck panels incorporating a polyurethane foam core. Eng Struct. 2019;184(1):205–16.
32. Holmes M. Aerospace looks to composites for solutions. Reinf Plast [Internet]. 2017;61(4):237–41. Available from: http://dx.doi.org/10.1016/j.repl.2017.06.079
33. Toozandehjani M, Kamarudin N, Dashtizadeh Z, Yee Lim E, Gomes A, Gomez C. Conventional and Advanced Composites in Aerospace Industry: Technologies Revisited. Am J Aerosp Eng. 2018;5(1):9–15.
34. Holmes M. Aerospace looks to composites for solutions. Reinf Plast. 2017;61(4):237–41.
35. Nsengiyumva W, Zhong S, Lin J, Zhang Q, Zhong J, Huang Y. Advances, limitations and prospects of nondestructive testing and evaluation of thick composites and sandwich structures: A state-of-the-art review. Compos Struct. 2021;256(112951):1–52.
36. Ciampa F, Mahmoodi P, Pinto F, Meo M. Recent advances in active infrared thermography for non-destructive testing of aerospace components. Sensors. 2018;18(2):609.
37. Selvaraju S, Ilaiyavel S. Applications of composites in marine industry. J Eng Res Stud [Internet]. 2011;2(2):89–91. Available

from: http://www.technicaljournalsonline.com/jers/VOL II/JERS VOL II ISSUE II APRIL JUNE 2011/ARTICLE 19 JERS VOL II ISSUE II APRIL- JUNE 2011.pdf

38. Aymerich F, Meili S. Ultrasonic evaluation of matrix damage in impacted composite laminates. Compos Part B Eng. 2000;31(1):1–6.
39. Talreja R, Chandra VS. Damage and Failure of Composite Materials. Toronto, Canada: Cambridge University Press; 2012. 36–56 p.
40. Davies G, Olsson R. Impact on Composite Structures. Aeronaut J. 2005;108(1089):541–63.
41. Ibrahim ME. Nondestructive evaluation of thick-section composites and sandwich structures: A review. Compos Part A Appl Sci Manuf [Internet]. 2014;64:36–48. Available from: http://dx.doi.org/10.1016/j.compositesa.2014.04.010
42. ASTM International. E1316-17A – Standard terminology for nondestructive examinations. 2017.
43. Birt EA, Smith RA. A review of NDE methods for porosity measurement in fibre-reinforced polymer composites. Insight. 2004;46(11):681–6.
44. Donadon M V., Iannucci L, Falzon BG, Hodgkinson JM, de Almeida SFM. A progressive failure model for composite laminates subjected to low velocity impact damage. Comput Struct. 2008;86:1232–52.
45. Kite AH, Hsu DK, Barnard DJ. Determination of porosity content in composites by micrograph image processing. AIP Conf Proc. 2008;975:942–9.
46. de Almeida SFM, Neto Z dos SN. Effect of void content on the strength of composite laminates. Compos Struct. 1994;28(2):139–48.
47. Fernlund G, Wells J, Fahrang L, Kay J, Poursartip A. Causes and remedies for porosity in composite manufacturing. IOP Conf Ser Mater Sci Eng. 2016;139(1).
48. Liu X, Chen F. A review of void formation and its effects on the

mechanical performance of carbon fiber reinforced plastic. Eng Trans. 2016;64(1):33–51.
49. Liu L, Zhang BM, Wu ZJ, Wang DF. Effects of Cure Pressure Induced Voids on the Mechanical Strength of Carbon/Epoxy Laminates.pdf. J Mater Sci Technol. 2005;21(1):87–91.
50. Jeong H. Effects of Voids on the Mechanical Strength and Ultrasonic Attenuation of Laminated Composites. J Compos Mater. 1997;31(3):276–92.
51. Mehdikhani M, Gorbatikh L, Verpoest I, Lomov S V. Voids in fiber-reinforced polymer composites: A review on their formation, characteristics, and effects on mechanical performance. J Compos Mater. 2019;53(12):1579–669.
52. de Almeida SFM, Neto Z dos SN. Effect of void content on the strength of composite laminates. Compos Struct. 1994;28(2):139–48.
53. Staszewski WJ, Mahzan S, Traynor R. Health Monitoring of Aerospace Composite Structures - Active and Passive Approach. Compos Sci Technol [Internet]. 2009;69:1678–85. Available from: http://dx.doi.org/10.1016/j.compscitech.2008.09.034
54. Scarponi C, Briotti G, Barboni R, Marcone A, Iannone M. Impact Testing on Composites Laminates and Sandwich Panels. J Compos Mater. 1996;30(17):1873–911.
55. Davis TJ, Gao D, Gureyev TE, Stevenson AW, Wilkins SW. Phase contrast imaging of weakly absorbing materials using hard x-rays. Nature [Internet]. 1995 [cited 2018 Apr 17];373(16):595–8. Available from: https://www.nature.com/articles/373595a0.pdf
56. Geubelle PH, Baylor JS. Impact-induced delamination of composites: A 2D simulation. Compos Part B Eng. 1998;98(4):589–602.
57. Shyr TW, Pan YH. Impact resistance and damage characteristics of composite laminates. Compos Struct. 2003;62(2):193–203.

58. Lapczyk I, Hurtado JA. Progressive damage modeling in fiber-reinforced materials. Compos Part A Appl Sci Manuf. 2007;38(1):2333–41.
59. De Moura MFSF, Marques AT. Prediction of low velocity impact damage in carbon epoxy laminates. Compos Part A [Internet]. 2002;33(1):361–268. Available from: www.elsevier.com/locate/compositesa
60. Williams G, Trask R, Bond I. A Self-Healing Carbon Fibre Reinforced Polymer for Aerospace Applications. Compos Part A. 2007;38(6):1525–32.
61. Wang B, Zhong S, Lee TL, Fancey KS, Mi J. Non-destructive testing and evaluation of composite materials/structures: A state-of-the-art review. Adv Mech Eng. 2020;12(4):1–28.
62. Achenbach J. Quantitative nondestructive evaluation. Int J Solids Struct [Internet]. 2000;37(1–2):13–27. Available from: http://linkinghub.elsevier.com/retrieve/pii/S0020768399000748
63. Javadi Y, Najafabadi MA. Comparison between contact and immersion ultrasonic method to evaluate welding residual stresses of dissimilar joints. Mater Des [Internet]. 2013;47:473–82. Available from: http://dx.doi.org/10.1016/j.matdes.2012.12.069
64. He Y, Tian G, Pan M, Chen D. Non-destructive testing of low-energy impact in CFRP laminates and interior defects in honeycomb sandwich using scanning pulsed eddy current. Compos Part B Eng [Internet]. 2014;59(1):196–203. Available from: http://dx.doi.org/10.1016/j.compositesb.2013.12.005
65. Sun H, Kosukegawa H, Hashimoto M, Uchimoto T, Takagi T. Electromagnetic-pulse-induced acoustic testing for nondestructive testing of plastic composite/metal adhesive bonding. Int J Hydrogen Energy [Internet]. 2020;45(55):31303–14. Available from: https://doi.org/10.1016/j.ijhydene.2020.08.079
66. Alves CL, Oliveira JS, Tannus A, Tarpani ACSP, Tarpani JR. Detection and imaging of damages and defects in fibre-

reinforced composites by resonance magnetic technique. Materials (Basel). 2021;14(4):1–22.

67. Garcea SC, Wang Y, Withers PJ. X-ray computed tomography of polymer composites. Compos Sci Technol [Internet]. 2018;156(1):305–19. Available from: https://doi.org/10.1016/j.compscitech.2017.10.023
68. Jeong H, Hsu DK. Experimental analysis ultrasonic attenuation in carbon composites of porosity-induced and velocity change. Ultrasonics. 1995;33(3):195–203.
69. Smith RA, Nelson LJ, Mienczakowski MJ, Challis RE. Automated analysis and advanced defect characterisation from ultrasonic scans of composites. Insight Non-Destructive Test Cond Monit. 2009;51(2):82–7.
70. Agyei RF, Sangid MD. A Supervised Iterative Approach to 3D Microstructure Reconstruction from Acquired Tomographic Data of Heterogeneous Fibrous Systems. Compos Struct [Internet]. 2018;206:234–46. Available from: https://doi.org/10.1016/j.compstruct.2018.08.029
71. Mccombe GP, Rouse J, Trask RS, Withers PJ, Bond IP. X-ray Damage Characterisation in Self-Healing Fibre Reinforced Polymers. Compos Part A [Internet]. 2012 [cited 2018 Apr 17];43:613–20. Available from: https://ac.els-cdn.com/S1359835X11004258/1-s2.0-S1359835X11004258-main.pdf?_tid=fda357b4-84c1-4f05-b6a2-34f63b6978f0&acdnat=1523976492_625467194051e49dfdf4f70797a17865
72. Yang R, He Y. Optically and non-optically excited thermography for composites: A review. Infrared Phys Technol. 2016;75(1):26–50.
73. Araújo dos Santos J V., Lopes HMR, Vaz M, Mota Soares CM, Mota Soares CA, de Freitas MJM. Damage localization in laminated composite plates using mode shapes measured by pulsed TV holography. Compos Struct. 2006;76(3):272–81.
74. Cawley P. The rapid non-destructive inspection of large

composite structures. Composites. 1994;25(5):351–7.
75. Bhat MR. Non-Destructive Evaluation of Defects and Damage in Composite Materials and Structures. J Indian Inst Sci. 2013;93(4):751–65.
76. Katunin A, Dragan K, Dziendzikowski M. Damage identification in aircraft composite structures: A case study using various non-destructive testing techniques. Compos Struct [Internet]. 2015;127:1–9. Available from: http://dx.doi.org/10.1016/j.compstruct.2015.02.080
77. Cartz L. Nondestructive Testing. Milwaukee: ASM International; 1995.
78. Hassan MH, Othman AR, Kamaruddin S. Void content determination of fiber reinforced polymers by acid digestion method. Adv Mater Res. 2013;795(2):64–8.
79. Kite AH, Hsu DK, Barnard DJ. Determination of porosity content in composites by micrograph image processing. AIP Conf Proc. 2008;975:942–9.
80. Farhang L, Fernlund G. Void and porosity characterization of uncured and partially cured prepregs. J Compos Mater. 2016;50(7):937–48.
81. Ramzi R, Mahmod MF, Bakar EA. Immersion ultrasonic inspection system for small scaled composite specimen. ARPN J Eng Appl Sci. 2015;10(22):17146–50.
82. Hartmann B, Jarzynski J. Immersion apparatus for ultrasonic measurements in polymers. J Acoust Soc Am [Internet]. 1974;56(5):1469–77. Available from: http://link.aip.org/link/?JAS/56/1469/1
83. Fahr A, Kandeil AY. Ultrasonic C-scan inspection of composite materials. Eng J Qatar Univ. 1992;5(1):201–22.
84. Scarponi C, Briotti G. Ultrasonic technique for the evaluation of delaminations on CFRP, GFRP, KFRP composite materials. Compos Part B Eng. 2000;31(3):237–43.
85. He M, Yang T. Non-Destructive Evaluation of the Bending-Fatigue Damage in Carbon-Fiber-Composite Laminates Based

on Ultrasonic Wave Propagation. J Test Eval [Internet]. 2018;46(2):647–55. Available from: http://www.astm.org/doiLink.cgi?JTE20160190

86. Stone DEW, Clarke B. Ultrasonic attenuation as a measure of void content in carbon-fibre reinforced plastics. Non-Destructive Test. 1975;8(3):137–45.
87. Reed FA, Batzinger TJ, Reed RW, Jönsson S. Porosity Measurement in Composites Using Ultrasonic Attenuation Methods. Rev Prog Quant Nondestruct Eval. 1993;12(1):1265–72.
88. M.S. Hughes, S.M. Handley, J.G. Miller, E.I. Madaras. A relationship between frequency dependent ultrasonic attenuation and porosity in composite laminates. In: Review of Progress in Quantitative Nondestructive Evaluation. Boston: Springer US; 1988. p. 1037–44.
89. Daniel IM, Wooh SC, Komsky I. Quantitative porosity characterization of composite materials by means of ultrasonic attenuation measurements. J Nondestruct Eval. 1992;11(1):1–8.
90. Okahara T, Biwa S, Kuraishi A. Nondestructive evaluation of porosity content in the curved corner section of composite laminates using focused ultrasonic waves. J Nondestruct Eval Diagnostics Progn Eng Syst. 2018;1(1):1–6.
91. Smith RA, Nelson LJ, Mienczakowski MJ, Wilcox PD. Ultrasonic Analytic-Signal Responses from Polymer-Matrix Composite Laminates. IEEE Trans Ultrason Ferroelectr Freq Control. 2018;65(2):231–43.
92. Endrizzi M. X-Ray Phase-Ccontrast Imaging. Nucl Inst Methods Phys Res A [Internet]. 2017;830:407. Available from: http://mendeley.csuc.cat/fitxers/6cbb571494ddcd736876500d863a64c8
93. Tan KT, Watanabe N, Iwahori Y. X-ray radiography and micro-computed tomography examination of damage characteristics in stitched composites subjected to impact loading. Compos

Part B [Internet]. 2011 [cited 2018 Apr 17];42:874–84. Available from: https://ac.els-cdn.com/S1359836811000394/1-s2.0-S1359836811000394-main.pdf?_tid=ee485fe4-1459-40a9-845f-750790660141&acdnat=1523976419_7c19a13dcdfa6433212ddc6e04f03647

94. Garcea SC, Wang Y, Withers PJ. X-ray computed tomography of polymer composites. Compos Sci Technol. 2018;156(1):305–19.
95. Stamopoulos AG, Tserpes KI, Prucha P, Vavrik D. Evaluation of porosity effects on the mechanical properties of carbon fiber-reinforced plastic unidirectional laminates by X-ray computed tomography and mechanical testing. J Compos Mater. 2016;50(15):2087–98.
96. Yang P, Elhajjar R. Porosity Content Evaluation in Carbon-Fiber/Epoxy Composites Using X-ray Computed Tomography. Polym - Plast Technol Eng. 2014;53(3):217–22.
97. Wildenschild D, Sheppard AP. X-ray imaging and analysis techniques for quantifying pore-scale structure and processes in subsurface porous medium systems. Adv Water Resour [Internet]. 2013;51:217–46. Available from: http://dx.doi.org/10.1016/j.advwatres.2012.07.018
98. Yu B, Bradley RS, Soutis C, Withers PJ. A comparison of different approaches for imaging cracks in composites by X-ray microtomography. Philos Trans R Soc A Math Phys Eng Sci. 2016;374(2071):1–15.
99. Djukic LP, Herszberg I, Schoeppner GA, Brownlow LA. Tow Visualisation in Woven Composites using X-Ray Computed Tomography. In: Proceedings of the 9th International Conference on Textile Composites: Recent Advances in Textile Composites. 2008. p. 417–25.
100. Lavoie JA, Adolfsson E. Stitch cracks in constraint plies adjacent to a cracked ply. J Compos Mater. 2001;35(23):2077–97.

101. Schilling PJ, Karedla BPR, Tatiparthi AK, Verges MA, Herrington PD. X-ray computed microtomography of internal damage in fiber reinforced polymer matrix composites. Compos Sci Technol. 2005;65(14):2071–8.
102. Pavier MJ, Clarke MP. Experimental Techniques for the Investigation of the Effects of Impact Damage on Carbon Fibre Composites. Compos Sci Technol [Internet]. 1995 [cited 2018 Apr 17];55(1):157–69. Available from: https://ac.els-cdn.com/0266353895000976/1-s2.0-0266353895000976-main.pdf?_tid=9ddecfea-b4f3-4f38-a7c2-7ae146b30297&acdnat=1523976439_d8f4ee751e909c6649a50e019c4b6891
103. Schilling PJ, Karedla BPR, Tatiparthi AK, Verges MA, Herrington PD. X-ray computed microtomography of internal damage in fiber reinforced polymer matrix composites. Compos Sci Technol. 2005;65(14):2071–8.
104. Massimi L, Buchanan I, Astolfo A, Endrizzi M, Olivo A. Fast, non-iterative algorithm for quantitative integration of X-ray differential phase-contrast images. Opt Express. 2020;28(26):39677.
105. Fitzgerald R. Phase-Sensitive X-Ray Imaging. Phys Today [Internet]. 2000 [cited 2018 Apr 17];53:23–6. Available from: https://doi.org/10.1063/1.1292471
106. Bravin A. Exploiting the X-Ray Refraction Contrast with an Analyser: The State of the Art. J Phys D Appl Phys. 2003;36(1):24–9.
107. Revol V, Jerjen I, Kottler C, Schütz P, Kaufmann R, Lüthi T, et al. Sub-Pixel Porosity Revealed by X-Ray Scatter Dark Field Imaging. J Appl Phys [Internet]. 2011 [cited 2018 Apr 17];110(044912):1–5. Available from: https://doi.org/10.1063/1.3624592
108. Revol V, Plank B, Kaufmann R, Kastner J, Kottler C, Neels A. Laminate Fibre Structure Characterisation of Carbon Fibre-Reinforced Polymers by X-Ray Scatter Dark Field Imaging with

a Grating Interferometer. NDT&E Int [Internet]. 2013 [cited 2018 Apr 17];58:64–71. Available from: https://ac.els-cdn.com/S0963869513000686/1-s2.0-S0963869513000686-main.pdf?_tid=0f626f82-5253-4c0f-8365-d5b3c71d9cf9&acdnat=1523975224_42ab4feafe46cf6b7e6392380008fc5a

109. Revol V, Kottler C, Kaufmann R, Straumann U, Urban C. Noise analysis of grating-based x-ray differential phase contrast imaging. Cit Rev Sci Instruments [Internet]. 2010 [cited 2018 Apr 17];81(1):1–8. Available from: https://doi.org/10.1063/1.3465334
110. Olivo A, Speller R. Modelling of a novel x-ray phase contrast imaging technique based on coded apertures. Phys Med Biol. 2007;52(22):6555–73.
111. Olivo A, Ignatyev K, Munro PRT, Speller RD. A coded-aperture based method allowing non-interferometric phase contrast imaging with incoherent X-ray sources. Nucl Instruments Methods Phys Res Sect A Accel Spectrometers, Detect Assoc Equip [Internet]. 2011;648:S28–31. Available from: http://dx.doi.org/10.1016/j.nima.2011.01.018
112. Olivo A, Ignatyev K, Munro PRT, Speller RD. Design and realization of a coded-aperture based X-ray phase contrast imaging for homeland security applications. Nucl Instruments Methods Phys Res Sect A Accel Spectrometers, Detect Assoc Equip [Internet]. 2009;610(2):604–14. Available from: http://dx.doi.org/10.1016/j.nima.2009.08.085
113. Munro PRT, Hagen CK, Szafraniec MB, Olivo A. A simplified approach to quantitative coded aperture X-ray phase imaging. Opt Express. 2013;21(9):11187.
114. Endrizzi M, Diemoz PC, Hagen CK, Millard TP, Vittoria FA, Wagner UH, et al. Laboratory-based edge-illumination phase-contrast imaging: Dark-field retrieval and high-resolution implementations. 2014 IEEE Nucl Sci Symp Med Imaging Conf NSS/MIC 2014. 2016;1–4.

115. Astolfo A, Endrizzi M, Kallon G, Millard TP, Vittoria FA, Olivo A. A first investigation of accuracy, precision and sensitivity of phase-based x-ray dark-field imaging. J Phys D Appl Phys. 2016;49(48):1–8.
116. Diemoz PC, Hagen CK, Endrizzi M, Olivo A. Sensitivity of laboratory based implementations of edge illumination X-ray phase-contrast imaging. Appl Phys Lett. 2013;103(24).
117. Diemoz PC, Endrizzi M, Zapata CE, Pešić ZD, Rau C, Bravin A, et al. X-ray Phase Contrast Imaging with Nanoradian Angular Resolution. Phys Rev Lett. 2013;110(13):1–5.
118. Munro PRT, Olivo A. X-ray phase-contrast imaging with polychromatic sources and the concept of effective energy. Phys Rev A - At Mol Opt Phys. 2013;87(5):1–7.
119. Diemoz PC, Endrizzi M, Bravin A, Robinson IK, Olivo A. Sensitivity of edge illumination X-ray phase-contrast imaging. Philos Trans R Soc A. 2014;372(20130128):1–7.
120. Astolfo A, Endrizzi M, Vittoria FA, Diemoz PC, Price B, Haig I, et al. Large field of view, fast and low dose multimodal phase-contrast imaging at high x-ray energy. Sci Rep. 2017;7(1):1–8.
121. Vavrik D, Jakubek J, Jandejsek I, Krejci F, Kumpova I, Zemlicka J. Visualization of delamination in composite materials utilizing advanced X-ray imaging techniques. J Instrum. 2015;10(4):1–10.
122. Mayo SC, Stevenson AW, Wilkins SW. In-Line Phase-Contrast X-ray Imaging and Tomography for Materials Science. Materials (Basel) [Internet]. 2012;5(12):937–65. Available from: http://www.mdpi.com/1996-1944/5/5/937/
123. Coindreau O, Vignoles G, Goyheneche J-M. Multiscale X-Ray CMT of C/C Composite Preforms: A Tool for Properties Assessment. In: Ceramic Transactions, Advances in Ceramic Matrix Composites. Hoboken, NJ, USA: John Wiley & Sons, Inc.; 2006. p. 77–84.
124. Gusenbauer C, Reiter M, Plank B, Salaberger D, Senck S, Kastner J. Porosity Determination of Carbon and Glass Fibre

Reinforced Polymers Using Phase-Contrast Imaging. J Nondestruct Eval. 2019;38(1):1–10.

125. Sarapata A, Ruiz-Yaniz M, Zanette I, Rack A, Pfeiffer F, Herzen J. Multi-contrast 3D X-ray imaging of porous and composite materials. Appl Phys Lett [Internet]. 2015;106(15):1–6. Available from: http://dx.doi.org/10.1063/1.4918617
126. Kageyama M, Okajima K, Maesawa M, Nonoguchi M, Koike T, Noguchi M, et al. X-ray phase-imaging scanner with tiled bent gratings for large-field-of-view nondestructive testing. NDT E Int [Internet]. 2019;105(January):19–24. Available from: https://doi.org/10.1016/j.ndteint.2019.04.007
127. Röper F, Plank B, Glinz J, Wolfahrt M, Kucher G, Pinter G. X-ray computed tomography in bonded aircraft repairs for composites. In: Proceedings of the 10th Conference on Industrial Computed Tomography. 2020. p. 1–6.
128. Baaklini GY, Yancey RN, Swickard SM. Ceramic Matrix Composites Characterization with X-Ray Microtomography and Ultrasonics. In: Proceedings of the 17th Annual Conference on Composites and Advanced Ceramic Materials, Part 1 of 2: Ceramic Engineering and Science Proceedings, Volume 14, Issue 7/8. Hoboken, NJ, USA: John Wiley & Sons, Inc.; 2008. p. 473–84.
129. Kim J, Liaw PK. Tensile fracture behavior of Nicalon/SiC composites. Metall Mater Trans A Phys Metall Mater Sci. 2007;38 A(13):2203–13.
130. Léonard F, Stein J, Soutis C, Withers PJ. The Quantification of Impact Damage Distribution in Composite Laminates by Analysis of X-Ray Computed Tomograms. Compos Sci Technol. 2017;152:139–48.
131. Nelson LJ, Smith RA, Mienczakowski M. Ply-orientation measurements in composites using structure-tensor analysis of volumetric ultrasonic data. Compos Part A Appl Sci Manuf [Internet]. 2018;104:108–19. Available from: https://doi.org/10.1016/j.compositesa.2017.10.027

132. Pomarède P, Meraghni F, Peltier L, Delalande S, Declercq NF. Damage Evaluation in Woven Glass Reinforced Polyamide 6.6/6 Composites Using Ultrasound Phase-Shift Analysis and X-ray Tomography. J Nondestruct Eval [Internet]. 2018;37(1):1–21. Available from: https://doi.org/10.1007/s10921-018-0467-3
133. Hannesschläger C, Revol V, Plank B, Salaberger D, Kastner J. Fibre Structure Characterisation of Injection Moulded Short Fibre-Reinforced Polymers by X-Ray Scatter Dark Field Tomography. Case Stud Nondestruct Test Eval [Internet]. 2015;3:34–41. Available from: http://dx.doi.org/10.1016/j.csndt.2015.04.001
134. Gresil M, Revol V, Kitsianos K, Kanderakis G, Koulalis I, Sauer M-O, et al. EVITA Project: Comparison Between Traditional Non-Destructive Techniques and Phase Contrast X-Ray Imaging Applied to Aerospace Carbon Fibre Reinforced Polymer. Appl Compos Mater [Internet]. 2017 [cited 2018 Apr 17];24:513–24. Available from: https://link.springer.com/content/pdf/10.1007%2Fs10443-016-9540-1.pdf
135. Senck S, Scheerer M, Revol V, Plank B, Hannesschläger C, Gusenbauer C, et al. Microcrack characterization in loaded CFRP laminates using quantitative two- and three-dimensional X-ray dark-field imaging. Compos Part A Appl Sci Manuf [Internet]. 2018 Dec;115(October 2017):206–14. Available from: https://linkinghub.elsevier.com/retrieve/pii/S1359835X18303804
136. Endrizzi M, Murat BIS, Fromme P, Olivo A. Edge-illumination X-Ray Dark-Field Imaging for Visualising Defects in Composite Structures. Compos Struct [Internet]. 2015;134(1):895–9. Available from: http://dx.doi.org/10.1016/j.compstruct.2015.08.072
137. Fromme P, Endrizzi M, Olivo A. Defect Imaging in Composite

Structures. In: AIP Conference Proceedings. 2018. p. 1–4.
138. Swait TJ, Jones FR, Hayes SA. A practical structural health monitoring system for carbon fibre reinforced composite based on electrical resistance. Compos Sci Technol [Internet]. 2012;72(13):1515–23. Available from: http://dx.doi.org/10.1016/j.compscitech.2012.05.022
139. Boaden J. A Guide to Double Through Transmission Inspection. e-Journal Nondestruct Test. 2010;44(1):1–5.
140. Rokhlin SI, Wang W. Double through-transmission bulk wave method for ultrasonic phase velocity measurement and determination of elastic constants of composite materials. J Acoust Soc Am [Internet]. 1992;91(6):3303–12. Available from: http://asa.scitation.org/doi/10.1121/1.402847
141. Guo N, Cawley P. The non-destructive assessment of porosity in composite repairs. Composites. 1994;25(9):842–50.
142. Class Instrumentation Ltd Ultrasonic Sound Velocity Table [Internet]. Available from: http://www.classltd.com/sound_velocity_table.html
143. Hellier CJ. Handbook of Nondestructive Evaluation. New York: New York: The McGraw-Hill Companies, Inc.; 2013.
144. NDT Research Center: Introduction to Ultrasonic Testing [Internet]. Available from: https://www.nde-ed.org/EducationResources/CommunityCollege/Ultrasonics/cc_ut_index.htm
145. Ultrasonic Testing (UT) - Velocity Table [Internet]. Available from: http://www.trinityndt.com/brochures/Ultrasonic_Inspection_Velocity_Table.pdf
146. Boccaccio M, Malfense Fierro GP, Meo M, Bolton G. Development and focusing enhancement of nonlinear air-coupled acoustic technique for damage characterization in materials. Mater Today Proc. 2019;34(April):266–74.
147. Mix PE. Introduction to Nondestructive Testing. Second. Hoboken, New Jersey: John Wiley & Sons, Inc.; 2005.

148. Class Instrumentation Ltd Ultrasonic Sound Velocity Table.
149. Ignatyev K, Munro PRT, Speller RD, Olivo A. Effects of signal diffusion on x-ray phase contrast images. Rev Sci Instrum. 2011;82(073702):1–9.
150. Olivo A, Speller RD. Deconvolution of x-ray phase contrast images as a way to retrieve phase information lost due to insufficient resolution. Phys Med Biol. 2009;54(15):347–54.
151. Matsunaga N, Yano K, Endrizzi M, Olivo A. Detection of individual sub-pixel features in edge-illumination X-ray phase contrast imaging by means of the dark-field channel. J Phys D Appl Phys. 2020;53(9).
152. Maughan Jones CJ, Vittoria FA, Olivo A, Endrizzi M, Munro PRT. Retrieval of weak x-ray scattering using edge illumination. Opt Lett. 2018;43(16):3874.
153. Endrizzi M, Basta D, Olivo A. Laboratory-based X-ray phase-contrast imaging with misaligned optical elements. Appl Phys Lett [Internet]. 2015;107(12):1–6. Available from: http://dx.doi.org/10.1063/1.4931778
154. Endrizzi M, Basta D, Olivo A. Laboratory-based X-ray phase-contrast imaging with misaligned optical elements. Appl Phys Lett. 2015;107(12):1–6.
155. Doherty A, Massimi L, Olivo A, Endrizzi M. Optimal and automated mask alignment for use in edge illumination X-ray differential-phase and dark-field imaging techniques. Nucl Instruments Methods Phys Res Sect A Accel Spectrometers, Detect Assoc Equip. 2020;984:1–6.
156. Shoukroun D, Massimi L, Iacoviello F, Endrizzi M, Bate D, Olivo A, et al. Enhanced composite plate impact damage detection and characterisation using X-Ray refraction and scattering contrast combined with ultrasonic imaging. Compos Part B [Internet]. 2020;181(107579):1–10. Available from: https://doi.org/10.1016/j.compositesb.2019.107579
157. Diemoz PC, Vittoria FA, Olivo A. Spatial resolution of edge illumination X-ray phase-contrast imaging. Opt Express.

2014;22(13):15514.
158. Massimi L, Hagen CK, Endrizzi M, Munro PRT, Havariyoun G, Hawker SPM, et al. Laboratory-Based X-Ray Phase Contrast CT Technology for Clinical Intra-Operative Specimen Imaging. In: Medical Imaging 2019: Physics of Medical Imaging. 2019. p. 62.
159. Limaye A. Drishti: a volume exploration and presentation tool. In: Developments in X-Ray Tomography VIII. 2012. p. 85060X.
160. Kok MDR, Robinson JB, Weaving JS, Jnawali A, Pham M, Iacoviello F, et al. Virtual unrolling of spirally-wound lithium-ion cells for correlative degradation studies and predictive fault detection. Sustain Energy Fuels. 2019;3(11):2972–6.
161. Murat BIS, Fromme P., Endrizzi M, Olivo A. Characterization of impact in composite plates. J Mech Eng. 2018;64(11):672–9.
162. Porter T, Duff T. Compositing Digital Images. Comput Graph (ACM). 1984;18(3):253–9.
163. Cantwell WJ, Morton J. Detection of impact damage in CFRP laminates. Compos Struct. 1985;3(3–4):241–57.
164. Diemoz PC, Endrizzi M, Hagen CK, Millard TP, Vittoria FA, Olivo A. Angular sensitivity and spatial resolution in edge illumination X-ray phase-contrast imaging. Nucl Instruments Methods Phys Res Sect A Accel Spectrometers, Detect Assoc Equip [Internet]. 2015;784:538–41. Available from: http://dx.doi.org/10.1016/j.nima.2014.12.027
165. Shoukroun D, Massimi L, Iacoviello F, Endrizzi M, Bate D, Olivo A, et al. Enhanced composite plate impact damage detection and characterisation using X-Ray refraction and scattering contrast combined with ultrasonic imaging. Compos Part B. 2020;181(107579):1–10.
166. Shoukroun D, Massimi L, Endrizzi M, Bate D, Fromme P, Olivo A. Composite Porosity Characterization using X-ray Edge Illumination Phase Contrast and Ultrasonic Techniques. In: Proceedings Volume 11593, Health Monitoring of Structural and Biological Systems XV. 2021. p. 115932.

167. HexPly ® M21 180C Curing Epoxy Matrix Report. 2020.
168. Nesbitt A, Godwin EW. Test Report UoM/NCCEF/QPD/RP/137250. Manchester; 2016.
169. Hassan MH, Othman AR, Kamaruddin S. Void content determination of fiber reinforced polymers by acid digestion method. Adv Mater Res. 2013;795(2):64–8.
170. ASTM D3171-15. In: Standard Test Methods for Constituent Content of Composite Materials. West Conshohocken, PA: ASTM International; 2015.
171. Reed FA, Batzinger TJ, Reed RW, Jönsson S. Porosity Measurement in Composites Using Ultrasonic Attenuation Methods. Rev Prog Quant Nondestruct Eval. 1993;12(1):1265–72.
172. Daniel IM, Wooh SC, Komsky I. Quantitative porosity characterization of composite materials by means of ultrasonic attenuation measurements. J Nondestruct Eval. 1992;11(1):1–8.
173. Bull DJ, Helfen L, Sinclair I, Spearing SM, Baumbach T. A comparison of multi-scale 3D X-ray tomographic inspection techniques for assessing carbon fibre composite impact damage. Compos Sci Technol. 2013;75:55–61.
174. Bull DJ, Spearing SM, Sinclair I, Helfen L. Three-dimensional assessment of low velocity impact damage in particle toughened composite laminates using micro-focus X-ray computed tomography and synchrotron radiation laminography. Compos Part A Appl Sci Manuf [Internet]. 2013;52:62–9. Available from: http://dx.doi.org/10.1016/j.compositesa.2013.05.003
175. Borstnar G, Mavrogordato MN, Helfen L, Sinclair I, Spearing SM. Interlaminar fracture micro-mechanisms in toughened carbon fibre reinforced plastics investigated via synchrotron radiation computed tomography and laminography. Compos Part A Appl Sci Manuf [Internet]. 2015;71:176–83. Available from: http://dx.doi.org/10.1016/j.compositesa.2015.01.012